4-8-2013

Electronic structure calculations and properties of alkaline-earth molecular ions

Sandipan Banerjee
University of Connecticut - Storrs, banerjee@phys.uconn.edu

Recommended Citation

Banerjee, Sandipan, "Electronic structure calculations and properties of alkaline-earth molecular ions" (2013). *Doctoral Dissertations*. 26.
http://digitalcommons.uconn.edu/dissertations/26

Electronic structure calculations and properties of alkaline–earth molecular ions

Sandipan Banerjee, Ph.D.

University of Connecticut, 2013

Recent years have seen many advances in the study of ultracold molecular ions [1, 2, 3]. Studies involving atom-ion scattering [4, 5], resonant charge transfer [6] and charge mobility [7] at ultracold temperatures, are a few of the many emerging fields of interest where an in-depth understanding of the underlying physics governing the interaction between atoms and ions is crucial. Alkaline-earth dimers are now being used as new grounds for testing fundamental physics laws, precision measurements [8] and quantum computation [9]. As a starting point for conducting such studies, one needs a very good knowledge of the electronic structure, energetics and long-range behavior of these molecular ions. In this thesis, we provide accurate *ab initio* calculations for the ground and low-lying excited states of Be_2^+, Mg_2^+, Ca_2^+ and Sr_2^+ molecular ions. We have also calculated the spectroscopic constants, electronic transition dipole moments, polarizabilities and long-range dispersion coefficients for the various alkaline-earth ionic dimers. We have extended our calculations to study heteronuclear species of alkaline-earth molecular ions, like BeCa^+, and mixed alkali alkaline-earth species like NaCa^+. We calculated photoassociation (PA) pathways for the formation of cold molecular ions, and also studied corrections to the Born-Oppenheimer Hamiltonian — non-adiabatic couplings and hyperfine structure due to nuclear spins and electric quadrupoles. We believe this work will lay foundation for new experiments in ultracold physics and chemistry.

Electronic structure calculations and properties of alkaline–earth molecular ions

Sandipan Banerjee

B.Sc., University of Calcutta, Kolkata, India 2004
M.Sc., University of Calcutta, Kolkata, India 2006
M.S., University of Connecticut, Storrs, CT 2008

A Dissertation
Submitted in Partial Fulfillment
of the Requirements for the Degree of
Doctor of Philosophy
at the
University of Connecticut

2013

APPROVAL PAGE

Doctor of Philosophy Dissertation

Electronic structure calculations and properties of alkaline–earth molecular ions

Presented by

Sandipan Banerjee

Major advisor ________________________________

Robin Côté

Associate advisor ________________________________

John A. Montgomery Jr.

Associate advisor ________________________________

José A. Gascón

University of Connecticut

2013

To my wife Jayita, and my parents Rathin and Dipti Banerjee;
without their love and support none of this would have been possible.
Thank you for always believing in me.

Acknowledgements

I would like to thank my major advisor Robin Côté, for all his help, and guidance during my stay here at UConn. I have learned many things from him. I was extremely blessed to have as my co-advisors John Montgomery, José Gascón and Harvey Michels. They were instrumental in guiding me when I felt I was completely lost. Several other members of the physics faculty played a significant role in my graduate education – Edward Eyler, William Stwalley, Alexander Kovner, and Juha Javanainen – I thank each one of you.

My life at UCONN would not have been easy without the help of the wonderful staff members in the Physics department. I would like to thank Carol Artacho-Guerra, Kim Giard, David Perry, Michael Rapposch, Michael Rozman, Dawn Rawlinson, Cecile Stanzione, and Barbara Styrczula for always being so helpful. I would like to thank the former and present members of the Côté research group. I also thank the members of the Gascón research lab in the Chemistry department for their warm hospitality and support.

I would like to express my gratitude to all of my fellow Physics graduate students for establishing a collaborative educational environment. To my close friends J.C Sanders and Nolan Samboy, thank you for helping me through all the rough times and making the good times even better. I am grateful to my office-mates Han Chen, Sanka Piyadasa and Fu Chang-Sun for creating an amazing work atmosphere in P-210.

Finally I would like to thank my family for their unconditional love, and for everything they have done for me. It was not easy for me to leave my parents and relatives in India, and travel halfway across the globe to pursue my graduate education. I thank my parents and parent-in-laws for always being extremely supportive of everything. I would like to thank my close friends Swastik Ghoshdastidar and Piyal Das for always encouraging me to achieve even the farthest dreams; I miss you guys everyday. I was fortunate enough to have family members in US, I thank Saikat and Debjani Ray-Majumder my brother-in-law and sister-in-law for being so loving and caring, and of course their amazing kids Rishi and Arjun. I thank my cousin brother Siddhartha (Jubin) for telling me that life is not all about taking stress, it is about having fun too. Last but not the least, I would like to thank my lovely wife Jayita. Without her, my accomplishments would be nowhere near as fulfilling or satisfying.

Table of Contents

Page

Chapter

APPENDICES

List of Tables

List of Figures

Figure **Page**

Chapter 1

Introduction

1.1 Motivations

The field of atomic, molecular and optical (AMO) physics, has been ever growing, owing to development of both experimental and theoretical methods. Recent Nobel prizes [10, 11] in physics (2012), once again illustrates the importance of using quantum mechanics to study atoms and molecules. In this thesis, we study the electronic structure and properties alkaline-earth molecular ions. An alkaline-earth ionic dimer has three electrons in the valence shell, examples of the homonuclear species that we studied being Be_2^+, Mg_2^+, Ca_2^+ and Sr_2^+. Recent experiments [12] have been successful at cooling and controlling molecular ions. One of the major advantages of using alkaline earth ionic dimers is that the ion and the neutral atom can be imaged separately. This opens up a wide range of new possibilities both for experiments and theory to study processes like resonant charge transfer [6] and quantum information storage, owing to the large number of internal states which can be used as qubits.

A major interest in the AMO community lies in understanding the behavior of an atom/ion in the presence of other atom/ion(s). The quantum mechanical treatment of scattering theory, although being developed a long time back, has found new testing grounds with the advent of ultracold physics. Atom-ion scattering, at ultracold ($\sim \mu$K) temperatures [4, 5] is a topic of growing interest. As a staring point for such collisional studies one needs an accurate knowledge of the energetics of the participating atom/ions. A quantitative description for such a problem is often obtained from a numerical solution of the time-independent Schrödinger equation, which gives rise to potential energy surfaces (PES) describing the ground and excited states of the system.

The experimental realization of Bose-Einstein condensation (BEC) makes numerous applications involving charged atomic and molecular species possible. The cooling and trapping [13] of such charged gases at sub-kelvin temperatures is a topic of growing interest. Other emerging fields include ultracold plasmas [14], ultracold Rydberg gases [15], and systems involving ions in a BEC [16, 17]. Alkaline-earth dimers are now been used as new grounds for testing fundamental physics laws, precision measurements [8], and quantum computation [9].

In this thesis, we provide accurate *ab initio* calculations for the ground and low-lying excited states of alkaline-earth molecular ions. The reliability of such calculations for potential energy curves and properties depend on accurate and expensive quantum chemistry methods, like full configuration interaction (CI), and extended basis sets. We explore many different methods with appropriate basis sets to precisely describe electron-electron correlations for these molecular ions. We have also extended our calculations to study heteronuclear species of alkaline-earth molecular ions like BeCa^+, and mixed alkali alkaline-earth species like NaCa^+. We also show preliminary results for corrections to the Born-Oppenheimer Hamiltonian — non-adiabatic couplings and hyperfine structure due to nuclear spins and electric quadrupoles.

1.2 Overview of *ab initio* methodology

As the complexity of atoms and molecules increases, one has to rely on accurate quantum mechanical description to account for electron correlation. The primary task at hand is to find solutions to the time-independent Schrödinger equation,

$$H\psi = E\psi \,. \tag{1.1}$$

Very rarely can one find a simple enough system which can be exactly solved analytically. Most of the times, we rely on numerical solutions to the Schrödinger equation. If solutions are generated without reference to experimental data, the methods are usually called *ab initio* (latin: "from the beginning"), in contrast to other semi-empirical approaches. Electronic structure calculations — numerical solutions of Schrödinger's equation for a specific system — are distinct from other forms of modeling because they are first-principles in nature. That is the calculations contain no external parameters other than a most basic description of the system.

However, the numerical solution of the Schrödinger equation remains a difficult task. Exact solutions of the equation are only solvable in times scaling exponentially with system size. This scaling precludes exact calculations for all but the smallest and simplest of systems. Approximations may be introduced to reduce the equations to a form that can be solved in polynomial time, but at the penalty of losing some degree of accuracy and predictive power. The treatment of electron-electron interactions is the principle source of difficulty, the physical and chemical properties of a system depend principally on the interaction of the electrons with each other and with the atomic cores. These interactions cannot easily be separated out or treated without approximation.

1.2.1 Born-Oppenheimer approximation

The typical form of the Hamiltonian operator in Eq. (1.1) takes into account contributions from the kinetic energies of the electrons and nuclei, the attraction of the electrons to the nuclei, and the inter-electronic and internuclear repulsions. In more complicated situations, such as the presence of an external electric or magnetic field, significant spin-orbit coupling in heavy elements, large relativistic effects etc., other terms are required in the Hamiltonian. We will consider some of these at later chapters in this thesis, but for now we omit them to simplify the discussion.

The Hamiltonian H in Eq. (1.1) can be written as,

$$H = -\sum_i \frac{\hbar^2}{2m_e}\nabla_i^2 - \sum_k \frac{\hbar^2}{2m_k}\nabla_k^2 - \sum_i \sum_k \frac{e^2 Z_k}{r_{ik}} + \sum_{i<j} \frac{e^2}{r_{ij}} + \sum_{k<l} \frac{e^2 Z_k Z_l}{r_{kl}} \tag{1.2}$$

where i, j run over electrons, k and l run over nuclei, m_e is the mass of the electron, m_k is the mass of nucleus k, ∇^2 is the Laplacian operator, e is the charge on the electron, Z is an atomic number, and r_{ij} is the distance between particles i and j. As is evident from Eq. (1.2), the Hamiltonian contains pairwise interactions, implying that motion is correlated.

In order to simply the Hamiltonian, the most common and reasonable approximation is to decouple the motion of nuclei and electrons, by realizing that the protons and neutrons are $\sim$ 1800 times as massive as electrons. This separation of the electronic and nuclear degrees of freedom is known as the Born-Oppenheimer approximation. Under this approximation, we can compute electronic energies for fixed nuclear positions. Thus, the electronic Schrödinger equation becomes

$$(H_{el} + V_N(\boldsymbol{R}))\psi_{el}(\boldsymbol{R}) = E_{el}\psi_{el}(\boldsymbol{R})\,, \tag{1.3}$$

where $\psi_{el}(\boldsymbol{R})$ refers to the purely electronic wavefunction in the Born-Oppenheimer approximation. The eigenvalue of the electronic Schrödinger equation is called the "electronic energy". Note that $V_N(\boldsymbol{R})$ is constant for a given set of fixed nuclear coordinates.

The solution of Eq. (1.3) over all possible nuclear coordinates is defined as the potential energy surface (PES) for a given system. Fig. 1.1 illustrates a typical PES for a dimer as a function of internuclear separation R. Note that without the Born-Oppenheimer approximation, we would have lacked the entire concept of PES and derived properties like equilibrium and transition state geometries. So although this seems to be a simple approximation, the consequences are profound in the fields of physics and chemistry.

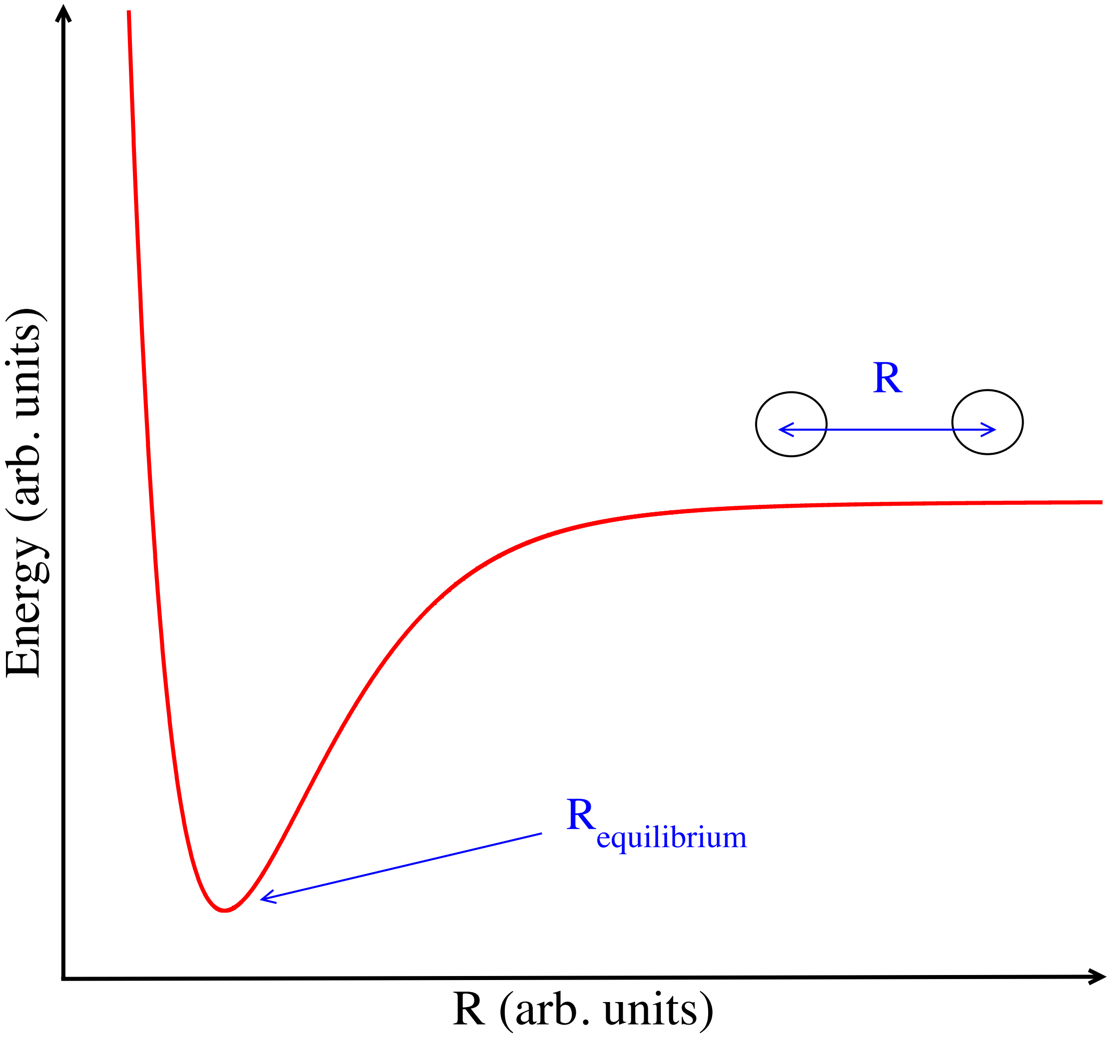

Figure 1.1. Schematic diagram of a potential energy surface.

1.2.2 Commonly used methods – Configuration Interaction and Coupled Cluster

The simplest and most basic solution to Schrödinger equation is provided by the Hartree theory, which states that the many-body wavefunction can be simply written as a direct product of one-electron wavefunctions,

$$\Psi_H = \psi_1 \psi_2 .... \psi_N \, . \tag{1.4}$$

Of course, such a drastic approximation does not necessarily obey Pauli exclusion principle, and is hence modified by anti-symmetrizing the wavefunction and expressing it as a Slater determinant. This is the Hartree-Fock (HF) theory. Unfortunately, even in the HF regime, there lacks an accurate account for electron correlation. The Hartree-Fock theory assumes each electron moves in the static electric field created by all of the other electrons, and then optimizes the orbitals for all of the electrons in a self-consistent fashion subject to a variational constraint.

So, the task remains to modify the HF wavefunction to obtain a lower electronic energy when we operate on that modified wavefunction with the many-body Hamiltonian. By the variational principle, such a construction would be a more accurate wavefunction for the given system. One of the obvious choices is to construct a wavefunction as a linear combination of multiple Slater determinants; instead of the HF single Slater determinant.

So the basic idea is to diagonalize the N-electron Hamiltonian in a basis of N Slater determinants. If the basis set is complete, we get the exact energies of ground and all excited states of the system. Such an approach is called "Configuration Interaction (CI)". The wavefunction can now be represented as

$$\mid \Phi_0\rangle = C_0 \mid \Psi_0\rangle + C_S \mid S\rangle + C_D \mid D\rangle + ... \,, \tag{1.5}$$

where, Ψ_0 represents the HF wavefunction, $|S\rangle$ represents all terms arising from single excitations from the HF reference wavefunction, $|D\rangle$ represents double excitations, and so on so forth. A full CI includes all possible excited configurations from the HF reference wavefunction. Although computationally expensive, a full CI together with an infinite basis set is the exact solution of non-relativistic Born-Oppenheimer time-independent Schrödinger equation.

In reality the size of the basis set is always restricted. However full CI always gives a very good description of the electron correlation. Many approximate methods are also developed using similar methodology as CI. In situations where a single HF wavefunction is not a good reference, one uses a multi-configuration self consistent field (MCSCF) wavefunction as a reference. The CI from such a reference is called multi-reference configuration interaction (MRCI).

Yet another method to estimate electron correlation is the "coupled cluster (CC)" method. The theory relies on the central equation that the full CI wavefunction can be written as

$$\psi = e^T \psi_{HF} \,, \tag{1.6}$$

where the cluster operator T is defined as

$$T = T_1 + T_2 + ... + T_n \,, \tag{1.7}$$

where n is the total number of electrons and the various T_i operators generate all possible determinants having i excitations from the reference. If one truncates the series in Eq.(1.6) to include only double excitations, a Taylor expansion gives

$$\psi = \Big(1 + T_2 + \frac{T_2^2}{2!} + ...\Big)\psi_{HF}\,, \tag{1.8}$$

which is different from the CI method, because there are terms involving T_2^2 giving quadruple excitations and T_2^3 giving hextuple excitations etc. These higher order excitations which are missing in the CI theory makes it non-size consistent.

The inclusion of single(S) and double(D) excitations define the CCSD method. Inclusion of triples (T_3) is usually computationally very expensive, so most often perturbative methods are used to estimate the contribution of connected triples. This very popular method is called CCSD(T), and is often referred to as the "gold standard" for single-reference calculations.

There is however no unique method that one can choose to be accurate for the description of any physical system. So we discuss more about these various quantum mechanical methods in the context of a particular system in the chapters to follow.

1.2.3 Basis sets

The basis set is the set of mathematical functions from which the wave function is constructed. Even in the simplest theory – Hartree Fock (HF) – wavefunctions are constructed from a linear combination of basis functions, the coefficients for which are determined from the iterative solution of the self-consistent field equations. The choice of a basis set is extremely crucial for the accurate description of a given system. The larger basis set entails more basis functions which becomes computationally expensive, although it provides a more accurate description of the system. Finally, it is of utmost importance that the basis functions must be chosen to have a form that is useful in a physical sense. That is, the functions should have large amplitudes in regions of space where the electron probability density ($|\psi|^2$) is also large, and small amplitudes where the probability density is small.

It has been now customary to use Gaussian-type orbitals (GTO) as basis functions, whose general form can be written as [18]

$$\phi(x,y,z,\alpha,i,j,k) = \left(\frac{2\alpha}{\pi}\right)^{3/4}\left[\frac{(8\alpha)^{i+j+k}i!j!k!}{(2i)!(2j)!(2k)!}\right]^{1/2} x^i y^j z^k e^{-\alpha(x^2+y^2+z^2)}\,, \tag{1.9}$$

where i, j and k are integers that dictate the nature of the orbital in a Cartesian sense; for example when all three of these indices are zero, the GTO has spherical symmetry, and is called an s-type GTO and so forth. Modern basis functions use a linear combination of such GTOs, as shown in Eq. (1.9), which are referred to as contracted GTOs. Of course, the development of the basis set does not end there. Polarization functions and diffuse functions are also added to such GTOs to make them more flexible. It must be noted that the choice of a basis set is extremely important for the accurate quantum mechanical description of a particular system. We shall postpone further discussion of development of basis set and implementation to the later chapters, and describe them in context of specific systems.

1.3 Outline of the Thesis

The division of this thesis is based on the physical system which is studied. Chapters 2 and 3 focus on the electronic structure calculations of the ground and excited states of the Be_2^+ molecular ion. We have also developed a photoassociation (PA) scheme to form ultracold Be_2^+ molecular ions. Chapter 4 is subdivided into sections, which discuss in detail electronic structure calculations in similar homonuclear alkaline-earth molecular ions — Mg_2^+, Ca_2^+ and Sr_2^+. We provide a comparative study of the potential energy curves in these systems and show preliminary results for non-adiabatic corrections in these molecular ions.

Chapters 5 and 6 focus on studies involving heteronuclear species of molecular ions: alkaline-earth and mixed alkali alkaline-earth systems. In Chapter 6, we discuss in detail the hyperfine spectrum of the ground singlet and triplet states of $NaCa^+$, arising from nuclear spins and electric quadrupoles.

Last but not the least, we discuss in Chapter 7 the application of quantum chemistry to the study of polyatomic molecular ions. Due to their many applications in physics, chemistry and materials science, we choose gold nano-clusters as our specimen to perform hybrid quantum mechanics (QM) and molecular mechanics (MM) calculations to study the electronic structure and properties of these complicated systems.

Chapter 2

The prototype example of Be_2^+

2.1 Ground X $^2\Sigma_u^+$ and B $^2\Sigma_g^+$ states

The first system in the family of homonuclear alkaline-earth molecular ions is Be_2^+. We calculate and analyze the ground X $^2\Sigma_u^+$ and B $^2\Sigma_g^+$ states in this chapter. In order to obtain potential energy curves for such a system, one must identify a suitable basis set and method to describe the problem. We begin by describing the methods used in our calculations followed by a discussion of the results which include the potential curves, spectroscopic constants, electronic transition dipole moments, lifetimes of the bound vibrational levels and the analysis of long-range behavior and determination of the Van der Waals coefficients.

As we have discussed in the previous chapter, the ideal goal from the quantum chemistry viewpoint is to solve the Born-Oppenheimer Schrödinger equation, with an infinite basis set at the full configuration interaction (FCI) level of theory. Realistically, however, the computational cost forces a limit on the size of the basis set and method used for any calculation of potential energy surfaces.

The Be_2^+ dimer is schematically shown in the diagram Fig. 2.1, comprising of the neutral Be atom and positively charged Be^+ ion separated by a distance R. The Be_2^+ dimer has seven electrons, four of which are in the atomic core orbitals. This implies

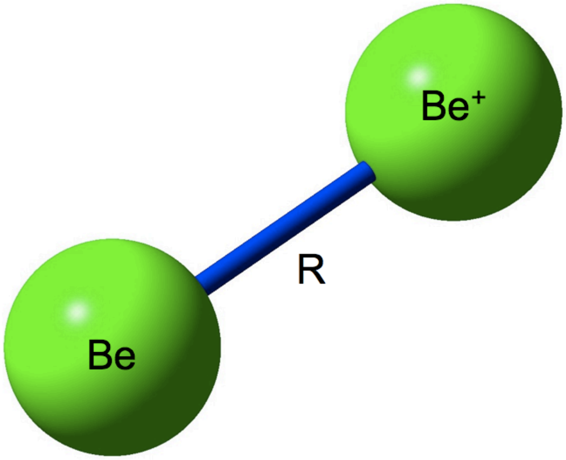

Figure 2.1. Schematic diagram of Be_2^+ dimer.

that the three valence electrons form an open shell doublet for the ground state of the system. Historically, Be_2 dimer has been a difficult problem for quantum chemistry, due to the $2s - 2p$ near degeneracy in the beryllium atom [19]. At large separations, the behavior of the molecule is dominated by the behavior of the constituent atom/ ions. Thus the near-degeneracy problem in Be atom also exists in the Be_2^+ dimer.

As a consequence of the nearly degenerate $2s$ and $2p$ orbital energies, the B $^2\Sigma_g^+$ state displays a multi-reference character. We show below the dominant molecular orbital (MO) configurations for both X $^2\Sigma_u^+$ and B $^2\Sigma_g^+$ states of the Be_2^+ dimer.

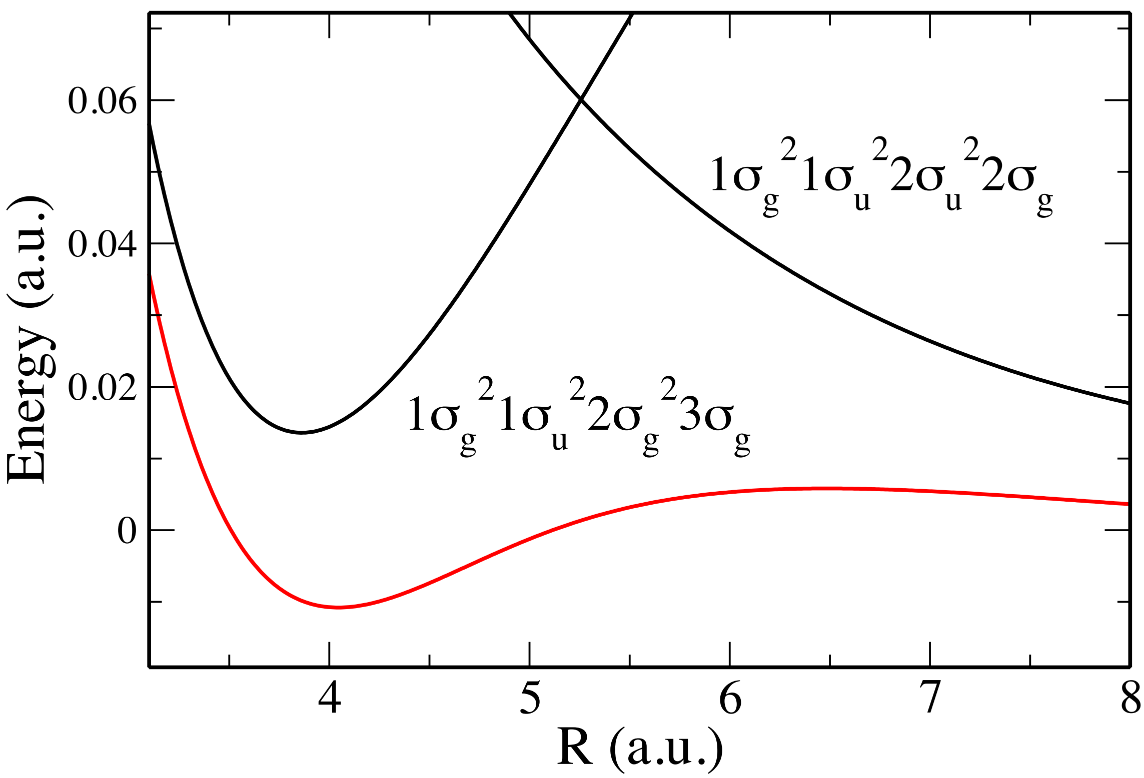

Figure 2.2. Dominant molecular orbital configurations in the B $^2\Sigma_g^+$ state. The curves in black shows the SCF curve crossings due to the change of the occupied molecular orbitals, whereas the curve in red shows the calculated FCI potential curve for the B $^2\Sigma_g^+$ state.

X $^2\Sigma_u^+$ state

MO configuration: $1\sigma_g^2 1\sigma_u^2 2\sigma_g^2 2\sigma_u$

B $^2\Sigma_g^+$ state

MO configuration 1: $1\sigma_g^2 1\sigma_u^2 2\sigma_g^2 3\sigma_g$

MO configuration 2: $1\sigma_g^2 1\sigma_u^2 2\sigma_u^2 2\sigma_g$

The multi-reference character of the B $^2\Sigma_g^+$ state was first reported by Fischer *et al.* [20]. This behavior of competing MO configurations is usually caused by near degeneracies of atomic energies and strong interactions with an excited $^2\Sigma_g^+$ state. The multi-reference nature of the B $^2\Sigma_g^+$ state is depicted in Fig. 2.2. At short internuclear separation, the dominant configuration is $1\sigma_g^2 1\sigma_u^2 2\sigma_g^2 3\sigma_g$ while at large separation it becomes $1\sigma_g^2 1\sigma_u^2 2\sigma_u^2 2\sigma_g$. As shown in Fig. 2.2, the calculated self-consistent field (SCF) energies, show a curve crossing where the MO configuration changes.

2.2 Computational Details

Typically, for calculation of potential energy curves, one starts with a Hartree Fock (HF) reference wavefunction and build on additional electron-electron interactions for a more quantitative description of a real system. In this case however, a single HF reference is not a good description of the system at all regions of potential energy curve. This fact is also reflected in a preliminary calculation done at the CCSD(T) level of theory, which finds a discontinuity in the potential curve for the B $^2\Sigma_g^+$ state at the SCF curve crossing (see Fig. 2.3). Valence full configuration interaction (FCI) calculations were found to give a smooth potential curve.

Therefore our computational approach is to perform valence FCI using the augmented correlation consistent polarized valence n-tuple zeta (aug-cc-pVnZ) basis set of Dunning [21]. In order to use FCI method, one still has to rely on HF reference wavefunctions. In the case of the B $^2\Sigma_g^+$ state of the Be_2^+ dimer, we calculate the SCF energy at every interatomic separation (R), using both MO configurations. Since SCF is a variational approach, the lower energy among the two SCF calculations corresponds to the correct occupation of the orbitals. Keeping this in mind, we use the correct SCF reference for the valence FCI calculations. The alternate approach for this calculation was to use a complete active space (CAS) wavefunction as a reference

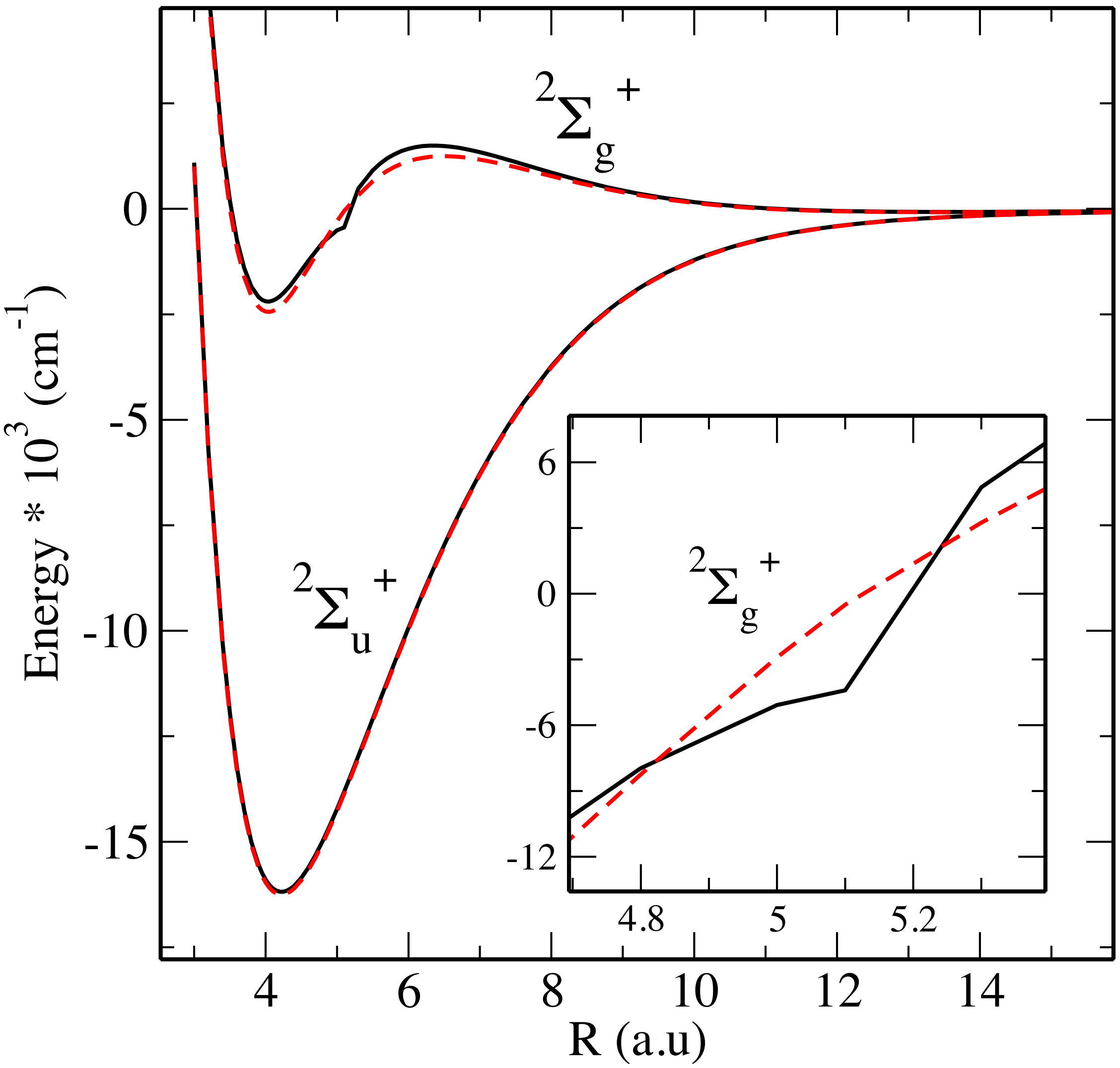

Figure 2.3. The curves in black show a CCSD(T) calculation done with aug-cc-pV5Z basis set, whereas the curves in red are a full CI calculation using the same basis set. The inset shows a discontinuity (black line) in the CCSD(T) curve for the B $^2\Sigma_g^+$ state due to the change in reference configuration at larger internuclear separation.

for a multi-reference configuration interaction (MRCI) calculation.

The choice of basis set is one of the most crucial aspects of any quantum chemistry calculation. Since Be_2^+ is a light system, owing to only 7 electrons, we choose a large basis set of quadruple (QZ) and quintuple zeta (5Z) quality for our calculations. The 5Z basis set would simply mean that it includes "h" angular momentum functions (s corresponds to $n = 0$, p to $n = 1$ and so forth). The 5Z basis set contains $14s$, $8p$, $4d$, $3f$, $2g$ and $1h$ Gaussian type angular momentum functions, which are contracted to $6s$, $5p$, $4d$, $3f$, $2g$, $1h$ functions. We show below an example of the cc-pV5Z basis set for Be_2^+ in MOLPRO program format. The exponents are indicated by the corresponding angular momentum function (s,p,d...) and the contraction coefficients are indicated by "c". This implies that for the cc-pV5Z basis set, there are 14 s-type functions and 10 contraction coefficients, representing the $1s$ and $2s$ core of Be_2^+ and similarly for other angular momentum functions.

```
basis={
!
! cc-pV5Z Basis Set from EMSL library
! BERYLLIUM        (14s,8p,4d,3f,2g,1h) -> [6s,5p,4d,3f,2g,1h]
!
s, BE , 54620.0000000, 8180.0000000, 1862.0000000, 527.3000000,
172.0000000, 62.1000000, 24.2100000, 9.9930000, 4.3050000,
1.9210000, 0.8663000, 0.2475000, 0.1009000, 0.0412900
c, 1.10, 0.0000180, 0.0001380, 0.0007230, 0.0030390, 0.0109080,
0.0340350, 0.0911930, 0.1992680, 0.3293550, 0.3404890
c, 1.10, -0.0000030, -0.0000250, -0.0001310, -0.0005580, -0.0019880,
-0.0063700, -0.0172170, -0.0408580, -0.0742370, -0.1192340
c, 11.11, 1
c, 12.12, 1
c, 13.13, 1
c, 14.14, 1
p, BE , 43.7500000, 10.3300000, 3.2260000, 1.1270000, 0.4334000,
0.1808000, 0.0782700, 0.0337200
c, 1.4, 0.0006330, 0.0048080, 0.0205270, 0.0678160
c, 5.5, 1
c, 6.6, 1
c, 7.7, 1
c, 8.8, 1
d, BE , 1.6350000, 0.7410000, 0.3350000, 0.1519000
c, 1.1, 1
c, 2.2, 1
c, 3.3, 1
c, 4.4, 1
f, BE , 0.6860000, 0.4010000, 0.2350000
c, 1.1, 1
c, 2.2, 1
c, 3.3, 1
g, BE , 0.6030000, 0.3240000
c, 1.1, 1
c, 2.2, 1
h, BE , 0.5100000
c, 1.1, 1
}
```

Clearly more exponents in each angular momentum function and more angular momentum functions would mean a better and much accurate description of the real system. Since computational time scales very quickly with the total number of basis functions, one is usually limited to a finite basis set. The core electrons are better described by tight Gaussian exponents (larger values) whereas the valence electrons are described accurately with diffuse exponents (smaller values). The role of such

Table 2.1. Additional diffuse functions added to cc-pV5Z basis set.

Orbitals	Exponents	Contraction coefficients
s	0.013777	1.0
p	0.007668	1.0
d	0.077200	1.0
f	0.013750	1.0
g	0.174000	1.0
h	0.225000	1.0

diffuse (augmented) functions is also extremely crucial in describing the valence electrons at large interatomic separations. Since we are also interested in studying the long-range behavior of these systems, we need good diffuse functions in our basis set. The published quintuple zeta basis set, did not have any augmented basis functions, hence we derive the exponents by a continuation of even-tempered exponents for each angular momentum functions. Table 2.1 shows the augmented basis functions derived for the 5Z basis set.

In order to reach the goal of solving Schrödinger equation with an infinite basis set, one approach that is often used is to extrapolate the results from a finite basis set calculation to the complete basis set (CBS) limit. In order to use this approach, we utilize our results from the aug-cc-pVQZ and aug-cc-pV5Z basis set. For extrapolating the SCF energies, we have used Schwenke's linear formula [22],

$$E_{SCF}^{ex} = E_{SCF}^{X} + \alpha[E_{SCF}^{Y} - E_{SCF}^{X}]\,, \tag{2.1}$$

where E_{SCF}^{X} and E_{SCF}^{Y} correspond to the SCF energies calculated with aug-cc-pVQZ and aug-cc-pV5Z basis sets respectively. The Schwenke extrapolation coefficient α is determined by fitting to accurate benchmark calculations; for our choice of basis sets $\alpha = 1.1099137$. For extrapolating the FCI correlation energies we have used the following formula given by Helgaker [23],

$$E_{FCI}^{ex} = \frac{X^3 E_X^{corr} - Y^3 E_Y^{corr}}{X^3 - Y^3}\,, \tag{2.2}$$

where X, Y are 4, 5 corresponding to the aug-cc-pVQZ and aug-cc-pV5Z basis sets. The total valence energy is given by the sum of the extrapolated SCF and FCI energies,

$$E_{valence} = E_{SCF}^{ex} + E_{FCI}^{ex}\,. \tag{2.3}$$

The total valence energy obtained from extrapolation of the basis sets was numerically very close to the valence energy obtained purely from a full CI calculation with a 5Z basis set. This suggests that results from the 5Z calculation were very close to being converged. The CBS extrapolation increased the well depths of the X $^2\Sigma_u^+$ and B $^2\Sigma_g^+$ states by ~ 40 cm^{-1}, however the dissociation energy for the outer well in the B $^2\Sigma_g^+$ state was unchanged. Now the total energy of the Be_2^+ dimer is given by,

$$E_{total} = E_{valence} + E_{core-valence}\,, \tag{2.4}$$

where $E_{valence}$ is the total valence energy obtained earlier and $E_{core-valence}$ is the correction to the valence energy from interactions of the valence electrons to the core and the interactions among the core electrons. Core-core (CC) and core-valence (CV) correlations were calculated as the difference between all-electron and frozen core CCSDT [24] calculations done with Martin's MTsmall basis set [25]. The MTsmall basis set consists of a completely uncontracted cc-pVTZ basis set augmented with two tight d and one tight f functions. For a three electron valence system, the coupled-cluster with singles, doubles and triples (CCSDT) is equivalent to full CI. The all electron calculations were very expensive computationally and took $\sim$ 8 hours for a single point energy calculation. Scalar relativistic corrections were estimated to be $\sim$ 10 cm^{-1} and are neglected.

In quantum chemistry, calculations using finite basis sets are susceptible to basis set superposition error (BSSE). As the atom/ ion of the Be$_2^+$ molecular ion approach one another, their basis functions overlap. Each monomer borrows functions from other nearby components, effectively increasing its basis set and improving the calculation of derived properties such as energy. If the total energy is minimized as a function of the system geometry, the short-range energies from the mixed basis sets must be compared with the long-range energies from the unmixed sets, and this mismatch introduces an error. We correct for the effects of BSSE by the counterpoise method of Boys and Bernardi [26]. In the counterpoise method the BSSE is calculated by re-performing all the calculations using the mixed (dimer) basis sets, and the error is then subtracted a posteriori from the uncorrected energy. The mixed basis sets for the individual atom/ion are realized by introducing ghost (dummy) orbitals, i.e, basis set functions which have no electrons or protons.

The FCI calculations were done using the `MOLPRO` [27] and `PSI3` [28] electronic structure programs running on a Linux workstation (2 quad core Intel Xeon E5520

CPU). The DETCI program in `PSI3` was much faster in comparison to the CI program of `MOLPRO`, thus we used `PSI3` for computing the valence energies with the larger 5Z basis sets. The core-core and core-valence corrections were done with the multi-reference coupled cluster (`MRCC`) program [29] of M. Kállay as implemented using the `MOLPRO` program. Examples of input files for calculations of potential energy curves using the different programs have been provided in Appendix A.1.

Le Roy's `LEVEL` program [30] has been used to calculate the bound vibrational levels, Franck-Condon factors and Einstein A-coefficients. Using these Einstein A-coefficients we were able to calculate the lifetimes of all vibrational levels of the B $^2\Sigma_g^+$ state. A sample input and output file of the `LEVEL` program are provided in Appendix B.1.

2.3 Results and Discussions

2.3.1 Potential Curves and Spectroscopic Constants

Fig. 2.4 shows the *ab initio* potential curves for the lowest $^2\Sigma_u^+$ and $^2\Sigma_g^+$ states of Be_2^+. These were obtained by the methodology described in the previous section. The most interesting feature of the ground states of the Be_2^+ dimer is that the B $^2\Sigma_g^+$ state has a double minima.

This double-well nature of the B $^2\Sigma_g^+$ state has been seen in other alkaline-earth molecular ions as well. This is discussed in detail, in Chapter 4 where a comparison is made to other alkaline-earth systems. The nature and strength of interaction of the B $^2\Sigma_g^+$ state with the next excited state of this symmetry 2 $^2\Sigma_g^+$, is crucial in understanding the double-well potential energy curve. In the B $^2\Sigma_g^+$ state, the two

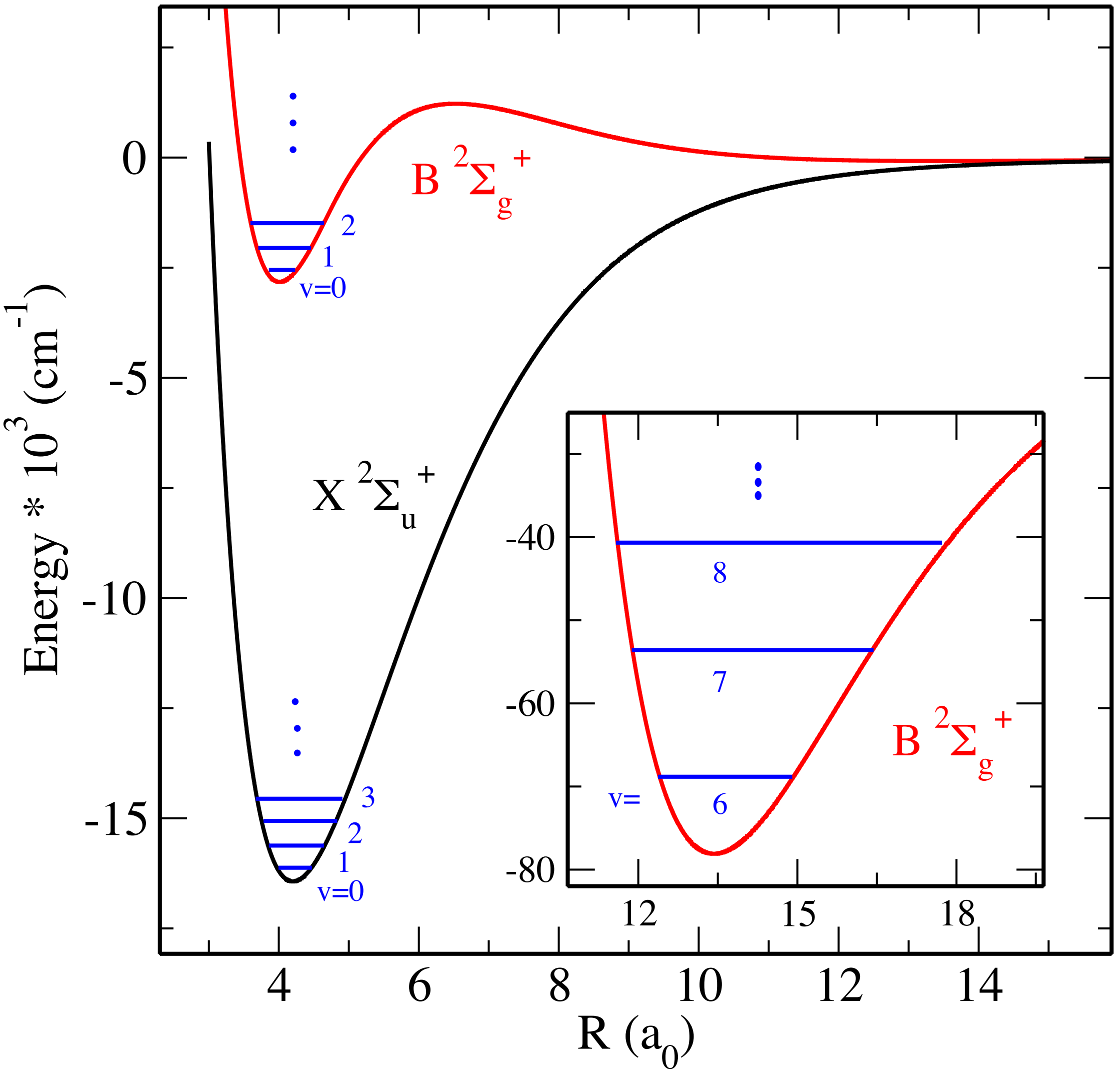

Figure 2.4. The figure shows the calculated *ab initio* potential curves of Be_2^+. The inset is a magnification of the shallow long-range well in the B $^2\Sigma_g^+$ state (in red). The positions of the first few bound vibrational levels are shown (in blue) for both states of the $^9Be_2^+$ dimer. Note that the energy scale for the inset is in cm^{-1}.

wells are widely separated by $\sim$ 5 Å. Both wells support bound vibrational states. We have calculated the radiative lifetimes of the bound levels in the B $^2\Sigma_g^+$ state, and found that the 12 bound levels in the shallow outer well are long lived ($\sim$ ms) compared to the ones in the deeper inner well ($\sim$ μs).

We use a standard Dunham analysis [31] to calculate the spectroscopic constants (Table 2.2). The minima for each potential well is approximately identified and 10 points each at a successive internuclear separation of 0.01 Å for both increasing and decreasing R are calculated. The potential well comprising of 21 points is fitted with

$$V(x) = V_0 + a_0\rho(x)^2[1 + a_1\rho(x) + a_2\rho(x)^2 + ...]\,, \tag{2.5}$$

where

$$\rho(x) = \frac{x - r_e}{r_e}\,, \tag{2.6}$$

and the coefficients a_0, a_1 etc. are the Dunham expansion coefficients. Although the Dunham series is an infinite series, it converges very fast and for all practical purposes one can terminate it keeping the fourth order coefficient without any loss of accuracy. V_0 is the value of the potential energy (in atomic units) at r_e. From the Dunham analysis, we calculate the spectroscopic constants r_e, B_e, ω_e and $\omega_e x_e$. The calculated spectroscopic constants are shown in Table 2.2. Unfortunately, there has not been any experimental measurement for the B $^2\Sigma_g^+$ state, so we could only compare the spectroscopic constants of the X $^2\Sigma_u^+$ against recent experiments. The agreement with the experimental values is extremely good and we believe that the values for the B $^2\Sigma_g^+$ state have a similar accuracy since the *ab initio* methods for calculating both states were the same. The X $^2\Sigma_u^+$ state supports approximately 70 bound vibrational levels,

Table 2.2. Calculated spectroscopic constants of Be_2^+

State	r_e (Å)	B_e (cm^{-1})	ω_e (cm^{-1})	$\omega_e x_e$ (cm^{-1})	D_e (cm^{-1})
$\mathrm{X}^2\Sigma_u^+$	2.221	0.756	525.299	4.454	16435
Exp. [32]	2.21(8)		525.88(18)	4.44(3)	16438(5)
$\mathrm{B}^2\Sigma_g^+$ (Inner)	2.123	0.829	547.452	11.681	2550
$\mathrm{B}^2\Sigma_g^+$ (Outer)	7.106	0.074	33.703	3.548	79

while the inner and outer wells of the B $^2\Sigma_g^+$ state support 5 and 13 levels, respectively.

2.3.2 Transition Moments and Lifetimes

For homonuclear molecules like Be_2^+, there is no permanent dipole moment. However there are transitions between different electronic states which are dipole allowed. To compute the electronic dipole transition moments coupling the X $^2\Sigma_u^+$ and B $^2\Sigma_g^+$ states of Be_2^+, we have used a 16 orbital complete active space self consistent field (CASSCF) wavefunction as a reference for performing multi-reference configuration interaction (MRCI) calculations. The core-valence contribution to the electronic transition moment is found to be negligible and hence omitted in the present calculations.

The transition dipole moments have been calculated using `MOLPRO`. Of the many possible methods to calculate transition moments using the CI code in `MOLPRO`, two are particularly useful. In the first/direct method, we can reduce the symmetry of the system to C_{2v} from D_{2h}. As a result of this, both the X $^2\Sigma_u^+$ and B $^2\Sigma_g^+$ states can now be described by the same symmetry operator A_1. Thus, we can simultaneously solve for two roots of the A_1 symmetry, and extract the transition moment as a function of internuclear separation R from the CI output in `MOLPRO`. The second and more general method is to store the electronic wavefunctions of the corresponding states of respective symmetries into separate files, and then in the next step calculate the transition dipole moment between those different symmetry states. An example of transition moment calculation is provided in Appendix A.3.

The transition moment for electric dipole transitions is defined as

$$\mu_{XB}(R) = \langle B \,|\, er \,|\, X \rangle \,, \tag{2.7}$$

where $|X_u\rangle$ and $|B_g\rangle$ are the electronic wave functions corresponding to the states X $^2\Sigma_u^+$ and B $^2\Sigma_g^+$ when the two Be nuclei are separated by the distance R. Fig. 2.5 shows a plot of the computed electronic dipole transition moment between the B $^2\Sigma_g^+$ and X $^2\Sigma_u^+$ ground states of Be_2^+. The curve shows a zero-crossing at around 5.5 a_0 which is approximately the same distance at which the dominant molecular orbital configuration changes from $(1\sigma_g^2\, 1\sigma_u^2\, 2\sigma_g^2\, 3\sigma_g)$ to $(1\sigma_g^2\, 1\sigma_u^2\, 2\sigma_u^2\, 2\sigma_g)$ in the B $^2\Sigma_g^+$ state of Be_2^+ (Fig. 2.2).

The transition moment μ_{XB} asymptotically follows the classical dipole behavior, $\mu_{XB} \sim R/2$ [33, 34], and we observe this behavior in the calculated curve (Fig. 2.5). This is understood by noting that for large R, the electron is localized on either one of the Be nuclei labeled A and B, respectively located at $\pm R/2$ from the geometric center on the molecular axis. The *gerade* and *ungerade* symmetries are well approximated

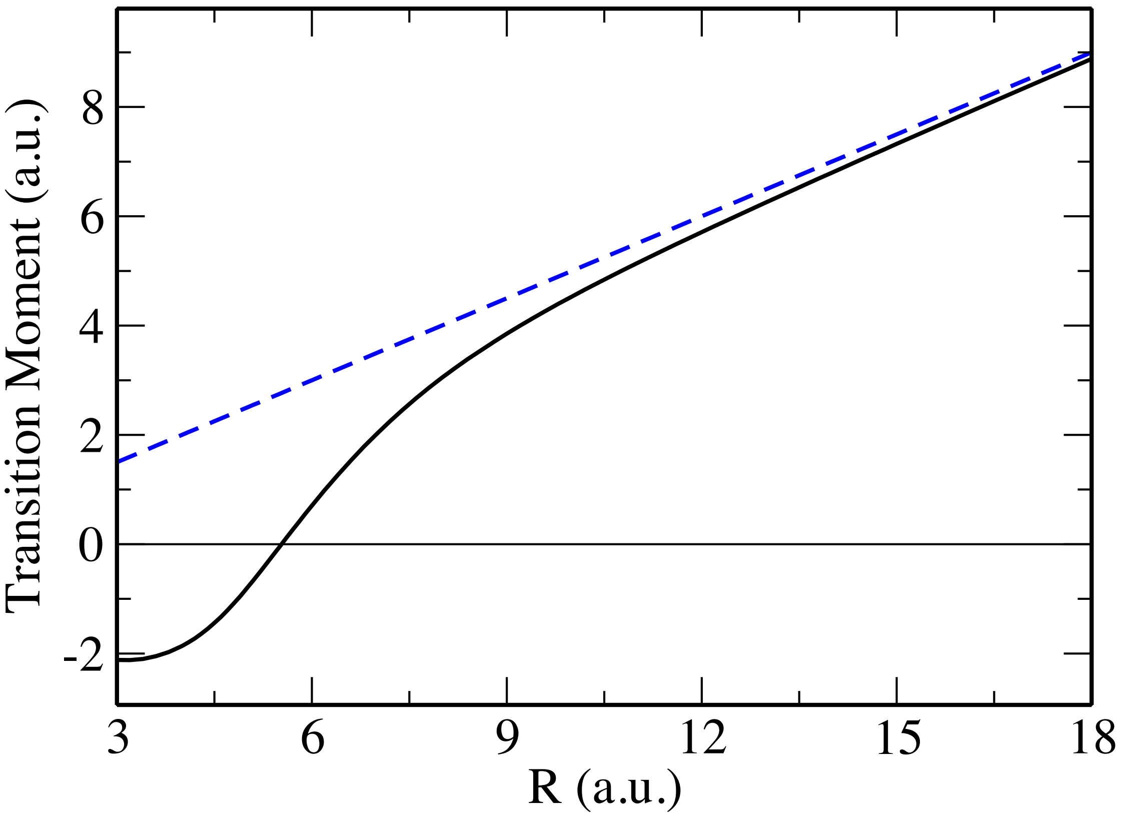

Figure 2.5. The figure shows a plot of the computed electronic dipole transition moment μ_{XB} coupling the B $^2\Sigma_g^+$ to the X $^2\Sigma_u^+$ state. The dotted line (in blue) shows R/2.

by an even and odd combination of states with the electron centered on A or B, *i.e.* $|B_g\rangle \sim \frac{1}{\sqrt{2}}\left(|A\rangle + |B\rangle\right)$ and $|X_u\rangle \sim \frac{1}{\sqrt{2}}\left(|A\rangle - |B\rangle\right)$, so that

$$\mu_{XB} = \langle B_g|z|X_u\rangle \; = \frac{1}{2}\left[\langle A|z|A\rangle - \langle B|z|B\rangle\right] \sim \frac{R}{2}\,, \tag{2.8}$$

where we put $e = 1$ in atomic units and omitted the cross terms because the overlap between the electronic wave functions centered of A and B are vanishingly small at large R. Since $\boldsymbol{r} \sim \pm R/2\hat{\boldsymbol{e}}_{\boldsymbol{R}}$ is constant, then $\langle A|\boldsymbol{r}|A\rangle \sim R/2$ and $\langle B|\boldsymbol{r}|B\rangle \sim -R/2$, leading to $\mu_{XB} \sim R/2$. We note that although the transition moment grows linearly with R, the probability of spontaneous transition will tend to zero since it is proportional to ν_{XB}^3, which vanishes exponentially as $R \to \infty$.

The calculated potential curves and the electronic transition dipole moments were used as input to Le Roy's `LEVEL` program to calculate the Einstein A-coefficients coupling the vibrational bound levels of the B $^2\Sigma_g^+$ state to the X $^2\Sigma_u^+$ state. We have also calculated the radiative lifetimes (Table 2.3) of the vibrational levels in the B $^2\Sigma_g^+$ state using these Einstein A-coefficients. Note that the bound levels in the shallow outer well are extremely long-lived ($\sim 10^{-3}$ s) in comparison to the levels in the inner well ($\sim 10^{-7}$ s). Our results for $v' = 0$ - 3 agree well with the results of Fischer *et al.* [20].

Table 2.3. Radiative lifetimes of the vibrational levels of the B $^2\Sigma_g^+$ state (in s) for $^9\mathrm{Be}_2^+$.

v'	B $^2\Sigma_g^+ \rightarrow$ X $^2\Sigma_u^+$
0	0.849×10^{-7}
1	0.937×10^{-7}
2	1.032×10^{-7}
3	1.161×10^{-7}
4	1.423×10^{-7}
5	1.539×10^{-7}
6	2.870×10^{-3}
7	1.861×10^{-3}
8	1.586×10^{-3}
9	1.557×10^{-3}
10	1.992×10^{-3}
11	1.840×10^{-3}
12	2.340×10^{-3}
13	3.382×10^{-3}
14	5.277×10^{-3}
15	10.067×10^{-3}
16	25.718×10^{-3}
17	97.361×10^{-3}

2.3.3 Long-Range Coefficients

For large internuclear separations, the long-range form of the intermolecular potential is

$$V_{LR}(R) = V_\infty - \frac{(\alpha_d/2)}{R^4} - \frac{(\alpha_q/2 + C_6')}{R^6} - ... \pm E_{exch} \, , \tag{2.9}$$

where E_{exch} is the exchange energy contribution and V_∞ is the asymptotic energy (which we have set to zero). Note that α_d is the static dipole polarizability, α_q is the static quadrupole polarizability, and C_6' is the dispersion coefficient. The ± sign in E_{exch} (see Section 4.7) corresponds to the ${}^2\Sigma_g^+$ and ${}^2\Sigma_u^+$ states, respectively.

All the parameters in Eq. (2.9) are common for both the X ${}^2\Sigma_u^+$ and B ${}^2\Sigma_g^+$ states. Neglecting higher order terms in Eq. (2.9), and adding the potentials for both states, the exchange term cancels and we get

$$-\frac{(V_g + V_u)}{2} \times R^4 = (\alpha_1/2) + \frac{(\alpha_2/2 + C_6')}{R^2} \, . \tag{2.10}$$

We have performed finite-field CCSD(T) calculations with the aug-cc-pV5Z basis set using `MOLPRO` to obtain the values of the static atomic dipole and quadrupole polarizabilities. We get $\alpha_d = 38.12$ a.u. and $\alpha_q = 300.01$ a.u. which are in excellent agreement with previous results [35]. Using α_d and α_q, we can numerically fit the value of dispersion coefficient C_6', using Eq. (2.10). From the fit we get $C_6' = 124.22$ a.u. This is in good agreement with unpublished results of Mitroy [36]. Table 2.4 lists the values of the long-range coefficients.

Table 2.4. Long-Range Coefficients for both X $^2\Sigma_u^+$ and B $^2\Sigma_g^+$ states (in a.u.)

	α_d	α_q	C_6'
This work	38.12	300.01	124.23
Previous [35]	37.76	300.98	
Previous [36]			119.99

2.4 Concluding Remarks

Accurate *ab initio* calculations have been performed to compute the X $^2\Sigma_u^+$ and B $^2\Sigma_g^+$ states of the Be_2^+ dimer. Since the B $^2\Sigma_g^+$ state has a shallow well near 13.4 bohr, it was necessary to include diffuse functions in the basis sets to describe the well accurately. Large augmented basis sets of the Dunning correlation consistent series were thus chosen and the results were also extrapolated to the complete basis set limit. We have corrected our valence only FCI results for core-core and core-valence effects using CCSDT calculations with both full and frozen core using Martin's MTsmall basis set.

Since the B $^2\Sigma_g^+$ state has not been experimentally observed we were unable to compare our theoretical values for dissociation energies or spectroscopic constants [32]. However there are recent experimental results for the X $^2\Sigma_u^+$ state which compare very well with our calculated results.

Chapter 3

Excited States in Be_2^+ dimer — An application to Photoassociation

3.1 Low lying asymptotes in Be_2^+

In the previous chapter, we have discussed the *ab initio* calculations of the ground X $^2\Sigma_u^+$ and B $^2\Sigma_g^+$ states of the Be_2^+ dimer. Both these ground states originate from the same long-range asymptote comprising of the Be neutral atom and the Be^+ ion in their respective ground states. Now, there may be a situation in which either of the neutral atom or the ion or both can be in an electronically excited state. In this chapter, we shall consider first order (single photon) excitations of both the Be neutral atom and the Be^+ ion, and calculate the family of excited state potential energy curves in the Be_2^+ dimer.

We first note down the excitations of the neutral atom and ion, and map the energetics of the system. Typically, the atomic and ionic excitation energies are well known and listed in the NIST atomic spectral database. The first and most important task to calculate electronically excited states from the *ab initio* perspective is to make sure whether one can reproduce the known atomic/ionic excitation energies.

The next task is to list down the different symmetries of the electronically excited atom or ions. This is important because the different symmetry operations would

Table 3.1. The lowest three asymptotes of Be_2^+. Also note that we have referred to the $1^2\Pi_u$ state † (in Channel II below) as $\mathrm{A}^2\Pi_u$ in the remainder of this chapter.

Channel	Asymptote	Molecular states
I	$\mathrm{Be}(^1\mathrm{S}_g) + \mathrm{Be}^+(^2\mathrm{S}_g)$	$\mathrm{X}\ ^2\Sigma_u^+$, $\mathrm{B}\ ^2\Sigma_g^+$
II	$\mathrm{Be}(^3\mathrm{P}_u) + \mathrm{Be}^+(^2\mathrm{S}_g)$	$1\ ^2\Pi_{g,u}{}^\dagger$, $2\ ^2\Sigma_{g,u}^+$
		$1\ ^4\Sigma_{g,u}^+$, $1\ ^4\Pi_{g,u}$
III	$\mathrm{Be}(^1\mathrm{S}_g) + \mathrm{Be}^+(^2\mathrm{P}_u)$	$3\ ^2\Sigma_{g,u}^+$, $2\ ^2\Pi_{g,u}$

quantify the number of potential energy curves arising from the different excited asymptotes. For example, in the case of the ground state asymptote, we have

$$\mathrm{Be}(^1\mathrm{S}_g) + \mathrm{Be}^+(^2\mathrm{S}_g) \rightarrow {}^2\Sigma_{u,g}^+ \quad .$$

Therefore, a combination of singlet sigma and doublet sigma states would give rise to doublet sigma states of both gerade and ungerade symmetry. Similarly, we list down the other combinations of single excitation of Be and Be^+. The three lowest asymptotes for Be_2^+ are shown in Table 3.1.

3.2 *Ab inito* curves for Excited States

We have calculated all the doublet and quartet states arising from the lowest asymptotes of Be_2^+. The potential energy curves of all doublet states corresponding to the three lowest asymptotes of Table 3.1 are shown in Fig. 3.1. The only asymptote

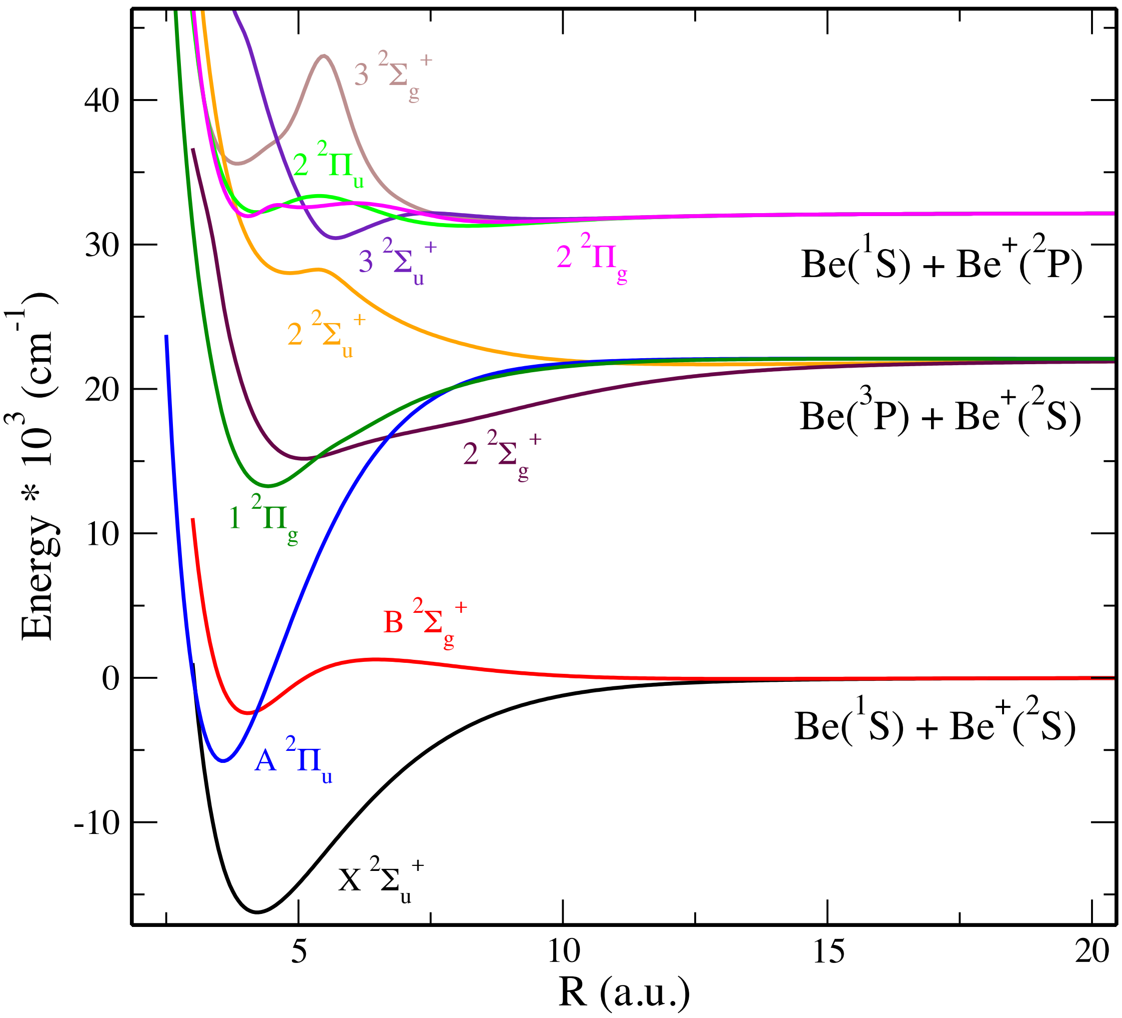

Figure 3.1. Calculated potential curves for low-lying doublet Σ and Π states of Be_2^+.

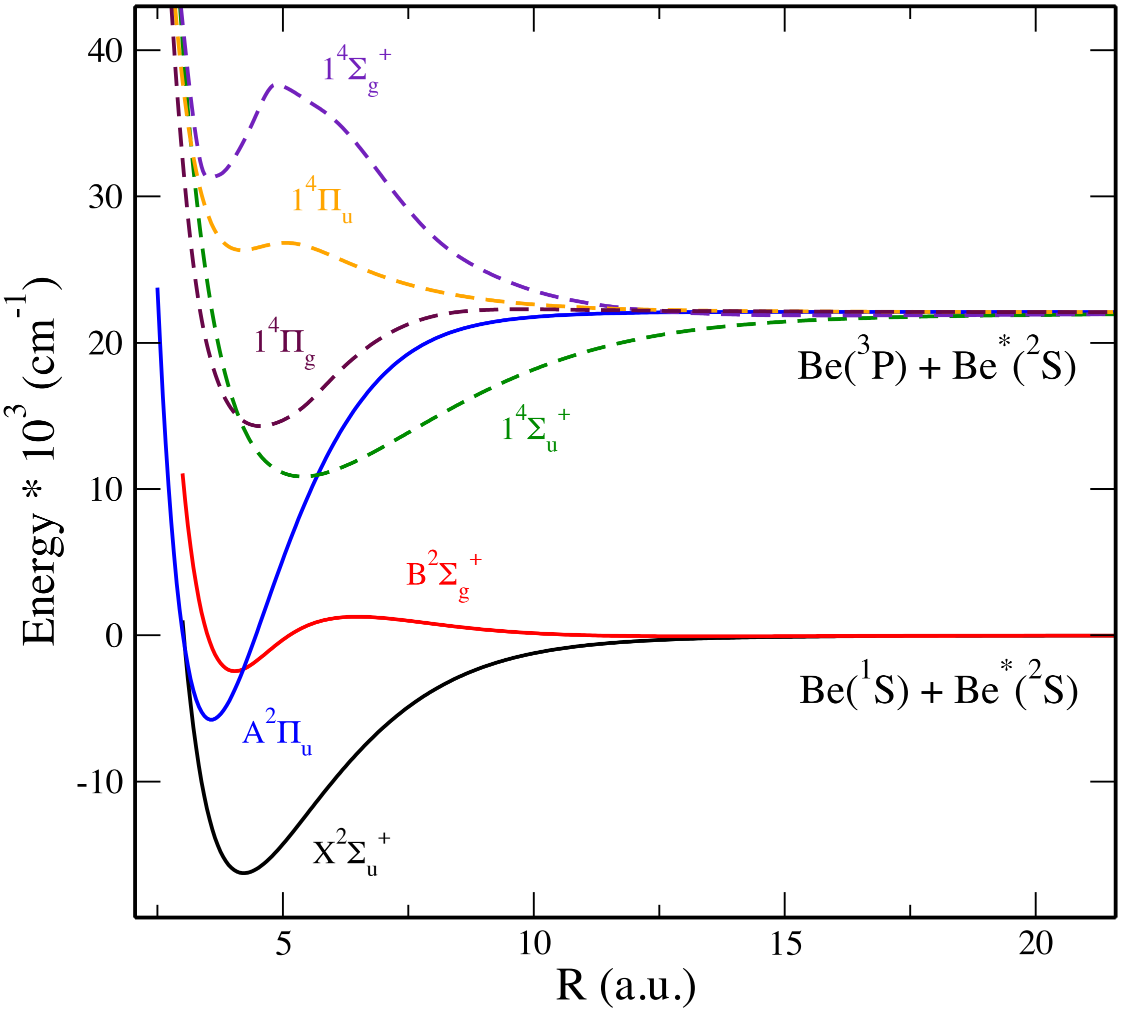

Figure 3.2. Calculated potential curves for low-lying quartet Σ and Π states of Be_2^+.

which gives rise to quartet electronic states (shown in Fig. 3.2) is denoted by "II" in Table 3.1; it arises from the combination of Be atom in excited $^3\mathrm{P}_u$ state and Be^+ in ground $^2\mathrm{S}_g$ state. The *ab initio* calculations were performed using `MOLPRO` with valence full configuration interaction (FCI) and the aug-cc-pV5Z basis set of Peterson [37, 38]. Similar results have been obtained previously by Meng, Bruna, and Wright [39, 40].

3.3 Theoretical background on photoassociation (PA)

In the previous section, we have calculated excited states of the Be_2^+ dimer, from asymptotes comprising of single photon excitations of the Be neutral atom and Be^+ ion. The excited states of a molecular ion are important for many reasons. Apart from studying avoided crossings and perturbations from higher states, they are of particular interest for formation of cold and ultracold molecular ions. One of the approaches in such experiments is to use the excited states as an intermediate step to form cold molecular ions into their lowest vibrational state.

The cooling and trapping [13] of molecular ions at sub-kelvin temperatures is a topic of growing interest. Several techniques like buffer-gas cooling and Stark decelerators [41] have been developed to obtain cold neutral molecules. A popular method for the formation of stable ultracold neutral molecules in the lowest rovibrational levels is from the photoassociation (PA) of ultracold atoms [42], where two colliding atoms absorb a photon to form a molecule. Schematically this is shown as

$$X + Y + h\nu \rightarrow (XY)^* \,. \tag{3.1}$$

Over the last several years, PA has been widely used to study molecular formation and long-range interactions. Such studies have a wide range of applications in metrology, molecular spectroscopy, precision measurements and quantum computing [9]. Formation of ultracold alkali dimers (both homonuclear and heteronuclear) have been explored in detail both experimentally and theoretically. More recently [43] alkaline earth dimers like Be_2 have also been studied in detail. One of the major advantages of using alkaline earth ionic dimers is that the ion and the neutral atom can be imaged separately. This opens up a wide range of possibilities both for experiments and theory for processes like resonant charge transfer [6] and quantum information storage.

In this section, we shall develop a PA scheme for the formation of ultracold Be_2^+ molecular ions in the B $^2\Sigma_g^+$ state. In the previous chapter, we have described the calculation of potential curves for the X $^2\Sigma_u^+$ and B $^2\Sigma_g^+$ states of Be_2^+ and shown the existence of a long-range well in the B $^2\Sigma_g^+$ state, which supports long lived (∼ms) vibrational levels. From the experimental viewpoint, such long-lived bound levels are extremely attractive. Since the longer-lived the molecules are, the longer is the time for possible manipulations and measurements. It is for this reason that we develop a PA scheme to form cold Be_2^+ molecular ions in the shallow long-range well of the B $^2\Sigma_g^+$ state.

In the previous section, we have calculated low-lying excited states in Be_2^+. We choose the first excited state of $^2\Pi_u$ symmetry, the A $^2\Pi_u$ state, as the intermediate excited state to populate into for the PA scheme. As a first step, the Franck-Condon overlap between two electronic states, defined by

$$FCF = \langle \psi_1 | \psi_2 \rangle \,, \tag{3.2}$$

is calculated to estimate the probability of radiative decay from state 2 to state 1. Once we have confirmed that there is a good probability of radiative decay into the lower B $^2\Sigma_g^+$ state in the vicinity of the long-range well, we do a more elaborate treatment to calculate the PA rate.

In order to have consistency in the *ab initio* calculations of the potential energy curves, we treat the A $^2\Pi_u$ at the same level of theory as the ground X $^2\Sigma_u^+$ and B $^2\Sigma_g^+$ states. The valence energy was calculated using full configuration interaction (FCI) with the aug-cc-pV5Z basis set of Peterson [37, 38]. The core-core and core-valence corrections to the correlation energy were made at the CCSDT/MTsmall level of theory, as done previously for the X $^2\Sigma_u^+$ and B $^2\Sigma_g^+$ states. The calculated potential curve for A $^2\Pi_u$ state is also corrected for the effects of basis set superposition error by the counterpoise method of Boys and Bernardi [26]. Scalar relativistic corrections were estimated to be small and are neglected.

A fully quantum mechanical scattering treatment is used to calculate the PA rate and estimate the total number of molecules formed per second in the rovibrational levels of the B $^2\Sigma_g^+$ state. The methods used for calculation of PA rates was developed previously in our group by a former graduate student Elizabeth Juarros [44] for LiH molecule. We use a very similar methodology here. Some of the numerical code was also developed in collaboration with Subhas Ghosal, a former postdoc of the group.

The photoassociation rate coefficient is defined as,

$$K_{v'} = \langle v_{rel} \sigma_{PA} \rangle \,. \tag{3.3}$$

For a laser $L = (I, \Delta)$, of intensity I and detuning Δ from a bound level (v', J') this becomes [45, 46]

$$K_{v'}(T, L) = \left\langle \frac{\pi v_{rel}}{\kappa^2} \sum_{l=0}^{\infty} (2l+1) |S_{l,v'}(\epsilon, L)|^2 \right\rangle, \tag{3.4}$$

where $\epsilon = \hbar^2\kappa^2/2\mu = \mu v_{rel}^2/2$, μ is the reduced mass, v_{rel} is the relative velocity of the colliding pair of atom and ion and $\mathrm{S}_{l,v'}$ represents the scattering matrix element for producing the state v' from the continuum state ϵ.

For ultracold temperatures, we only consider *s*-wave scattering i.e. only the l=0 term contributes and we can approximate

$$|S_{l=0,v'}|^2 \simeq 2\pi\gamma_s(I, \epsilon, v')\delta(\epsilon - \Delta)\,, \tag{3.5}$$

where $\gamma_s(I, \epsilon, v') = \pi I |D_{v'}(\epsilon)|^2/\epsilon_0 c$. Note that

$$|D_{v'}(\epsilon)|^2 \equiv |\langle v'|D(R)|\epsilon\rangle|^2\,, \tag{3.6}$$

where $D(R)$ is the dipole transition moment between the A $^2\Pi_u$ and B $^2\Sigma_g^+$ states. For an ultracold temperature T, assuming a Maxwellian velocity distribution, the maximum value of $K_{v'}(T, L = I, \Delta)$ becomes [47, 48]

$$K_{v'}^{max} = \frac{4\pi^2}{h}\frac{I}{\epsilon_0}\frac{e^{-1/2}}{Q_T} C_{v'} \sqrt{\frac{k_B T}{2}}\,, \tag{3.7}$$

where c is the speed of light, k_B is the Boltzmann constant and $Q_T = (2\pi\mu k_B T/h^2)^{3/2}$ (μ is the reduced mass). We also assume $\mid D_{v'}(\epsilon) \mid^2 = C_{v'}\sqrt{\epsilon}$ according to Wigner's threshold law [49].

We note that this approximation is not valid when the intensity I becomes large and saturation effects need to be estimated [50]. The limiting value of the photoassociation rate coefficient is given by

$$K^{limit}(T) = \frac{k_B T}{h Q_T} = \frac{h^2}{(2\pi\mu)^{3/2}} \frac{1}{\sqrt{k_B T}} \,. \tag{3.8}$$

The rate of molecules formed per second can be obtained if we multiply $K_{v'}$ given by the above equations by the atomic densities n_{Be} and n_{Be^+}, and the volume V illuminated by the laser beam, giving us $R_{v'} = n_{Be} n_{Be^+} K_{v'} V$.

3.4 PA scheme *via* the A$^2\Pi_u$ state

For the current PA scheme, we have chosen the A $^2\Pi_u$ state as the excited state which would radiatively couple to the lower B $^2\Sigma_g^+$ state. Once a vibrational level in the A $^2\Pi_u$ state is populated, it decays into the ground state by spontaneous emission, or by stimulated emission with another laser. For the case of spontaneous emission, the total rate of formation in the ground B $^2\Sigma_g^+$ state is given by [51, 46]

$$R_{tot} = r_v^{v'} R_{v'} = r_v^{v'} n_{Be} n_{Be^+} K_{v'} V \,, \tag{3.9}$$

where, $r_v^{v'} = A_v^{v'} \tau_{v'}$ is the branching ratio between an excited vibrational level $(v', J' = 1)$ and the ground state $(v, J = 0)$. $A_v^{v'}$ is the Einstein A-coefficient (the width of spontaneous emission) and $\tau_{v'} = 1/\sum_v A_v^{v'}$ is the lifetime of the level $(v', J' = 1)$.

However, the population in excited state can also decay by stimulated emission, with the help of a second laser. In this case, the two-photon stimulated Raman photoassociation process is given by [47]

$$K_{vv'}^{(2)} = K_{v'}^{(1)} \Big(\frac{\Omega_{vv'}}{\Delta}\Big)^2, \tag{3.10}$$

where $K_{v'}^{(1)}$ is the single photon photoassociation rate being by Eq. (3.7), $\Omega_{vv'}$ is the bound-bound Rabi frequency and Δ is the detuning. $\Omega_{vv'}$ can be estimated using $\hbar^2\Omega_{vv'}^2 = (2\pi I_2/c)|D_{vv'}|^2$, where $D_{vv'}$ is the transition matrix element between bound levels v and v'.

The A $^2\Pi_u$ state lies energetically lower than the B $^2\Sigma_g^+$ state (Fig. 3.3) which means the lowest rovibrational levels of the A $^2\Pi_u$ state would be extremely long lived, since spontaneous emission to the lowest ground X $^2\Sigma_u^+$ state is dipole forbidden.

In the present PA scheme (Fig. 3.3), the red band of the excited levels are not accessible, thus one has to go to a much higher, possibly a Rydberg state, to probe the deeply bound levels of the B $^2\Sigma_g^+$ state which in turn can radiatively decay into A $^2\Pi_u$. The A $^2\Pi_u$ state supports 60 bound levels, however there is good Franck-Condon overlaps with the B $^2\Sigma_g^+$ outer well (v = 8 - 15, $J' = 0$) only for the few uppermost rovibrational levels (v' = 50 - 59, $J = 1$). The lifetimes of bound levels in the A $^2\Pi_u$ state are calculated by the same procedure used previously for the B $^2\Sigma_g^+$ state [52].

3.5 Transition moment and Long-range expansion coefficients

The transition moment between A $^2\Pi_u$ and B $^2\Sigma_g^+$ of Be_2^+ are obtained from multi-reference configuration interaction (MRCI) calculations using a 16 orbital complete

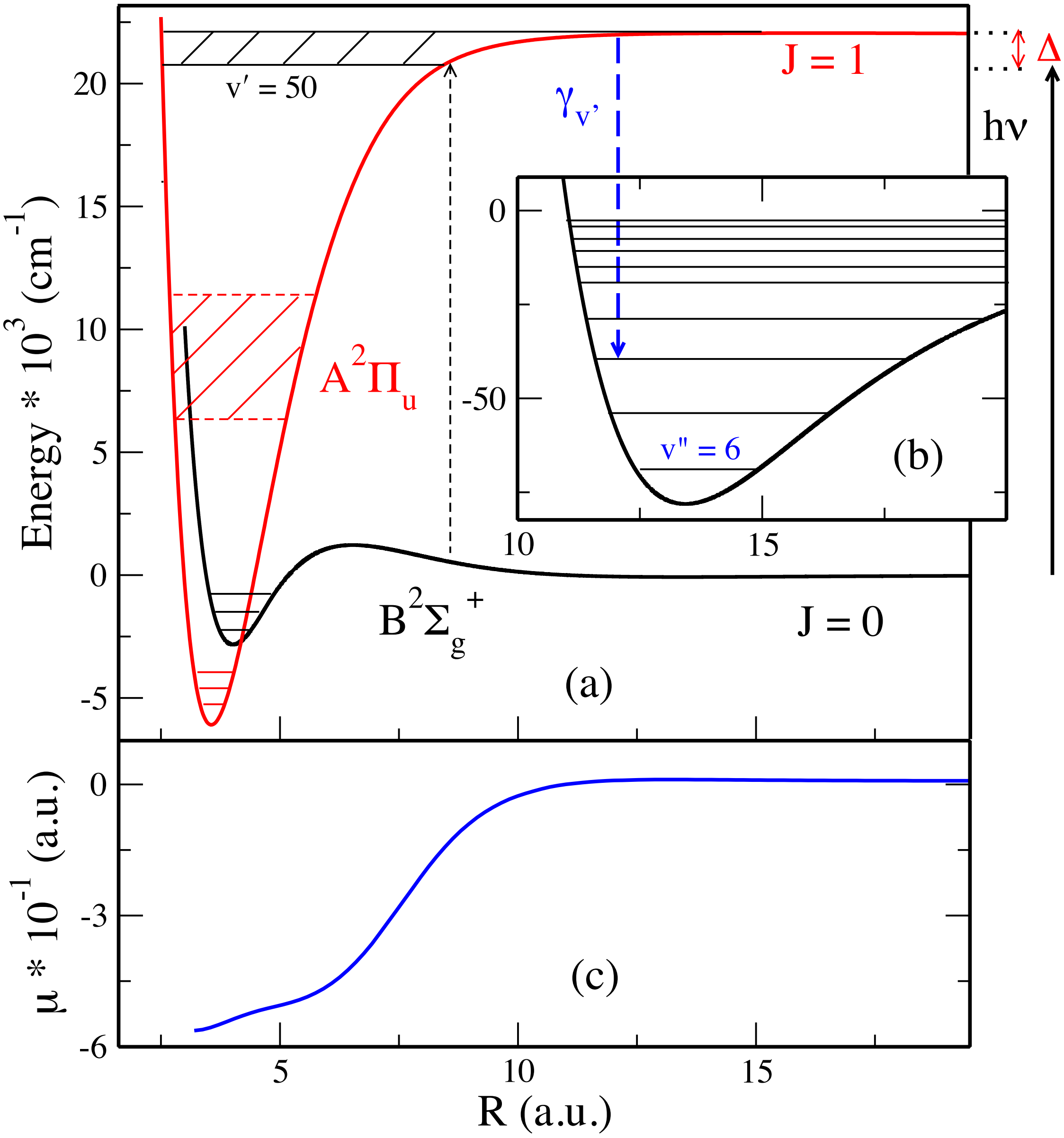

Figure 3.3. (a) PA scheme to populate the highest bound levels in A $^2\Pi_u$ state (black band), which decays by spontaneous emission to outer well of B $^2\Sigma_g^+$. (b) A magnification of the outer well of B $^2\Sigma_g^+$ state with bound vibrational levels. (c) The calculated electronic dipole transition moment between the A $^2\Pi_u$ and B $^2\Sigma_g^+$ states of Be_2^+.

active space self consistent field (CASSCF) reference. Fig. 3.3(c) shows the computed electronic dipole transition moment between the A $^2\Pi_u$ and the B $^2\Sigma_g^+$ ground states of Be_2^+.

Starting with our *ab initio* results, we compute the Be_2^+ PA formation rate. The calculated potential curve for the B $^2\Sigma_g^+$ state was smoothly joined to the long-range form $-C_4/R^4 - C_6/R^6 - C_8/R^8$ [52]. The A $^2\Pi_u$ state was smoothly continued to $-C_3/R^3 - C_4/R^4 - C_6/R^6$. Note that the expansion coefficients are different for the two states since they come from different atom/ion asymptotes, $\mathrm{Be}(^1\mathrm{S}_g)$ + $\mathrm{Be}^+(^2\mathrm{S}_g)$ and $\mathrm{Be}(^3\mathrm{P}_u)$ + $\mathrm{Be}^+(^2\mathrm{S}_g)$ for the B $^2\Sigma_g^+$ and A $^2\Pi_u$ states, respectively.

Note that $C_3 = Q \times q$, where Q is the quadrupole moment of the Be atom in the ^3P state and q is the charge of the Be^+ ion (+1). $C_4 = \alpha_d/2$, where α_d is the dipole polarizability of the beryllium atom in the respective ground/excited state. We report the long-range expansion for all the doublets going to the same asymptote as that of A $^2\Pi_u$ state. Note that C_3 for the A $^2\Pi_u$ and 1 $^2\Pi_g$ state has opposite sign and magnitude (half) from the 2 $^2\Sigma_{g,u}^+$ states (see Table 3.2). This behavior has been previously studied for alkali dimers by Marinescu and Dalgarno [53]. The *ab initio* calculations of polarizabilities and expansion coefficients agree well with semi-emprical calculations, provided by our collaborator Jim Mitroy in a private communication. The methodology for computing the dispersion coefficients is described below.

The approach used to generate the dispersion coefficients is based on the work of Dalgarno who did many of the early calculations utilizing oscillator strength sum rules [54, 55]. In the case of states with non-zero angular momentum, the sums over oscillator strengths are rewritten in terms of sums over the reduced matrix elements

Table 3.2. The static atomic dipole polarizability (α_d), static quadrupole polarizability (α_q), quadrupole moment (Q) and dispersion coefficients for low lying doublets of Be_2^+. All values are in atomic units (a.u.).

Molecular State	α_d	α_q	Q	C_3 $(= Q \times q)$	C_4 $(=\alpha_d/2)$	C_6'	C_8
X $^2\Sigma_u^+$, B $^2\Sigma_g^+$ [52]	38.12	300.01	0.00	0.00	19.06	120.20	—
Semi-empirical	37.73	—	—	—	18.86	120.35	3876.34
A $^2\Pi_u$, 1 $^2\Pi_g$	39.04	275.01	−2.27	−2.27	19.52	123.29	—
2 $^2\Sigma_u^+$, 2 $^2\Sigma_g^+$	39.04	275.01	4.54	4.54	19.52	123.29	—
Semi-empirical	39.04	—	4.54	4.54	19.52	127.50	—

of the electric multipole operators [56, 57]. The underlying structure models used to describe the Be^+ and Be ground and excited states employ a frozen core based on a Hartree-Fock wave function. A semi-empirical core polarization potential is then added to the Hamiltonian. The effective Hamiltonian is then diagonalized in a very large basis of one-electron or two-electron states constructed using Laguerre Type Orbitals [58]. Specific details of the structure models for Be^+ [59] and Be [60] have been published previously. Contributions arising from core excitations are explicitly included in the evaluation of dispersion coefficients and polarizabilities [58, 56]. Calculations using this approach reproduce the close exact Hylleraas calculations of the polarizabilities of the Be^+ $2s$ and $2p$ states to better than 0.01 a_0^3 [59]. Similarly, the present model calculation of the Be ground state dipole polarizability reproduces the best ab-initio calculation to better than 0.1% [60].

3.6 Photoassociation Rates

We report our computed values for $K_{v'}^{max}$ going into the excited rovibrational levels (v', J'=1) in Table 3.3 for certain levels with maximum Franck-Condon overlap with the ground state levels (v, J=0). We choose a laser intensity $I = 1000$ W/cm^2 and temperature $T = 1$ mK for all our calculations. We choose these experimental parameters so that the PA rate coefficient would be safely below K^{limit}. The limiting value for PA rate with these parameters is $K^{limit} = 3.66 \times 10^{-10}$ cm^3/s. We find the largest rate coefficient to be 3.56×10^{-15} cm^3/s for $v' = 59$. For lower vibrational levels $K_{v'}^{max}$ steadily decreases, which can be explained by the poor overlap of the continuum wave function of the ground B $^2\Sigma_g^+$ state with the excited bound level wave functions.

Table 3.3. Photoassociation rates $K^{(1)}_{vv'}$, $K^{(2)}_{vv'}$ with corresponding lifetimes ($\tau_{v'}$) and branching ratio ($r_v^{v'}$) for bound levels v' and v with best Franck-Condon overlaps. Parameters used are $I_1 = I_2 = 1000$ W/cm^2, $T = 1$ mK, $\Delta = 500$ MHz. Powers of ten are indicated in square brackets.

Levels ($v \leftarrow v'$)	$C_{v'}$(a.u.)	$K^{(1)}_{vv'}$(cm^3/s)	$\tau_{v'}$(s)	$r_v^{v'}$	$D_{vv'}$(a.u.)	$K^{(2)}_{vv'}$(cm^3/s)
06 ← 54	2.26[+1]	1.75[−17]	6.27[−11]	< 1%	9.64[−8]	2.83[−20]
07 ← 56	3.07[+2]	2.38[−16]	1.57[−07]	< 1%	3.42[−9]	4.85[−22]
08 ← 50	4.92[−3]	9.14[−45]	2.46[−15]	99%	1.36[−5]	1.22[−19]
09 ← 57	1.18[+2]	9.14[−17]	2.08[−04]	47%	4.76[−5]	3.61[−14]
10 ← 59	4.59[+3]	3.56[−15]	2.06[−05]	23%	1.91[−3]	2.26[−09]
11 ← 58	1.10[+3]	8.53[−16]	1.85[−05]	14%	5.65[−4]	4.74[−11]
12 ← 51	4.58[−2]	6.14[−44]	2.63[−15]	12%	1.15[−6]	8.18[−21]
13 ← 52	2.26[+1]	3.82[−21]	3.61[−14]	12%	3.41[−6]	3.54[−17]
14 ← 53	3.30[+0]	1.83[−30]	1.90[−12]	10%	9.31[−6]	3.93[−17]
15 ← 55	1.13[+2]	8.81[−17]	2.49[−09]	9%	5.03[−5]	3.86[−14]

Larger rates can be obtained by saturating the transition to K^{limit}. One can also use another laser to obtain a two-photon assisted PA rate (see Eq. (3.10)). In that case one ensures that the molecules formed in the excited level can be transferred to the ground state with $\sim$ 100% efficiency. Also since the formation rate is large for the uppermost vibrational level v', the laser wavelength necessary ($\sim$ 455 nm) for this process would be close to the $2s$ - $3p$ atomic transition of Be, which can be easily realized experimentally.

3.7 Concluding Remarks

We note that by using photoassociation, a large number of Be_2^+ molecules could be formed in the long-range well of the B $^2\Sigma_g^+$ state. This means that PA can be used as an experimental probe to study the long-range properties of the ground B $^2\Sigma_g^+$ state in Be_2^+ dimer. Owing to the long lifetimes of the molecules realized in the long-range well, there can be many applications in the study of resonant charge transfer and quantum information storage.

In order to obtain the PA rates, we first calculated the excited potential energy curves of the Be_2^+ dimer using similar *ab initio* techniques that we developed in Chapter 2. We also calculated the electronic dipole transition moments coupling the A $^2\Pi_u$ and the B $^2\Sigma_g^+$ state. For the proposed PA scheme, we got a single photon rate of $\sim 10^{-15}$ cm^3/s for the highest vibrational level in the A $^2\Pi_u$ state. This rate got significantly improved once we used a two-photon scheme to obtain the final PA rate of $\sim 10^{-9}$ cm^3/s. With the tremendous advancement in the field of lasers, using a two-photon PA scheme is easily achievable experimentally. Thus, the theoretical results look extremely hopeful in order to produce cold Be_2^+ molecular ions.

Chapter 4

Other homonuclear alkaline-earth systems — Ca_2^+, Sr_2^+ and Mg_2^+

4.1 Motivations

In the previous chapters, we have developed the *ab initio* methodology to calculate ground and excited states in Be_2^+ dimer. We want to extend our study to other homonuclear species of the alkaline earth family – Mg_2^+, Ca_2^+, and Sr_2^+ (Ba_2^+ is omitted since it requires large relativistic corrections). The valence electronic structures are similar for all alkaline-earth molecular ions,

Be_2^+: $(2s)^2$
Mg_2^+: $(3s)^2$
Ca_2^+: $(4s)^2$
Sr_2^+: $(5s)^2$
Ba_2^+: $(6s)^2$.

In this chapter, we obtain accurate *ab initio* calculations for the X $^2\Sigma_u^+$, B $^2\Sigma_g^+$, and A $^2\Pi_u$ states of Mg_2^+, Ca_2^+, and Sr_2^+ molecular ions. Due to recent interests in experiments on Ca_2^+ and Sr_2^+ [61, 8] we developed a computational scheme keeping the valence electronic structure of Ca and Sr in mind. We later extend our calculations to describe Mg_2^+, which turns out to be the exception in this series, i.e. without a "double well" in the B $^2\Sigma_g^+$ state. Although the valence electronic structure is very similar among Be, Mg, Ca, and Sr, no unique computational model could describe the intricacies of the various ionic dimers accurately. Hence, the different species are described in separate sections, and a comparative study between them is made at the end.

4.2 Ca_2^+ molecular ion

In this section, we describe the *ab initio* methods used in our calculations for the Ca_2^+ dimer, and follow with a discussion of the results, which include the potential curves of the X $^2\Sigma_u^+$, B $^2\Sigma_g^+$, and A $^2\Pi_u$ states and their spectroscopic constants. We also calculate electronic dipole transition moments for the X $^2\Sigma_u^+ \leftrightarrow$ B $^2\Sigma_g^+$ and the B $^2\Sigma_g^+ \leftrightarrow$ A $^2\Pi_u$ transitions. Bound vibrational levels are computed for all the states along with Franck-Condon overlaps and radiative lifetimes for the most abundant calcium isotope (^{40}Ca 96.94%). We also provide an analysis of long-range behavior, calculation of static atomic dipole and quadrupole polarizabilities, and determination of the Van der Waals dispersion coefficient C_6'.

4.2.1 Computational Methods

We can express the total energy of Ca_2^+ at any interatomic separation R as

$$E_{total} = E_{valence} + \Delta E_{core-valence} + \Delta E_{scalar-relativistic}\,. \tag{4.1}$$

For the ground X $^2\Sigma_u^+$ and B $^2\Sigma_g^+$ states, the valence contribution to the total energy is calculated by a multi-reference configuration interaction (MRCI) method using a 18 orbital complete active space (CAS) wavefunction as a reference. The presence of near degeneracies in the constituent atoms can lead to a rich structure in the resulting interaction potentials. The active space was chosen to include molecular counterparts of nearly degenerate $4s$, $4p$ and $3d$ orbitals of Ca. The state-averaged CAS includes all doublet states correlated to Ca$^+$(^{2}D) + Ca(^{1}S) and Ca$^+$(^{2}S) + Ca(^{1}S) asymptotes with equal weights. We have used the augmented correlation consistent polarized valence quintuple zeta (aug-cc-pV5Z) basis set of Peterson [37, 38]. In order to assess the quality of MRCI, we do a comparison with a full CI calculation with aug-cc-pVTZ basis, and find out that the difference in total energy at the equilibrium separation of 7.3 bohrs for the X $^2\Sigma_u^+$ state of Ca$_2^+$ is 4.5 microhartrees. At large separation (1000 bohrs), this difference further reduces to 1.5 microhartrees.

The second term in Eq. (4.1), the correction from the core-valence contribution is estimated by

$$\Delta E_{core-valence} = [E_{RIV} - E_{Val}]_R - [E_{RIV} - E_{Val}]_{R_\infty} \,. \tag{4.2}$$

The core-valence correction $\Delta E_{core-valence}$ is the difference of energies from a valence only (Ar core) and a restricted inner valence (RIV, Ne core) CCSDT calculation. For this purpose we have used the correlation-consistent polarized weighted core-valence triple zeta (cc-pwCVTZ) basis set of Koput and Peterson [37]. To assess the convergence with basis set of the calculated core-valence contribution, we performed single point calculations at the equilibrium bond separation for the ground state with a larger basis set (cc-pwCVQZ). The effect of increasing the basis set from TZ to QZ changed the core-valence energy by ~ 8 cm^{-1} at the r_e of the B $^2\Sigma_g^+$ state. These results indicate that the core-valence contribution to the total energy is adequately converged with the TZ basis sets.

The last correction term $\Delta E_{scalar-relativistic}$ is the contribution from relativistic effects, which for a heavy atom like Ca is significant. This can be expressed as

$$\Delta E_{scalar-relativistic} = [E_{rel} - E_{non-rel}]_R - [E_{rel} - E_{non-rel}]_{R_\infty} . \tag{4.3}$$

We have used the Douglas-Kroll version of the cc-pwCVTZ basis set from Kirk Peterson (cc-pwCVTZ-DK), and performed CCSDT calculations to estimate this correction. The magnitude of scalar relativistic correction at the equilibrium bond distance for the B $^2\Sigma_g^+$ state of the Ca_2^+ is $\sim$ 180 cm^{-1}. For Ca_2^+, the valence electron space contains only 3 electrons, thus the valence CCSDT is equivalent to full CI.

The calculation of the A$^2\Pi_u$ state, correlating to the Ca$^+$ $3d$ atomic level, is complicated by the near degeneracy with the Ca $4s4p$ atomic level. The second excited $^2\Pi_u$ state comes from an atomic asymptote of Ca $4s4p$ and Ca$^+$ $4s$, which lies $\sim$ 1500 cm^{-1} above the A$^2\Pi_u$ asymptote. We find, however, that valence CAS+MRCI calculations incorrectly predict the Ca $4s4p$ and Ca$^+$ $4s$ asymptote to lie below the Ca $4s^2$ and Ca$^+$ $3d$ asymptote. The correct ordering of the atomic energy levels is obtained when core-valence correlation including double excitations of the inner valence electrons are included in the correlation treatment using the cc-pwCVQZ (or better) basis set.

We expect that a balanced description of valence and core-valence interactions in the A$^2\Pi_u$ state would be obtained from a CAS(19,26)+MRCI calculation that includes molecular orbitals arising from the atomic $3s$, $3p$, $3d$, $4s$ and $4p$ orbitals. This is a much more demanding calculation than those required for the X $^2\Sigma_u^+$ and B $^2\Sigma_g^+$ states that correlate to ground states atoms. It was found that a smaller CAS(19,21)+MRCI+Q/cc-pwCVQZ (MRCI plus Davidson correction) calculation correlating the $3s3p$ inner valence electrons with a $4s3d + 4p_x$ valence reference was sufficient to obtain the correct ordering of the first and second $^2\Pi_u$ molecular states. Extending this calculation to include the entire $4p$ reference space using the cc-pwCV5Z was attempted but was too computationally demanding for our available resources.

An alternative approach to the multi-reference all electron calculation is to replace the argon core of the Ca atoms with an effective-core potential (ECP) where the effects of core-valence correlation are included using a core polarization potential (CPP) [62].

The ECP and CPP used for Ca_2^+ are listed below. Since most *ab initio* calculations were employed using `MOLPRO`, we list the ECP and CPP in the `MOLPRO` format,

```
basis={
!
! basis set used with Ca ECP
!
s,Ca,3.915549,1.717346,0.753222,0.330361,
0.144895,0.063550,0.027873,0.012225,0.005362
p,Ca,1.791540,0.730947,0.298226,0.121676,
0.049644,0.020255,0.008264
d,Ca,2.722,1.296,0.648,0.216,0.072,0.024
f,Ca,0.264,0.155,0.091
g,Ca,0.166635

ECP,Ca,18,3,0;
1; 2,1.000000,0.000000;
1; 2,0.898000,12.466000;
1; 2,0.548000,5.146000;
1; 2,1.119000,-7.709000;

! CPP Input - should be put before
! the RHF card

!cpp,init,1;
!ca,1,3.06,,,0.43;
}
```

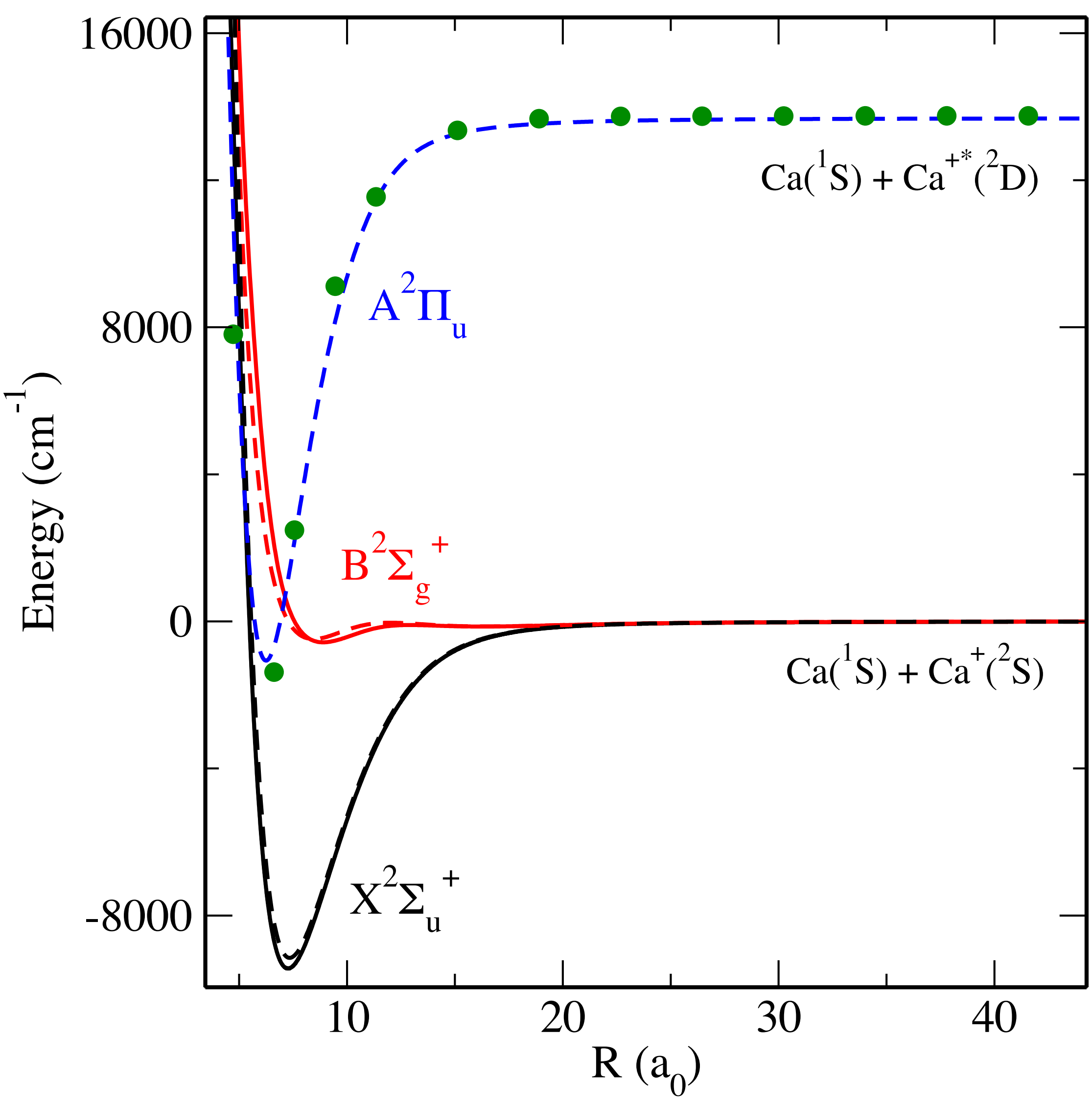

Figure 4.1. *Ab initio* X $^2\Sigma_u^+$ (in black), B $^2\Sigma_g^+$ (in red) and A $^2\Pi_u$ (in blue) states of Ca_2^+. Dashed lines show calculation with a pseudopotential, while solid lines show the results of an all electron correlated calculation. For the A $^2\Pi_u$ state, results of all electron MRCI calculations are shown in green ●. Note that a_0 is the Bohr radius (atomic unit of length).

This method was used with great success by Czuchaj *et al* for Ca_2 ground and excited states [63]. We have performed comparisons between the all electron calculations for the first two $^2\Sigma$ states as described above and the valence $4s4p3d$ space MRCI using the ECP+CPP and basis set of Czuchaj *et al* [63]. The agreement was found to be satisfactory for the case of the lowest Σ states as seen in Fig. 4.1. Additionally we have compared the $\mathrm{A}^2\Pi_u$ state calculated using the same ECP+CPP method to the core-valence MRCI+Q/cc-pwCVQZ calculation using the $3s3p4s3d + 4p_x$ space discussed above. These two calculations agree very well, as demonstrated by Fig. 4.1. Because of the good agreement with the all electron calculations and the computational limitations in performing multi-reference core-valence correlation calculation, we have used the ECP+CPP method to calculate the $\mathrm{A}^2\Pi_u$ state. We note in passing that the use of the CPP is essential; without it one does not obtain the correct ordering of the excited atomic asymptotes. All the potential curves are also corrected for basis-set superposition error (BSSE) using the standard counterpoise technique of Boys and Bernardi [26]. The BSSE was negligible ($\sim 2 - 4\ \mathrm{cm}^{-1}$) at the potential minima for the different curves.

The MRCI valence calculations were done using the `MOLPRO` electronic structure program [27]. The core-valence CCSDT calculations were carried out using `CFOUR` (coupled-cluster techniques for computational chemistry) program [64]. A sample input file for calculation of core-valence corrections using the `CFOUR` program is provide in Appendix A.4. The `MOLPRO` package has scripting facilities built in to its code, unlike other similar programs like `CFOUR`. Hence, to use such a program to calculate a series of data points, at various internuclear separations, one needs to use third party scripts or programs. Most commonly used coding platforms are in `PERL` and `PYTHON`. We have developed a general `PYTHON` program, which can be used with most quantum chemistry software to generate a series of data points at the desired internuclear separations, for a certain level of theory. Since in this context using the `CFOUR` program was the most efficient for calculating the core-valence corrections, we have provided the `PYTHON` script for use with `CFOUR` program in Appendix A.5. The scalar relativistic corrections were done at the CCSDT level of theory using the `MRCC` (multi-reference coupled cluster) program [29] of M. Kállay. All of the programs were running on a Linux workstation. All calculations employed restricted open-shell (ROHF) reference wavefunctions.

4.2.2 Potential Curves and Spectroscopic Constants

Fig. 4.2 shows the *ab initio* potential curves for the X $^2\Sigma_u^+$ and B $^2\Sigma_g^+$ states of Ca_2^+. The calculated curves are corrected for the effects of basis set superposition error by the counterpoise method of Boys and Bernardi [26]. Fig.4.1 shows the A $^2\Pi_u$ state. We have used a standard Dunham analysis [31] to calculate the spectroscopic constants (Table 4.1). We calculate bound vibrational levels for the X $^2\Sigma_u^+$, B $^2\Sigma_g^+$, and A $^2\Pi_u$ state for the $^{40}Ca_2^+$ dimer.

Unfortunately there are no experimental spectroscopic data for the ground or excited states of the Ca_2^+ dimer. There are, however, some previous theoretical studies of Ca_2 [63, 66] and Ca_2^+ [61, 63, 65], and a comparison to the results for the X $^2\Sigma_u^+$ state is given in Table 4.1.

No spectroscopic constants have been reported for the most recent calculation by Sullivan *et al.* [61]. Another approach for calculating interaction energies in alkaline earth elements, is using symmetry-adapted perturbation theory (SAPT), which has

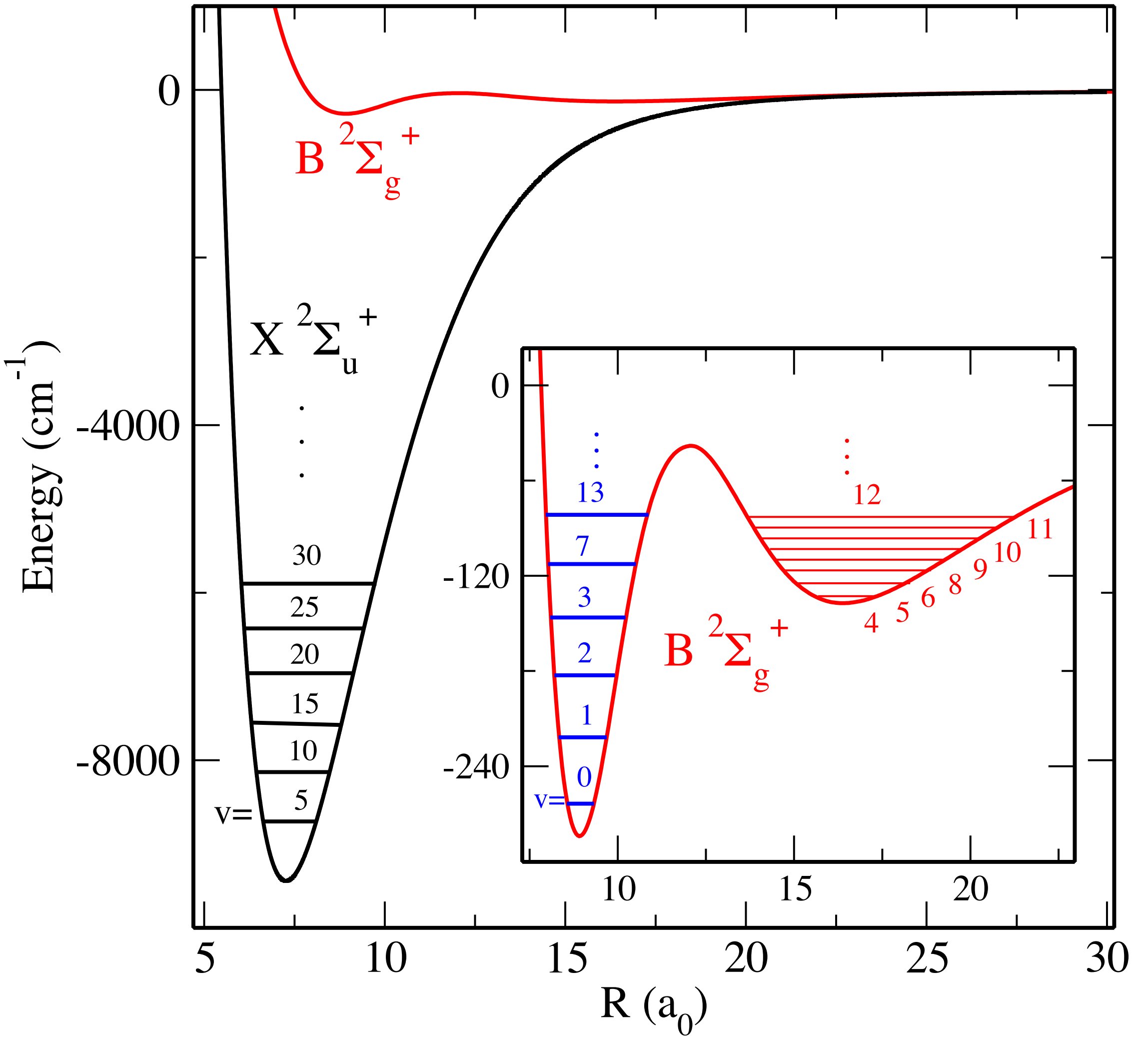

Figure 4.2. Calculated *ab initio* potential curves of Ca_2^+. The inset is a magnification of the double-well nature in the B $^2\Sigma_g^+$ state (in red); lowest vibrational levels in the inner well are shown in blue thick lines and outer well in red thin lines (for ^{40}Ca). X $^2\Sigma_u^+$ state has 168 bound levels and B $^2\Sigma_g^+$ state has 56 bound levels, 6 of which are localized in the inner well.

Table 4.1. Calculated spectroscopic constants of Ca_2^+

State	r_e (Å)	B_e (cm^{-1})	ω_e (cm^{-1})	$\omega_e x_e$ (cm^{-1})	D_e (cm^{-1})
X $^2\Sigma_u^+$	3.844	0.056	127.829	0.071	9440
Previous [63]	3.773		132.300		9817
Previous [65]	3.995	0.053	119.000		8388
B $^2\Sigma_g^+$ (Inner)	4.719	0.037	41.593	0.561	284
B $^2\Sigma_g^+$ (Outer)	8.665	0.011	8.549	3.839	137
A $^2\Pi_u$	3.303	0.077	194.195	0.370	14746

been demonstrated earlier by Patkowski *et al.* [67]. The B $^2\Sigma_g^+$ state has a double well similar to that found in our Be_2^+ calculations [52]. Both of these wells support bound vibrational states. This double-well nature of the B $^2\Sigma_g^+$ state is most likely caused by perturbations from an excited $^2\Sigma_g^+$ state.

We have calculated radiative lifetimes (see Fig. 4.3) for bound vibrational levels in both the inner and outer wells of the B $^2\Sigma_g^+$ state. Since these wells are separated by a large barrier, the wavefunction of the lower vibrational levels can be strongly localized in either wells. The localization of the vibrational wavefunctions can be attributed to the asymmetry of the double well (see Fig. 4.2) and disappears for levels above the barrier.

The behavior of the radiative lifetimes exhibits three distinct regimes, one where the wavefunction is mainly localized in the inner well (in blue), one where it is localized in the outer well (in red), and the last being the region (in green) in which the wavefunction spreads over both wells, resulting in poor Franck-Condon overlap with

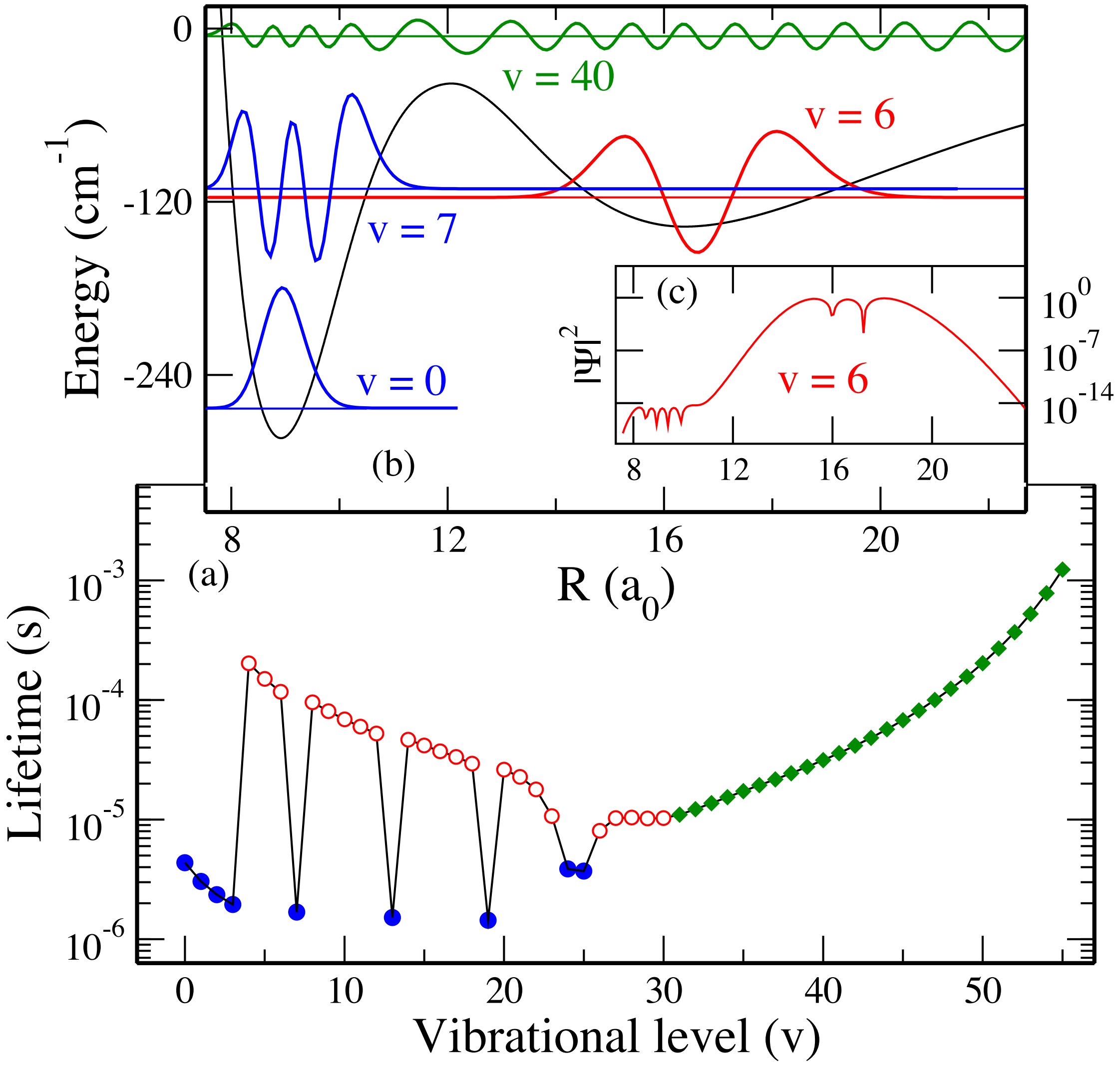

Figure 4.3. (a) Calculated radiative lifetimes of bound levels of $^{40}\text{Ca}_2^+$ in the B $^2\Sigma_g^+$ state, on a log-scale. The shorter lifetimes (blue ●) correspond to bound levels localized in the inner well, the longer lifetimes (red ○) to levels localized in outer well, and the increasingly longer lifetimes (green ◆) to levels spread over both wells. (b) show examples of each cases: v= 0 and 7 in the inner well, v=6 in the outer well, and v=40 in both. (c) depicts $|\psi|^2$ of v=6 on a log-scale; showing that the amplitude in the inner well is extremely small. The reverse is true for v= 7 and so on.

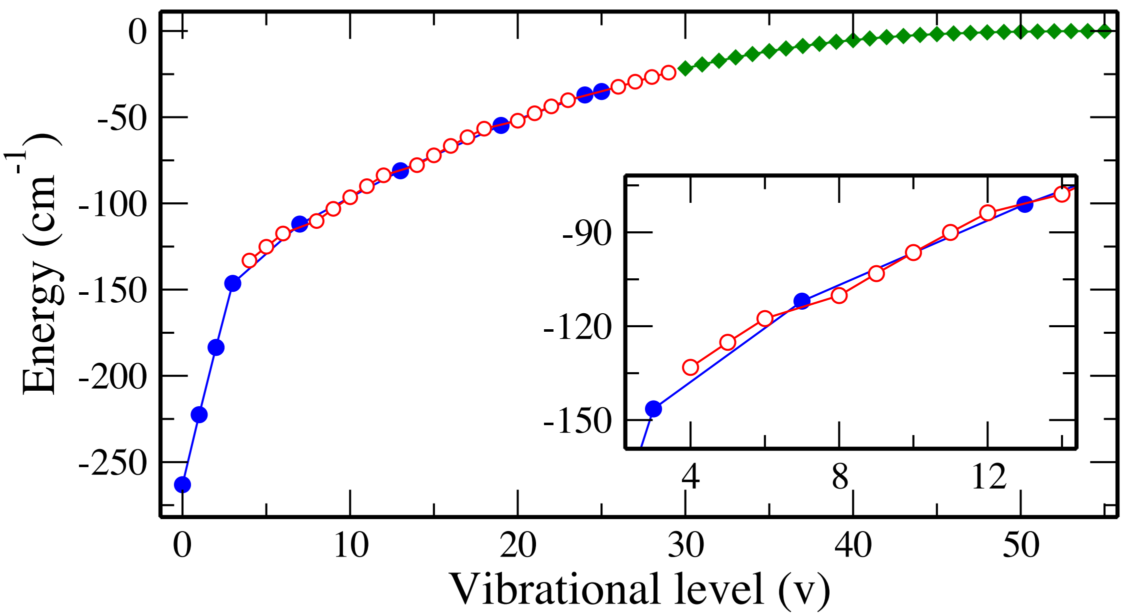

Figure 4.4. Energies of bound levels of B $^2\Sigma_g^+$ state in $^{40}\mathrm{Ca}_2^+$ using the same convention as in Fig.4.3. The inset magnifies the difference in slopes of levels localized in the inner well (shown in blue) from the ones in the outer well (shown in red).

the ground X $^2\Sigma_u^+$ state and hence longer lifetimes. The inset shows the square of the amplitude of wavefunction in v=6, of B $^2\Sigma_g^+$ state in a logarithmic plot as a demonstration that the amplitude is negligible inside the inner well but still finite, preserving the correct number of nodes for that level. Fig.4.4 shows a plot of the energies of all bound vibrational levels in the B $^2\Sigma_g^+$ state of $^{40}\mathrm{Ca}_2^+$. The localization effect of wavefunctions discussed above is also exhibited in this plot; the density of levels in the more extended outer well is larger than in the inner well, leading to different energy slopes. The inset of Fig. 4.4 exemplifies this point.

4.2.3 Electronic dipole transition moments

Electronic dipole-allowed transitions are calculated using similar *ab initio* methodology developed for Be_2^+ in Chapter 2. We calculate two transition moments, one of them couples the ground X $^2\Sigma_u^+$ and B $^2\Sigma_g^+$ states, and the other one couples the

B $^2\Sigma_g^+$ state to the excited A $^2\Pi_u$ state. We use a complete active space self consistent field (CASSCF) wavefunction as a reference for performing multi-reference configuration interaction (MRCI) calculations. The core-valence contribution to the electronic transition moment is found to be negligible and hence omitted in the present calculations. The calculation of the transition moment coupling the B $^2\Sigma_g^+$ state to the excited A $^2\Pi_u$ state was done with the ECP+CPP valence CAS+MRCI method.

The electronic dipole transition moment (in atomic units) is given by

$$\mu_{12}(R) = \langle 2 \,|\, z \,|\, 1 \rangle \,, \tag{4.4}$$

where $|1\rangle$ and $|2\rangle$ are the electronic wave functions corresponding to the pair of states X $^2\Sigma_u^+ \leftrightarrow$ B $^2\Sigma_g^+$ or B $^2\Sigma_g^+ \leftrightarrow$ A $^2\Pi_u$, when the two Ca nuclei are separated by the distance R.

Fig. 4.5(a) shows the electronic transition dipole moment μ_{BA} coupling the B $^2\Sigma_g^+$ and the A $^2\Pi_u$ states. The transition moment goes to zero asymptotically. Fig. 4.5(b) shows μ_{XB} between the B $^2\Sigma_g^+$ and the X $^2\Sigma_u^+$ states of Ca_2^+. The transition moment μ_{XB} asymptotically follows the classical dipole behavior, $\mu_{XB} \sim R/2$ [33, 34] (see Fig. 4.5(b)). We note that although the transition moment grows linearly with R, the probability of spontaneous transition will tend to zero since it is proportional to ν_{XB}^3, which vanishes exponentially as $R \to \infty$.

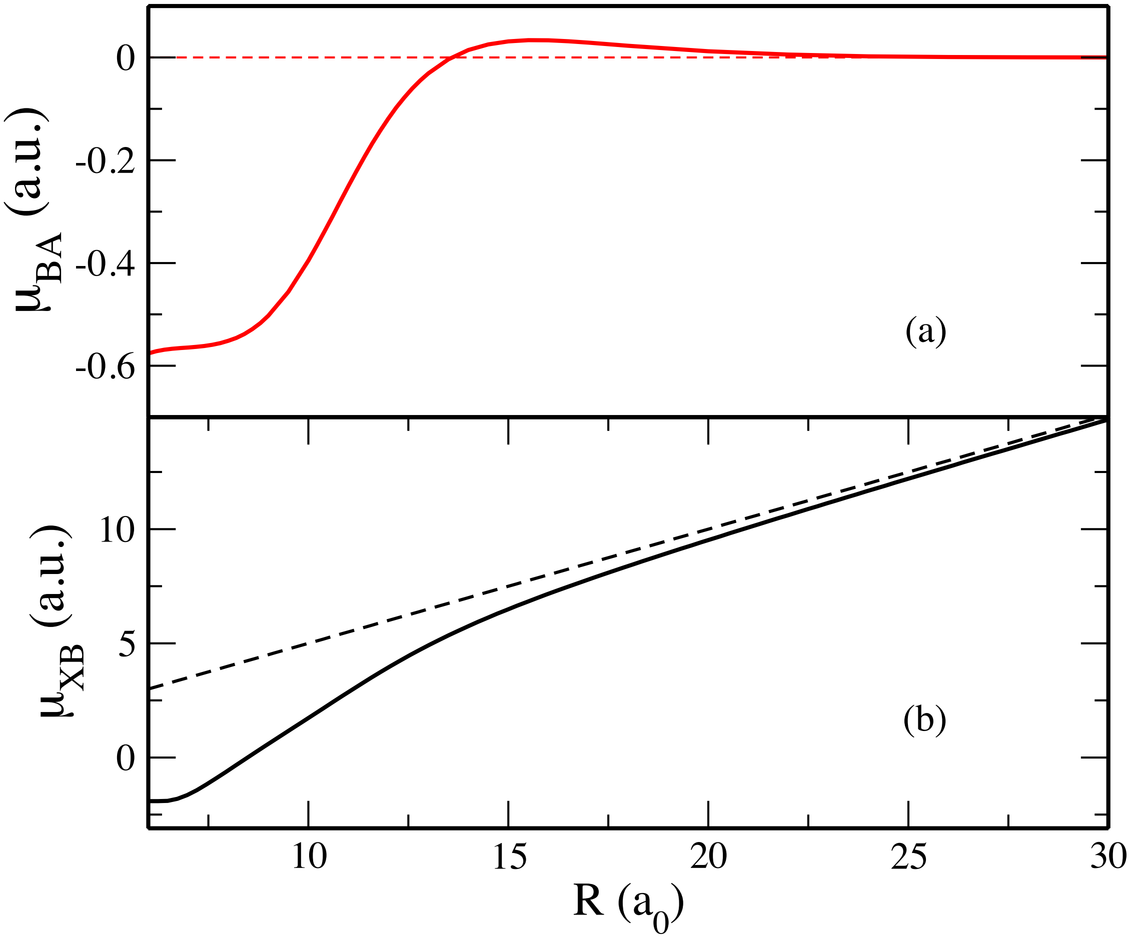

Figure 4.5. Computed electronic dipole transition moment, μ_{BA} coupling the B $^2\Sigma_g^+$ to the A $^2\Pi_u$ state shown in red (a) and μ_{XB} coupling the X $^2\Sigma_u^+$ to the B $^2\Sigma_g^+$ state shown in black (b). The dashed line $R/2$ in (b), corresponds to the classical dipole behavior.

Table 4.2. The static atomic dipole polarizability (α_d), static quadrupole polarizability (α_q) and dispersion coefficient for X $^2\Sigma_u^+$, B $^2\Sigma_g^+$, and A $^2\Pi_u$ states of Ca_2^+. All values are in atomic units. The square brackets indicate powers of ten.

Molecular State	α_d	α_q	C_4 (=$\alpha_d/2$)	Dispersion coefficient (C_6')	C_6 (=$\alpha_q/2+C_6'$)
X $^2\Sigma_u^+$, B $^2\Sigma_g^+$	1.606[2]	3.073[3]	8.032[1]	1.081[3]	2.618[3]
Previous [68]	1.571[2]	3.081[3]			
Previous [36]				1.085[3]	
A $^2\Pi_u$	1.606[2]	3.073[3]	8.032[1]	4.950[2]	2.031[3]

4.2.4 Polarizabilities and long-range coefficients

The long-range analysis for Ca_2^+ was done in a way very similar to that of Be_2^+ described in Chapter 2. For large internuclear separations, the long-range form of the intermolecular potential can be written as

$$V_{LR}(R) = V_\infty - \sum_n \frac{C_n}{R^n}\,, \tag{4.5}$$

which, for the molecular ion Ca_2^+, can be approximated by

$$V_{LR}(R) \sim V_\infty - \frac{C_4}{R^4} - \frac{C_6}{R^6}\,, \tag{4.6}$$

where V_∞ is the energy of the atomic asymptote. C_4=$\alpha_d/2$, α_d is the static dipole polarizability, $C_6 = (\alpha_q/2 + C_6')$, α_q is the quadrupole polarizability, and C_6' the Van der Waals dispersion coefficient. In the expression for long-range energy we have ignored the exchange energy contribution E_{exch} which is very small (discussed in Section 4.7). Also we have truncated the series at powers of R^{-6}, not including contributions from R^{-8} and R^{-10} order coefficients.

We have performed finite-field CCSD(T) calculations with the aug-cc-pV5Z basis set using `MOLPRO` to obtain the values of the static atomic dipole and quadrupole polarizabilities. We obtain $\alpha_d = 160.64$ a.u. and $\alpha_q = 3073.39$ a.u which are both in good agreement with a previous result [68] of 157.1 a.u. and 3081 a.u., respectively. The values of static dipole and quadrupole polarizability do not change for the excited A $^2\Pi_u$ state, since it comes from an atomic asymptote in which the Ca ion is in an excited ^2D state whereas the Ca atom is in ground ^1S state (see Fig.4.1). Using a numerical fit, as described by Banerjee *et al.* [52], we were able to extract the value of the dispersion coefficient C_6' for all the states. The value of dispersion coefficient for ground states are in good agreement with unpublished results of Mitroy [36], which are done by the methods used by Mitroy and Zhang [69, 70] for Ca and Ca$^+$. Table [4.2] lists the values of polarizabilities and dispersion coefficient for X $^2\Sigma_u^+$, B $^2\Sigma_g^+$ and A $^2\Pi_u$ states of the Ca$_2^+$ dimer.

4.3 Sr_2^+ molecular ion

Studies involving Sr atom is now the focal point in the development of precision measurements and atomic clock. There has been many theoretical studies for the Sr atom and Sr_2 neutral dimer [8]. However, very little is known about the Sr_2^+ ionic dimer. With the advancement in cooling and trapping of molecular ions, new experiments have been proposed to study the Sr_2^+ ionic dimer. To better guide experimental efforts, we extend our *ab initio* treatment of alkaline-earth molecular ions and calculate the X $^2\Sigma_u^+$, B $^2\Sigma_g^+$, and A $^2\Pi_u$ states of Sr_2^+. Owing to many similarities with Ca_2^+, I will refer to the previous sections for details of the computation and only present the results of the *ab initio* calculations in the following sub-sections.

4.3.1 Computational Methods

Sr_2^+ is the heaviest of the family of alkaline-earth elements that we have calculated. Owing to its large size and many electrons, developing an *ab initio* method to accurately describe the different electronic interactions was an extremely challenging task. We showed in our calculations of the A $^2\Pi_u$ state in Ca_2^+ that the core electrons approximated by an effective-core potential (ECP) can still give a very accurate results. We hence use a similar ECP+CPP approach to calculate all states of Sr_2^+ molecular ion. Since one does not have to calculate the potential energy in pieces, this method is computational cheap and yet reliable. The ECP and CPP is obtained from Stoll *et al.* [71] and is provided in the `MOLPRO` format below.

```
basis={
!
! basis set used with Sr ECP
!
s,Sr,0.7917400,0.3161780,0.0665650,0.0269900,
1.982593, 0.010944, 0.004437;
p,Sr,0.2258250,0.0956910,0.0420770,0.0180770,
1.257691, 0.532933, 0.007766;
d,Sr,2.722, 1.296, 0.648, 0.216, 0.072, 0.024;
f,Sr,0.264, 0.155, 0.091;
g,Sr,0.166635;

ECP,Sr,36,3,0;
1; 2,1.000000,0.000000;
1; 2,0.796200,15.387000;
1; 2,0.421200,5.077000;
1; 2,0.492700,-2.248000;
!
! CPP Input - should be put before
! the RHF card

!cpp,init,1;
!sr,1,5.51,,,0.315;
}
```

4.3.2 Potential Curves and Spectroscopic Constants

Fig. 4.6 shows the X $^2\Sigma_u^+$, B $^2\Sigma_g^+$ and A $^2\Pi_u$ states of Sr_2^+, computed with the ECP+CPP method described earlier. The potential energy curves are very similar to that of the Ca_2^+ dimer. The B $^2\Sigma_g^+$ state exhibits a similar double well nature as that of Be_2^+ and Ca_2^+, as shown in the inset of Fig. 4.7. Both double wells support bound vibrational levels.

The spectroscopic constants are calculated using the standard Dunham analysis and are shown in Table 4.3. We believe this will be a valuable starting point for the future experiments with Sr_2^+. There has not been any prior experimental or theoretical values to compare our results with.

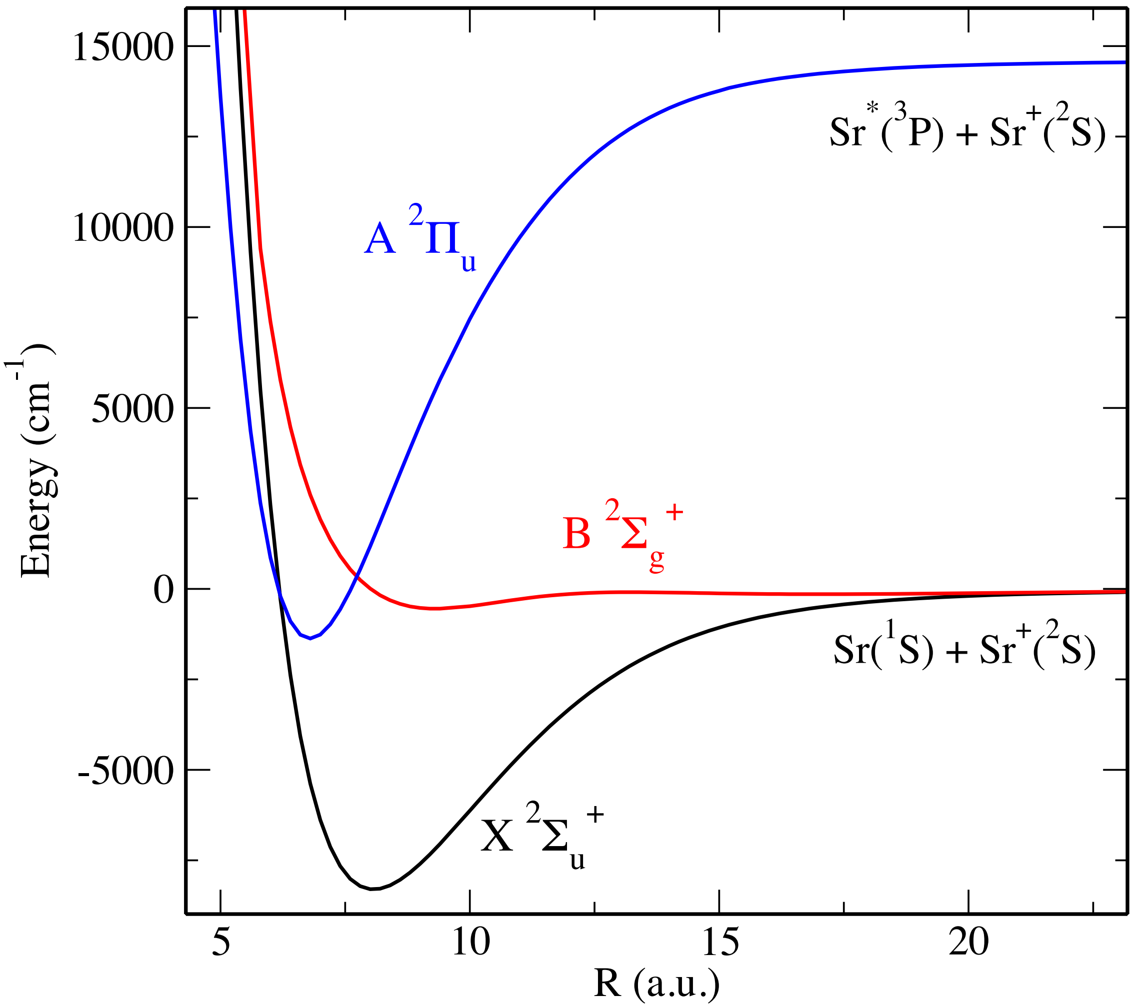

Figure 4.6. *Ab initio* potential energy curves for X $^2\Sigma_u^+$ (in black), B $^2\Sigma_g^+$ (in red) and A $^2\Pi_u$ (in blue) states of Sr_2^+.

Table 4.3. Calculated spectroscopic constants of Sr_2^+

State	r_e (Å)	B_e (cm^{-1})	ω_e (cm^{-1})	$\omega_e x_e$ (cm^{-1})	D_e (cm^{-1})
X$^2\Sigma_u^+$	4.269	0.021	78.634	0.197	8303
B$^2\Sigma_g^+$ (Inner)	4.929	0.015	32.922	0.307	548
B$^2\Sigma_g^+$ (Outer)	8.990	0.004	5.245	1.872	146
A$^2\Pi_u$	3.593	0.029	122.294	0.290	15947

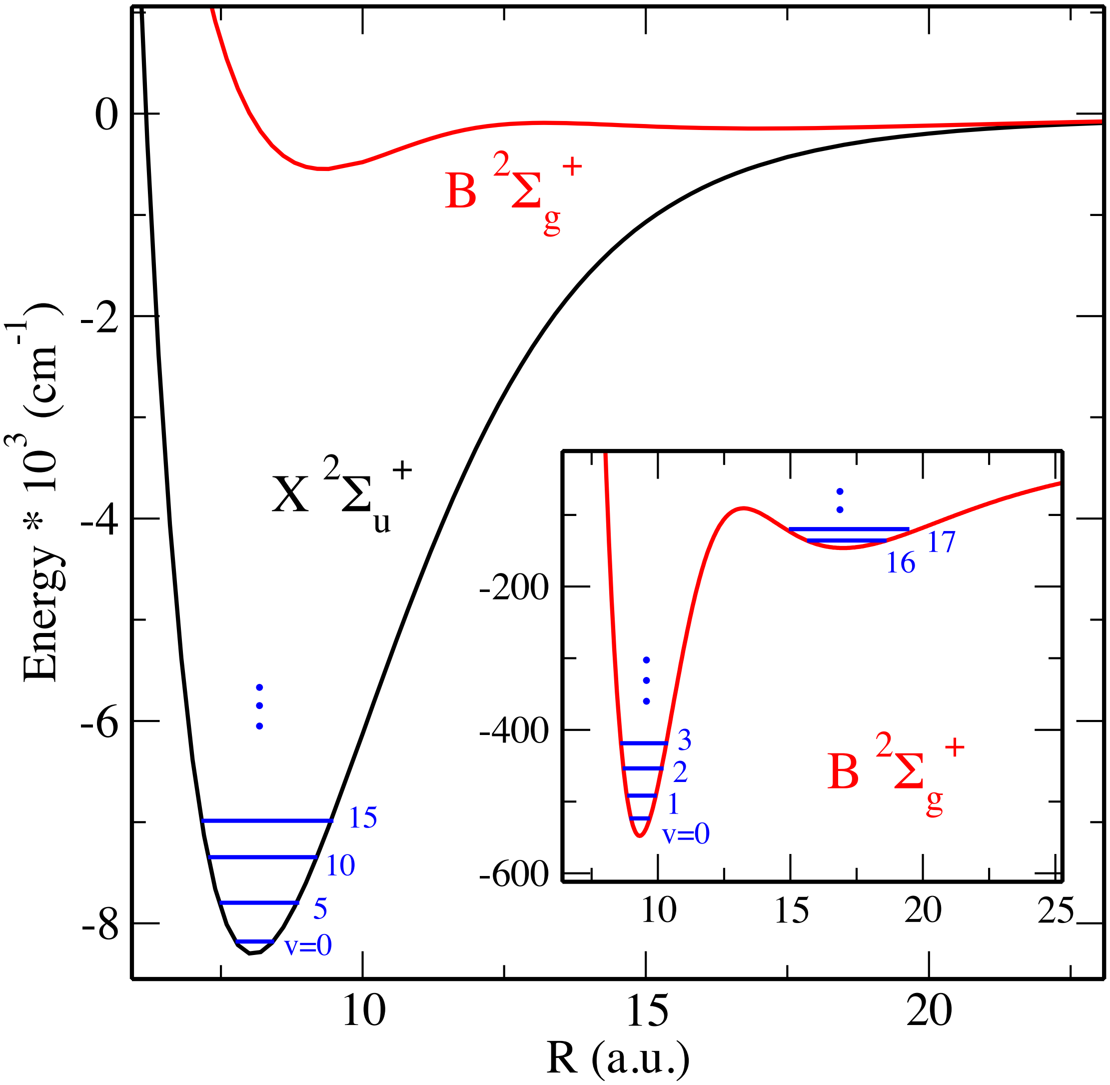

Figure 4.7. Calculated *ab initio* potential curves for ground states of Sr_2^+. The inset is a magnification of the double-well nature in the B $^2\Sigma_g^+$ state (in red). First few bound vibrational levels are shown in each potential minima (in blue), X $^2\Sigma_u^+$ state has 240 bound levels and B $^2\Sigma_g^+$ state has 96 levels, 16 of which are localized in the inner well.

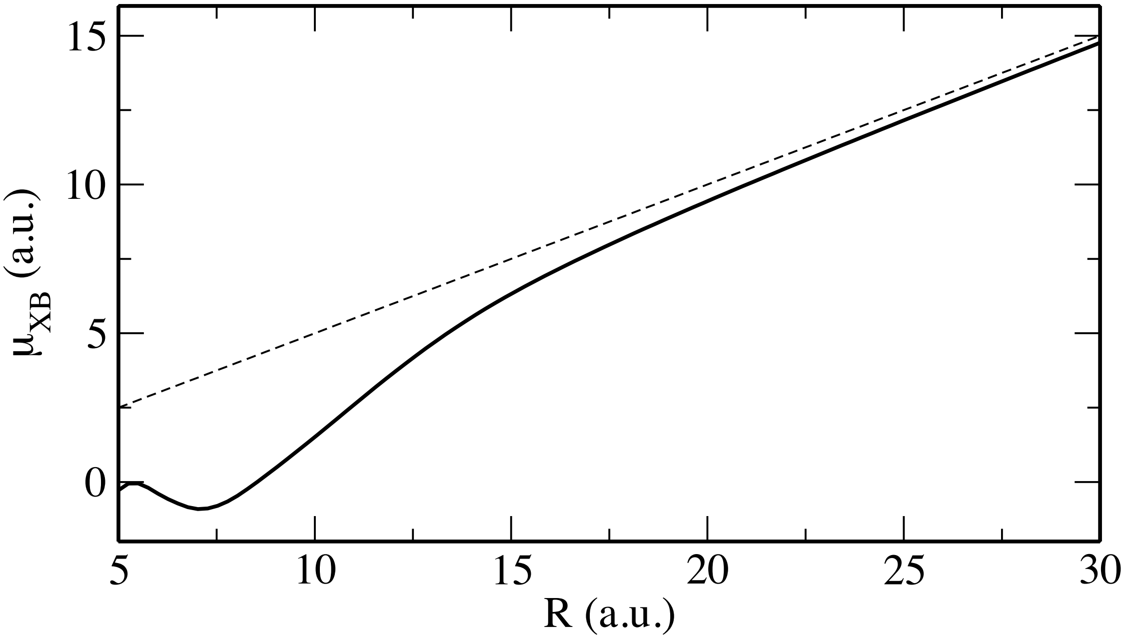

Figure 4.8. Computed electronic dipole transition moment μ_{XB} between the X $^2\Sigma_u^+$ to the B $^2\Sigma_g^+$ state shown in black. The dashed line $R/2$, corresponds to the classical dipole behavior.

4.3.3 Electronic dipole transition moments

Electronic dipole transition moments are calculated using a similar *ab initio* methodology to that developed for Ca_2^+. Fig. 4.8 shows the dipole transition moment coupling the $B^2\Sigma_g^+$ to the $X^2\Sigma_u^+$ state in Sr_2^+. Fig. 4.9 shows the electronic dipole transition moment coupling the $A^2\Pi_u$ state to $B^2\Sigma_g^+$ state. Both the transition moments qualitatively show a very similar pattern to that obtained for Ca_2^+.

4.3.4 Polarizabilities and long-range coefficients

The long-range analysis for Sr_2^+ was done in a very similar way to that of Ca_2^+. For the excited A $^2\Pi_u$ state, we have to consider an additional expansion coefficient C_3 [53] arising from the quadrupole moment of the Sr atom in the excited ^3P state.

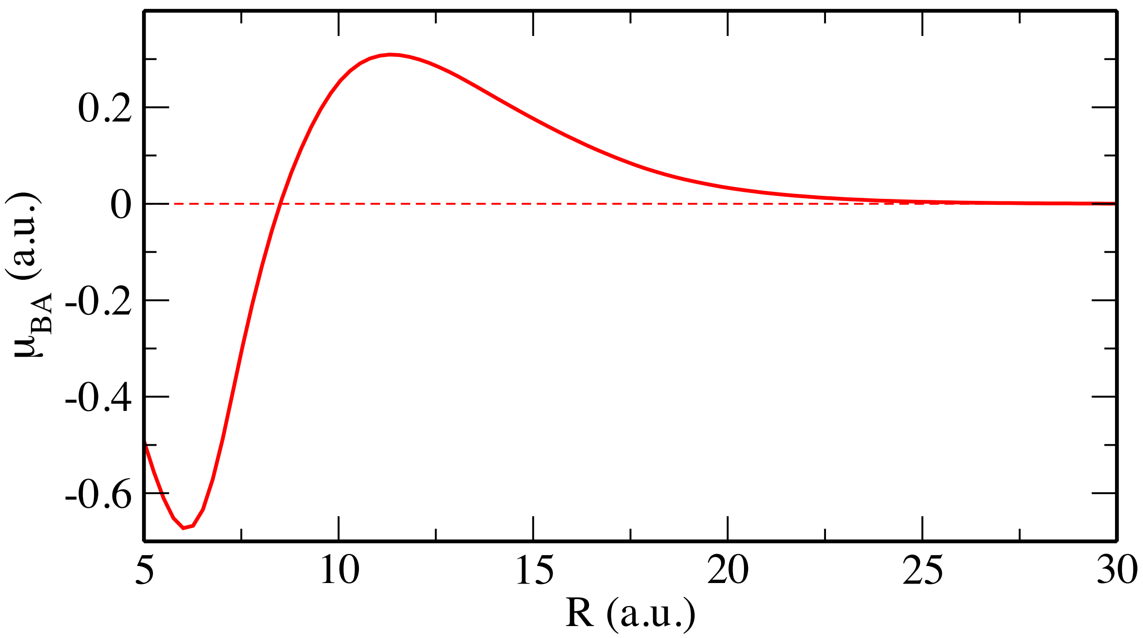

Figure 4.9. Computed electronic dipole transition moment μ_{BA} between the B $^2\Sigma_g^+$ and A $^2\Pi_u$ states.

We have ignored the exchange energy contribution E_{exch} (see Section 4.7 for details) which is very small. Also we have truncated the series at powers of R^{-6}, not including higher order contributions from R^{-8} and R^{-10} coefficients.

For estimating the dipole and quadrupole polarizabilities, we have performed relativistic finite-field calculations in `MOLPRO`. In order to do compute the energies at finite fields, an all electron basis set from Sadlej *et al.* [72] were used. A complete active space (CAS) comprising of 29 orbitals was used as a reference for MRCI calculations. The state-averaged CAS included all doublet states correlated to Sr(^1S) + Sr$^+$(^2S) and Sr(^3P) + Sr$^+$(^2S) asymptotes with equal weights. Table 4.4 lists the values of polarizabilities for the X $^2\Sigma_u^+$, B $^2\Sigma_g^+$, and A $^2\Pi_u$ states of Sr$_2^+$. Our calculated values agree very well with previous theoretical and experimental results.

Table 4.4. The static atomic dipole and static quadrupole polarizabilities for the X $^2\Sigma_u^+$, A $^2\Pi_u$, and B $^2\Sigma_g^+$ states of Sr_2^+. The values in square brackets indicates powers of ten. All values are in atomic units (a.u.).

Molecular State	Dipole polarizability (α_d)	Quadrupole polarizability (α_q)
X $^2\Sigma_u^+$, B $^2\Sigma_g^+$	1.936[2]	4.633[3]
Prev. theory [72]	1.940[2]	—
Prev. theory [68]	1.972[2]	4.630[3]
Prev. theory [73]	2.045[2]	4.641[3]
Prev. expt. [74]	1.860[2] ± 15	—
A $^2\Pi_u$	4.602[2]	6.736[3]
Prev. theory [8]	4.570[2]	—

The effect of core-valence corrections to the dipole and quadrupole polarizabilities have been estimated by Porsev *et al.* [68] to be $\sim$ 5 a.u. and 17 a.u. respectively. Also, since the core is exactly the same for the excited A $^2\Pi_u$ state, we can assume the same core-valence corrections as for the ground X $^2\Sigma_u^+$ and B $^2\Sigma_g^+$ states. Since we do not include the effect of such corrections in our calculation of the polarizabilities, the error in our values for dipole and quadrupole polarizabilities are $\sim$ 2% and 0.3 % respectively. Using a numerical fit, as described by Banerjee *et al.* [52], we were able to extract the value of the dispersion coefficient C_6' for all the states. Table 4.5 lists the values all calculated and derived long-range coefficients for the X $^2\Sigma_u^+$, B $^2\Sigma_g^+$, and A $^2\Pi_u$ states of Sr_2^+.

Table 4.5. The long-range coefficients for the X $^2\Sigma_u^+$, A $^2\Pi_u$, and B $^2\Sigma_g^+$ states of Sr_2^+. The values in square brackets indicates powers of ten. All values are in atomic units (a.u.).

Molecular State	Quadrupole moment (Q)	C_3 ($= Q \times q$)	C_4 ($=\alpha_d/2$)	C_6'	C_6 ($=\alpha_q/2 + C_6'$)
X $^2\Sigma_u^+$, B $^2\Sigma_g^+$	—	—	9.680[1]	3.653[3]	5.970[3]
A $^2\Pi_u$	8.415	8.415	2.301[2]	2.731[3]	6.100[3]

4.4 Mg_2^+ molecular ion

The last species that was studied in this family of alkaline-earth molecular ions was Mg_2^+. Owing to the similar valence electronic structure, most results were found to be similar to other members of the family. One major exception though, is the absence of the double well in the B $^2\Sigma_g^+$ state of Mg_2^+. The B $^2\Sigma_g^+$ state still exhibits a long-range shallow well. We shall discuss more about the double-well nature of B $^2\Sigma_g^+$ state and make a qualitative comparison of the different alkaline-earth molecular ions in the next section.

4.4.1 Computational Methods

Due to the smaller number of electrons in Mg_2^+, we use an all-electron description of the problem similar to the case of Be_2^+. The potential energy curves were calculated as a sum of the valence and the core-valence contributions.

The valence energy was obtained from MRCI calculations using a CAS space comprising of the valence s, p and d orbitals. We have used the augmented 5Z basis sets of Peterson, given below in `MOLPRO` format.

```
basis={
!
! MG   aug-cc-pV5Z
!
sp,Mg,v5z;c;
d,Mg,1.0837,0.4968,0.2278,0.1044;
f,Mg,0.4917,0.2764,0.1554;
g,Mg,0.4427,0.2311;
h,Mg,0.3731;

s,Mg,0.0108;
p,Mg,0.0071;
d,Mg,0.0371;
f,Mg,0.0579;
g,Mg,0.0947;
h,Mg,0.1577;
}
```

The core-valence contribution to the total energy is obtained as a difference between frozen-core and RIV CCSDT calculations done with the cc-pWCVTZ basis sets. The scalar relativistic corrections are estimated to be small and are neglected. The valence calculations were done using `MOLPRO` and the core-valence corrections using the `CFOUR` program.

4.4.2 Potential Curves and Spectroscopic Constants

Fig. 4.10 shows the X $^2\Sigma_u^+$, B $^2\Sigma_g^+$, and A $^2\Pi_u$ states of Mg_2^+ computed with the *ab initio* method described above. Table 4.6 lists the spectroscopic constants r_e, B_e, ω_e, $\omega_e x_e$ and D_e for all the calculated states of Mg_2^+. There has been only one photodissociation experiment to study the X $^2\Sigma_u^+$ state of Mg_2^+ [75], and our calculations agree well with the experimental value of the dissociation energy.

No experiments yet have been reported for the B $^2\Sigma_g^+$ and A $^2\Pi_u$ states. The potential energy curves are qualitatively similar to the other members of the alkaline-

Table 4.6. Calculated spectroscopic constants of Mg_2^+

State	r_e (Å)	B_e (cm^{-1})	ω_e (cm^{-1})	$\omega_e x_e$ (cm^{-1})	D_e (cm^{-1})
X $^2\Sigma_u^+$	3.050	0.149	210.453	0.991	10624
Previous [75]					10200 ± 300
B $^2\Sigma_g^+$	7.897	0.022	11.610	3.825	89
A $^2\Pi_u$	2.625	0.201	325.234	1.361	15890

earth series. The B $^2\Sigma_g^+$ state has a shallow long-range well, which supports 16 bound vibrational levels. This is depicted more clearly in the inset of Fig. 4.11. These levels are long-lived. Table 4.7 shows the radiative lifetimes of the bound levels in the B $^2\Sigma_g^+$ state.

4.4.3 Electronic dipole transition moments

Electronic dipole transition moments are calculated using similar *ab initio* methodology developed for Sr_2^+ and Ca_2^+. Fig. 4.12 shows the dipole transition moment coupling the B $^2\Sigma_g^+$ to the X $^2\Sigma_u^+$ state. Fig. 4.13 shows the electronic dipole transition moment coupling the A $^2\Pi_u$ state to the B $^2\Sigma_g^+$ state. Both transition moments qualitatively show a very similar pattern to that obtained for the other members of the alkaline-earth family of molecular ions.

4.4.4 Polarizabilities and long-range coefficients

The long-range analysis for Mg_2^+ was performed in a similar way to that of Sr_2^+. As was the case with Sr_2^+, the A $^2\Pi_u$ state in Mg_2^+ comes from an excited asymptote,

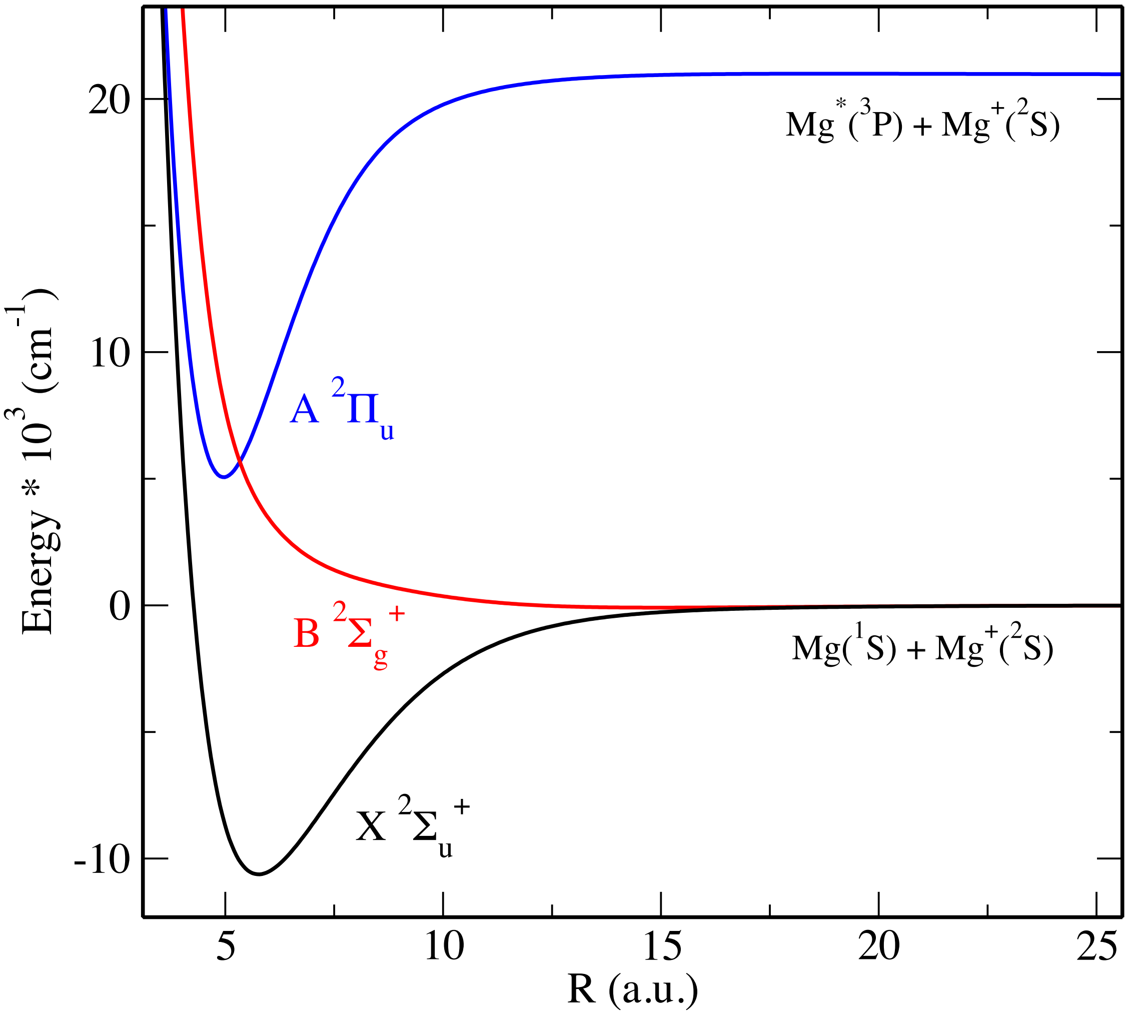

Figure 4.10. Calculated potential energy curves X $^2\Sigma_u^+$ (in black), B $^2\Sigma_g^+$ (in red), and A $^2\Pi_u$ (in blue) for Mg_2^+.

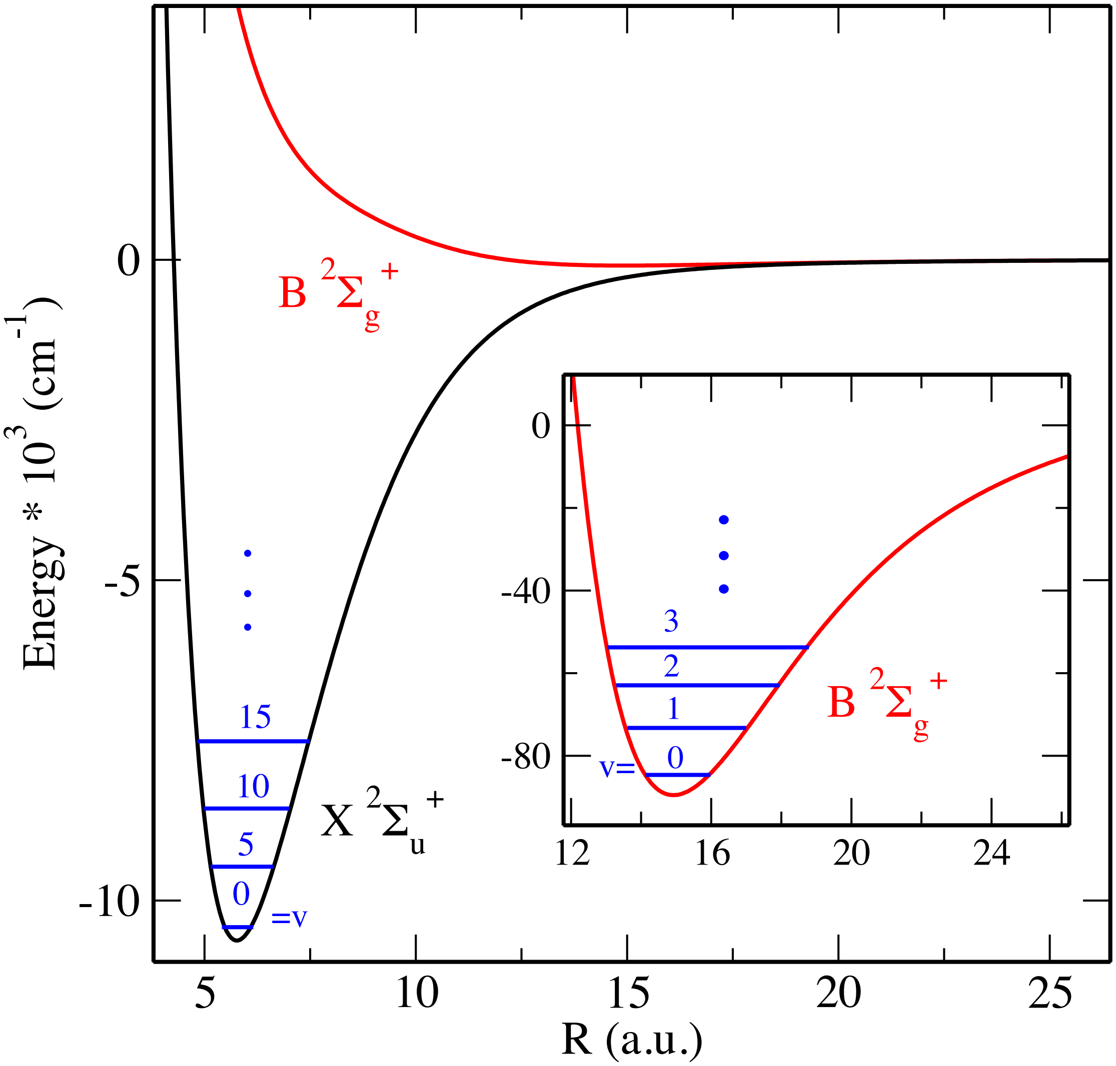

Figure 4.11. Calculated *ab initio* curves for ground states of $^{24}\mathrm{Mg}_2^+$. The inset is a magnification of the shallow long-range well in the B $^2\Sigma_g^+$ state (in red). First few bound vibrational levels are shown in each potential minima (in blue), X $^2\Sigma_u^+$ state has 103 bound levels and B $^2\Sigma_g^+$ state has 16 bound levels.

Table 4.7. Radiative lifetimes of the vibrational levels of the B $^2\Sigma_g^+$ state (in s) for $^{24}\mathrm{Mg}_2^+$.

v'	B $^2\Sigma_g^+ \rightarrow$ X $^2\Sigma_u^+$
0	1.06×10^{-3}
1	7.26×10^{-4}
2	5.71×10^{-4}
3	4.85×10^{-4}
4	4.36×10^{-4}
5	4.08×10^{-4}
6	3.94×10^{-4}
7	3.92×10^{-4}
8	3.99×10^{-4}
9	4.17×10^{-4}
10	4.45×10^{-4}
11	4.85×10^{-4}
12	5.39×10^{-4}
13	6.13×10^{-4}
14	7.51×10^{-4}
15	1.16×10^{-3}

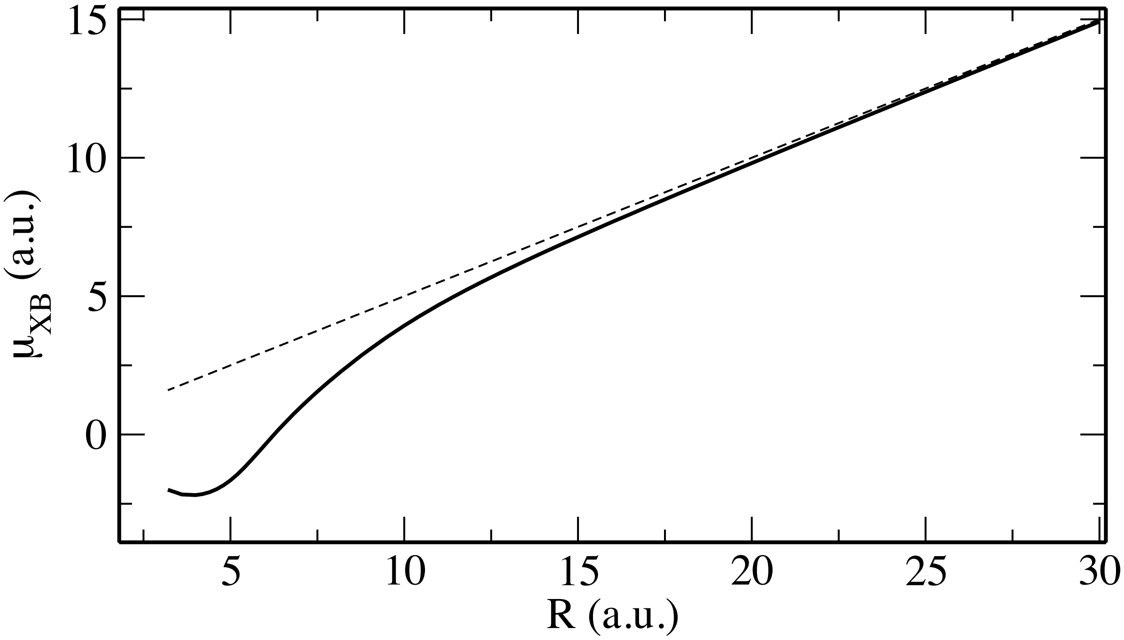

Figure 4.12. Computed electronic dipole transition moment μ_{XB}, coupling the X $^2\Sigma_u^+$ to the B $^2\Sigma_g^+$ state shown for Mg_2^+. The dashed line $R/2$, corresponds to the classical dipole behavior.

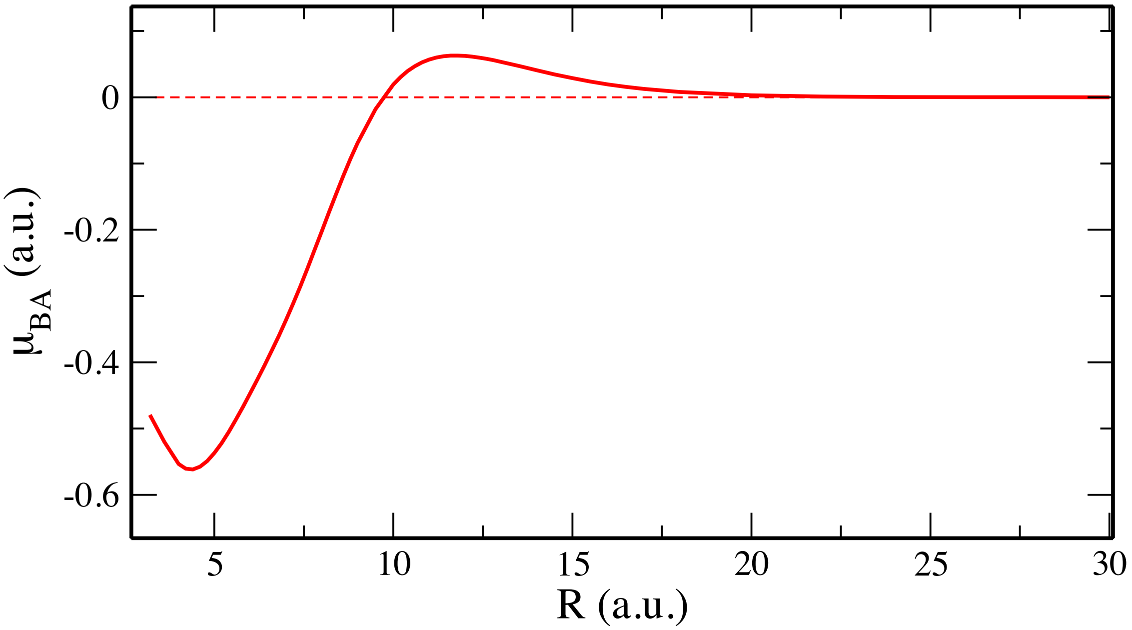

Figure 4.13. Computed electronic dipole transition moment μ_{BA} coupling the B $^2\Sigma_g^+$ to the A $^2\Pi_u$ state shown for Mg_2^+.

comprising of the Mg neutral atom in the excited ^{3}P state and the Mg^+ in the ground ^{2}S state (see Fig. 4.11). For calculating the static dipole and quadrupole polarizabilities, we have used finite field CCSD(T) method in `MOLPRO` with the aug-cc-pV5Z basis sets. Table 4.8 lists the values of polarizabilities for the X $^2\Sigma_u^+$, B $^2\Sigma_g^+$ and A $^2\Pi_u$ states of Mg_2^+. Our calculated values agree well with previous theoretical results of Derevianko *et al.* [68]. Table 4.9 lists all the values of calculated and derived long-range coefficients.

Table 4.8. The static atomic dipole and quadrupole polarizabilities for the X $^2\Sigma_u^+$, A $^2\Pi_u$ and B $^2\Sigma_g^+$ states of Mg_2^+. The values in square brackets indicates powers of ten. All values are in atomic units (a.u.).

Molecular State	Dipole polarizability (α_d)	Quadrupole polarizability (α_q)
X $^2\Sigma_u^+$, B $^2\Sigma_g^+$	7.502[1]	8.802[2]
Prev. theory [68]	7.224[1]	8.773[2]
A $^2\Pi_u$	8.892[1]	9.723[2]

Table 4.9. The long-range coefficients for the X $^2\Sigma_u^+$, A $^2\Pi_u$, and B $^2\Sigma_g^+$ states of Mg_2^+. The values in square brackets indicates powers of ten. All values are in atomic units (a.u.).

Molecular State	Quadrupole moment (Q)	C_3 ($= Q \times q$)	C_4 ($=\alpha_d/2$)	C_6'	C_6 ($=\alpha_q/2 + C_6'$)
X $^2\Sigma_u^+$, B $^2\Sigma_g^+$	—	—	3.751[1]	2.169[2]	6.570[2]
A $^2\Pi_u$	4.285	4.285	4.446[1]	2.118[2]	6.980[2]

4.5 Beyond the Born-Oppenheimer (BO) regime – Non-Adiabatic Corrections

In most studies of atomic and molecular properties, the Born-Oppenheimer approximation is an extremely good approximation since the nuclei are massive compared to electrons, and hence their motion can be neglected. However in studies of atom-ion collisions, especially those involving different isotopes, the motion of the nuclei must be taken into account. In this section we shall explore the regime where the Born-Oppenheimer approximation fails, and develop *ab initio* methods to account for the non-adiabatic corrections.

In the case of collisional studies between two isotopes of the same element, the charge transfer reaction becomes near-resonant rather than a resonant process; as is seen in previous studies with HD^+ [76] and Li_2^+ [77]. This near-resonant process is driven by the small non-adiabatic couplings between the two electronic states that are due to the small kinematic effects because of the finite nuclear mass. The molecular u–g symmetry is broken and the molecular states separate at large internuclear distances to asymptotic binding energies for $A + A'^+$ and for $A^+ + A'$, differing by a small amount ΔE that depends on the masses and, to a smaller extent, on the overlap of electronic wavefunctions with the nuclei. The Born-Oppenheimer approximation fails because its symmetry properties are determined by the electronic Hamiltonian only.

Here we have devised a scheme similar to that of Peng et al. [5] for calculating by means of *ab initio* methods the rather weak couplings due to non-BO corrections using a MCSCF/MRCI framework. All of the code has been implemented in `MOLPRO` quantum chemistry program (see Appendix C.1). We show here the non-BO corrections for the ^{9}Be^{10}Be$^+$ molecular ion. The study is extended into the more complicated systems of ^{24}Mg^{25}Mg$^+$ and ^{40}Ca^{43}Ca$^+$, whose results are shown in Appendix C.3.

The total Hamiltonian of the system including the motion of the nuclei can be written as [5]

$$H = T_N + T_e + T_{mp} + V_{int}(\boldsymbol{r}, \boldsymbol{R}) \,, \tag{4.7}$$

where T_N is the kinetic energy operator for the relative motion of the nuclei, T_{mp} is the mass polarization term, T_e is the electron kinetic energy, $\boldsymbol{R}$ is the vector connecting the nuclei, $\boldsymbol{r}$ measures the coordinates of electrons in the center of nuclear mass (CNM) frame, and $V_{int}(\boldsymbol{r}, \boldsymbol{R})$ contains all the electrostatic interactions. Combining $V_{int}(\boldsymbol{r}, \boldsymbol{R})$ and T_e yields the non- relativistic BO electronic Hamiltonian H_e.

The mass-polarization term arises because it is not possible to rigorously separate the centre of mass motion from the internal motion for a system with more than two particles. This reads as

$$T_{mp} = \sum_{i,j=1}^{N_e} -\frac{1}{2M_N} \nabla_i \nabla_j \,, \tag{4.8}$$

where M_N is the total nuclear mass and the summation runs over the total number of electrons. The matrix element of T_{mp} between BO eigenstates ψ_α and ψ_β is denoted as $\epsilon^{mp}_{\alpha\beta}$. Using standard quantum mechanical treatment (as shown in [5]), one can recast the time-independent radial Schrödinger equation in matrix form

$$\Big[\boldsymbol{I}\frac{d^2}{dR^2} + 2\mu\boldsymbol{F}\frac{d}{dR} + 2\mu\boldsymbol{E} - 2\mu\Big(\boldsymbol{I}\frac{J(J+1)-\lambda^2}{2\mu R^2} + \boldsymbol{V} - \boldsymbol{L}\Big)\Big]\boldsymbol{\chi} = 0 \,, \tag{4.9}$$

with $\boldsymbol{I}$ being the identity matrix and μ representing the reduced mass of the entire system. $\boldsymbol{F}$ and $\boldsymbol{L}$ matrices have only off-diagonal elements and approach zero asymptotically in the BO representation. The matrix $\boldsymbol{V}$ originates from the nuclear kinetic operator and the mass polarization term. Its diagonal elements are an adiabatic correction to the BO states. The off-diagonal elements couple the two $^2\Sigma^+$ states. Our goal is to calculate, the matrix elements of $\boldsymbol{V}$, $\boldsymbol{F}$ and $\boldsymbol{L}$, which would constitute the non-BO corrections. Our prototype system for all the calculations is the $^9\text{Be}^{10}\text{Be}^+$ molecular ion, for which the affected BO states are the X $^2\Sigma_u^+$, A $^2\Pi_u$, and B $^2\Sigma_g^+$ states. The non-BO matrix elements are defined as [5]

$$F_{\alpha\beta} = \frac{1}{\mu}\Big\langle\psi_\alpha\Big|\frac{\partial}{\partial R}\Big|\psi_\beta\Big\rangle\,, \tag{4.10}$$

$$V_{\alpha\beta} = \sum_{i=1}^{N_{nuc}}\Big\langle\psi_\alpha\Big| -\frac{1}{2M_i}\nabla_i^2\Big|\psi_\beta\Big\rangle\,, \tag{4.11}$$

and

$$\begin{aligned} L_{\alpha\beta} = \frac{1}{\mu R^2}\Big[&\sqrt{(J+\Lambda+1)(J-\Lambda)}\langle\psi_\alpha|iL_y|\psi_\beta\rangle \\ &-\sqrt{(J-\Lambda+1)(J+\Lambda)}\langle\psi_\alpha|iL_y|\psi_\beta\rangle\Big]\,. \end{aligned} \tag{4.12}$$

These non-BO matrix elements have been calculated in the *ab initio* framework, more details of which are provided in Appendix C.1. The most important correction to the BO regime is the diagonal BO correction, which breaks the u–g symmetry and separates the long-range into two distinct asymptotes depending on the mass of the nuclei. This is given by,

$$V_{\alpha\alpha} = \sum_{i=1}^{N_{nuc}}\Big\langle\psi_\alpha\Big| -\frac{1}{2M_i}\nabla_i^2\Big|\psi_\alpha\Big\rangle\,. \tag{4.13}$$

The inclusion of the diagonal BO correction in the potential energy curves for a particular system gives rise to the so-called "diabatic states". Both the diagonal and off-diagonal contributions of the $\boldsymbol{V}$ matrix is implemented by a numerical differentiation procedure as described in the previous work of Peng et al. [5].

We compute the overlap of the BO wave functions at displaced nuclear Cartesian coordinates

$$O_{\alpha\beta}^{\Delta x} = \langle \psi_\alpha(x - \Delta x; R) | \psi_\beta(x + \Delta x; R) \rangle \, , \tag{4.14}$$

where x represents the general nuclear cartesian coordinate and Δx is the displacement. For every value of internuclear separation R, we calculate the overlap of the electronic wavefunctions between the positive and negative displacements Δx, Δy and Δz corresponding to the nuclear cartesian coordinate x, y and z respectively. Using the four-point formula for numerical differentiation [5] we get for each coordinate I

$$V_{\alpha\beta,I} = \frac{1}{48\Delta x^2}\Big[16(O_{\alpha\beta}^{\Delta x} + O_{\beta\alpha}^{\Delta x}) - (O_{\alpha\beta}^{2\Delta x} + O_{\beta\alpha}^{2\Delta x}) - 30\delta_{\alpha\beta}\Big] \, , \tag{4.15}$$

and therefore

$$V_{\alpha\beta} = \sum_{I=1}^{N_{nuc}} -\frac{1}{2M_I} V_{\alpha\beta,I} \, . \tag{4.16}$$

We show in Fig. 4.14, the $V_{\alpha\beta}$ coupling between the X $^2\Sigma_u^+$ and B $^2\Sigma_g^+$ states in the ^{9}Be^{10}Be$^+$ molecular ion. The diagonal corrections V_{uu} and V_{gg}, when added to the BO states produce the diabatic potential energy curves. The g-u symmetry is broken and the asymptotes are separated to the limits of ^{9}Be$^+$ + ^{10}Be and ^{10}Be$^+$ +

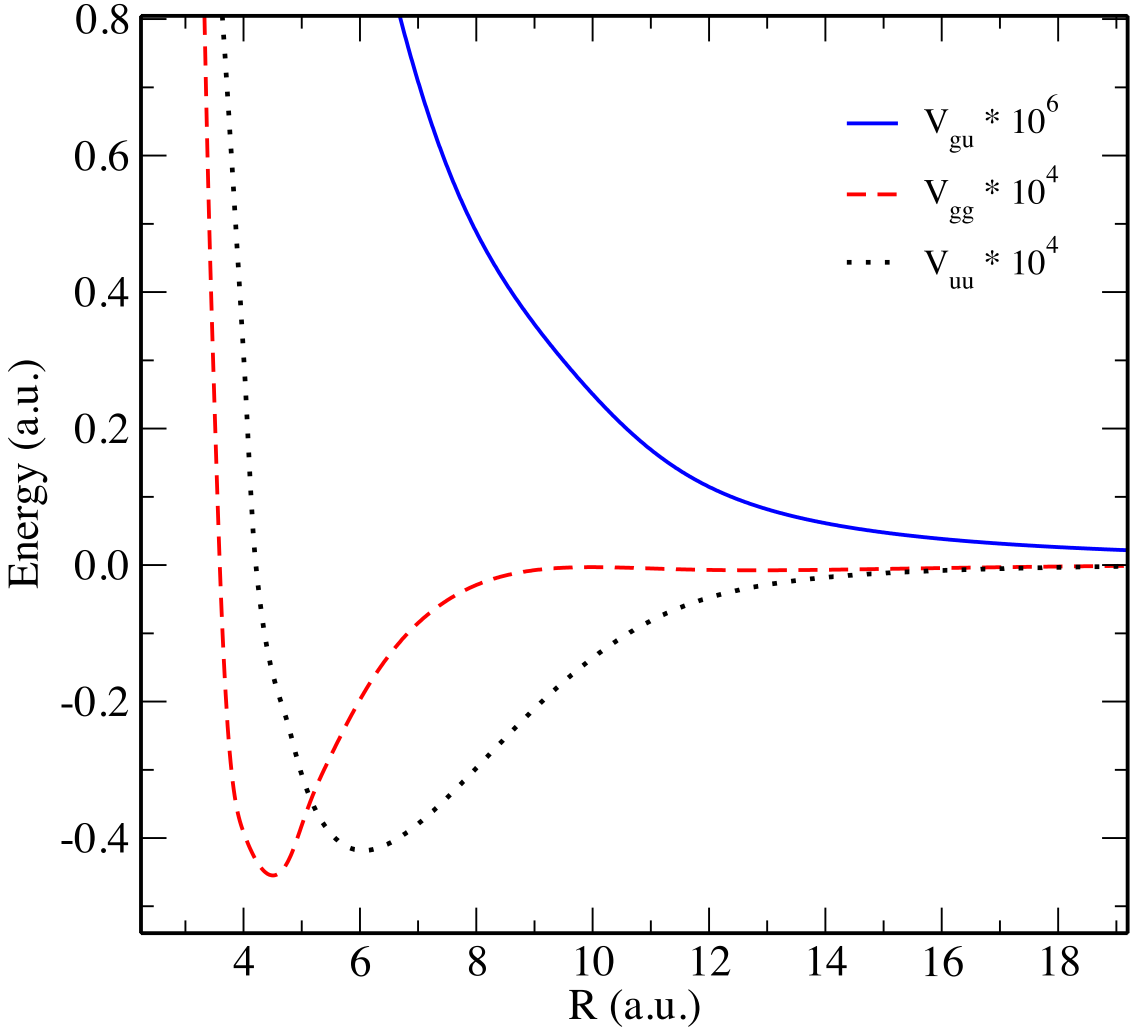

Figure 4.14. Calculated $V_{\alpha\beta}$ coupling between the X ${}^2\Sigma_u^+$ and B ${}^2\Sigma_g^+$ states in ^{9}Be^{10}Be${}^+$ molecular ion. The diagonal couplings (multiplied by 10^4) are shown in black (dotted) and red (dashed) lines, and off-diagonal coupling V_{gu} (multiplied by 10^6) is shown in blue (solid) line.

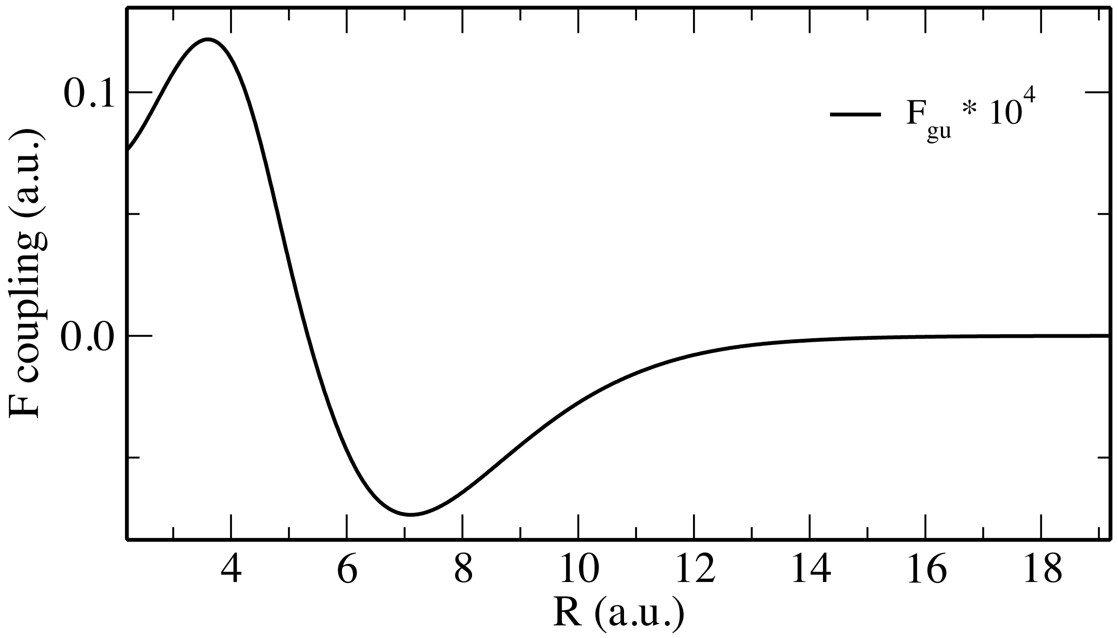

Figure 4.15. Calculated first derivative coupling (multiplied by 10^4) $F_{\alpha\beta}$ between the X $^2\Sigma_u^+$ and B $^2\Sigma_g^+$ states in ^{9}Be^{10}Be$^+$ molecular ion.

^{9}Be. The asymptotic difference is numerically equal to the off-diagonal correction V_{gu}.

The BO wavefunctions are calculated at MCSCF level of theory. The active space in this MCSCF wave function was composed of seven electrons in ten MOs, formed by 1s2s2p orbitals of the Be atoms. All *ab initio* calculations are performed using the `MOLPRO` program. Fig. 4.15 shows the first derivative coupling $F_{\alpha\beta}$ between the X $^2\Sigma_u^+$ and B $^2\Sigma_g^+$ states. Also, we calculate the L_y coupling between the X $^2\Sigma_u^+$ and A $^2\Pi_u$ states in ^{9}Be^{10}Be$^+$ molecular ion (see Fig. 4.16). As we have seen for $V_{\alpha\beta}$, all the off-diagonal couplings $F_{\alpha\beta}$ and $L_{\Sigma\Pi}$ are extremely small and more important for small internuclear separations.

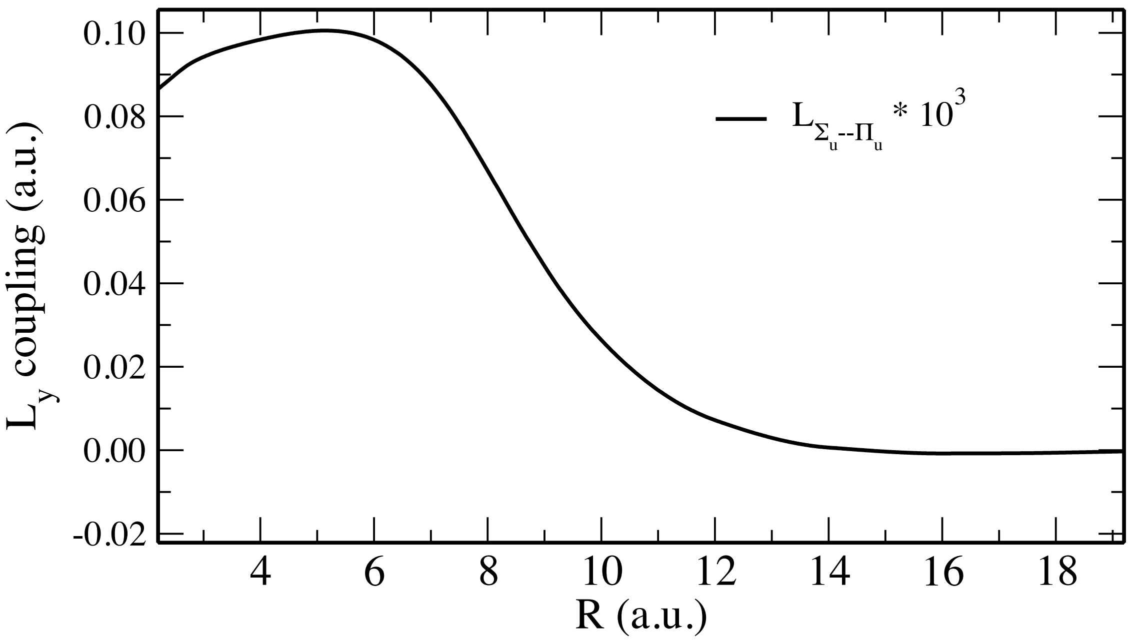

Figure 4.16. Calculated L_y coupling (multiplied by 10^3) between X $^2\Sigma_u^+$ and A $^2\Pi_u$ states of ^{9}Be^{10}Be$^+$.

4.6 A comparative study of all homonuclear alkaline-earth dimers

In the previous sections, we have presented a detailed analysis of the electronic structure and properties of homonuclear alkaline-earth molecular ions Ca_2^+, Sr_2^+, and Mg_2^+. This work was preceded by the *ab initio* calculations of the ground and excited states of the Be_2^+ dimer in Chapters 2 and 3. In this section we shall provide a qualitative comparison of the potentials in the alkaline-earth family of molecular ions and look more closely at the "double-well" B $^2\Sigma_g^+$ state. Owing to the similar valence electronic structure of these alkaline-earth ionic dimers, we expected a lot of similarities in the potential energy curves of these molecular ions. In all these cases we studied very carefully the lowest three states, namely the X $^2\Sigma_u^+$, A $^2\Pi_u$, and B $^2\Sigma_g^+$ states. Although the X and B states belong to the ground state asymptote, the first excited $^2\Pi$ state comes down strongly and intersects the B $^2\Sigma_g^+$ state thus becoming the lower lying state energetically, and is hence named the A state. We stick to this particular naming convention for all the elements in this series.

We show in Fig. 4.17 the potential energy curves for the X $^2\Sigma_u^+$, A $^2\Pi_u$, and B $^2\Sigma_g^+$ states of the Be_2^+, Mg_2^+, Ca_2^+, and Sr_2^+ molecular ions. The X $^2\Sigma_u^+$ state is always bound by $\sim$ 10,000 cm^{-1} for all these molecular ions. The equilibrium bond separation shifts to a higher value of inter-nuclear distance as one moves from Be to Sr due to the increase in size of the constituent atom/ion. The B $^2\Sigma_g^+$ state has a double minima for all these ionic dimers except Mg_2^+. The A $^2\Pi_u$ goes down strongly and intersects the $^2\Sigma$ states for all the alkaline-earth molecular ions. For Be, Ca, and Sr this intersection takes place below the dissociation energy of the ground $^2\Sigma$ states. We believe such perturbations at short-range would also affect long-range behavior like resonant charge transfer processes. In the case of Mg_2^+ the crossing takes place at energies much higher than the dissociation channel.

The presence of barriers and multiple minima in potential energy curves is always caused by interactions with an excited electronic state. For the case of the B $^2\Sigma_g^+$ state, the nearest state perturbing it is the next excited Σ_g^+ state. We use the respective *ab initio* methods developed for each one of the Be, Ca, Sr, and Mg molecular ions to calculate the excited 2 $^2\Sigma_g^+$ state. Fig. 4.18 shows a plot of the B $^2\Sigma_g^+$ and 2 $^2\Sigma_g^+$ states for Be_2^+, Ca_2^+, Sr_2^+, and Mg_2^+. From the curves in Fig. 4.18 we can qualitatively describe the interaction between the $^2\Sigma_g^+$ states in each of the species of alkaline-earth molecular ions. Two prominent double-wells has been observed for the Ca_2^+ and Sr_2^+ molecular ions, which is evident from the separation of the ground and excited state asymptotes ($<$ 15,000 cm^{-1}). In the case of both Be_2^+ and Mg_2^+ this separation of atomic asymptotes is $\sim$ 20,000 cm^{-1}, which is significantly higher

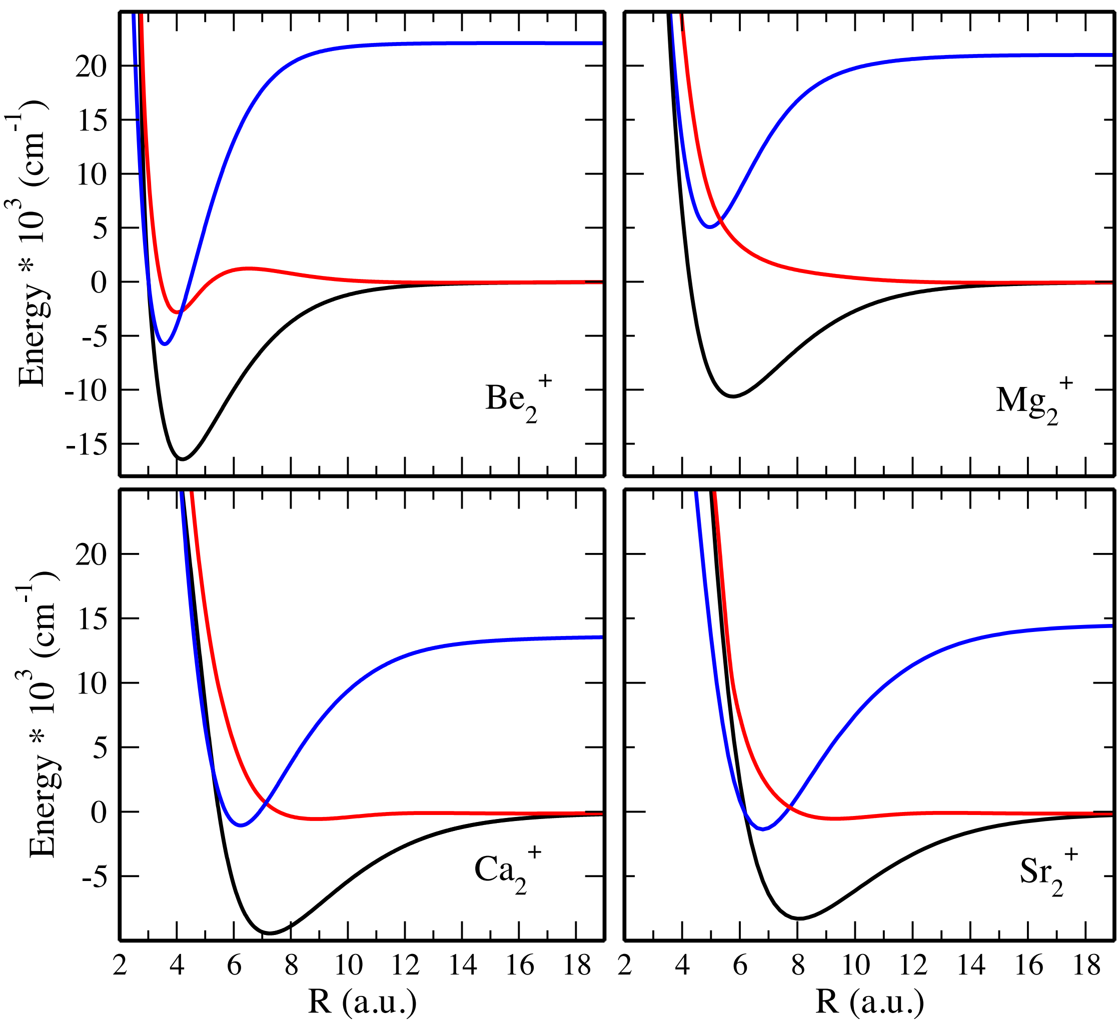

Figure 4.17. Calculated *ab initio* curves for the X $^2\Sigma_u^+$ (in black), A $^2\Pi_u$ (in blue) and B $^2\Sigma_g^+$ (in red) states of the Be_2^+, Mg_2^+, Ca_2^+ and Sr_2^+ molecular ions.

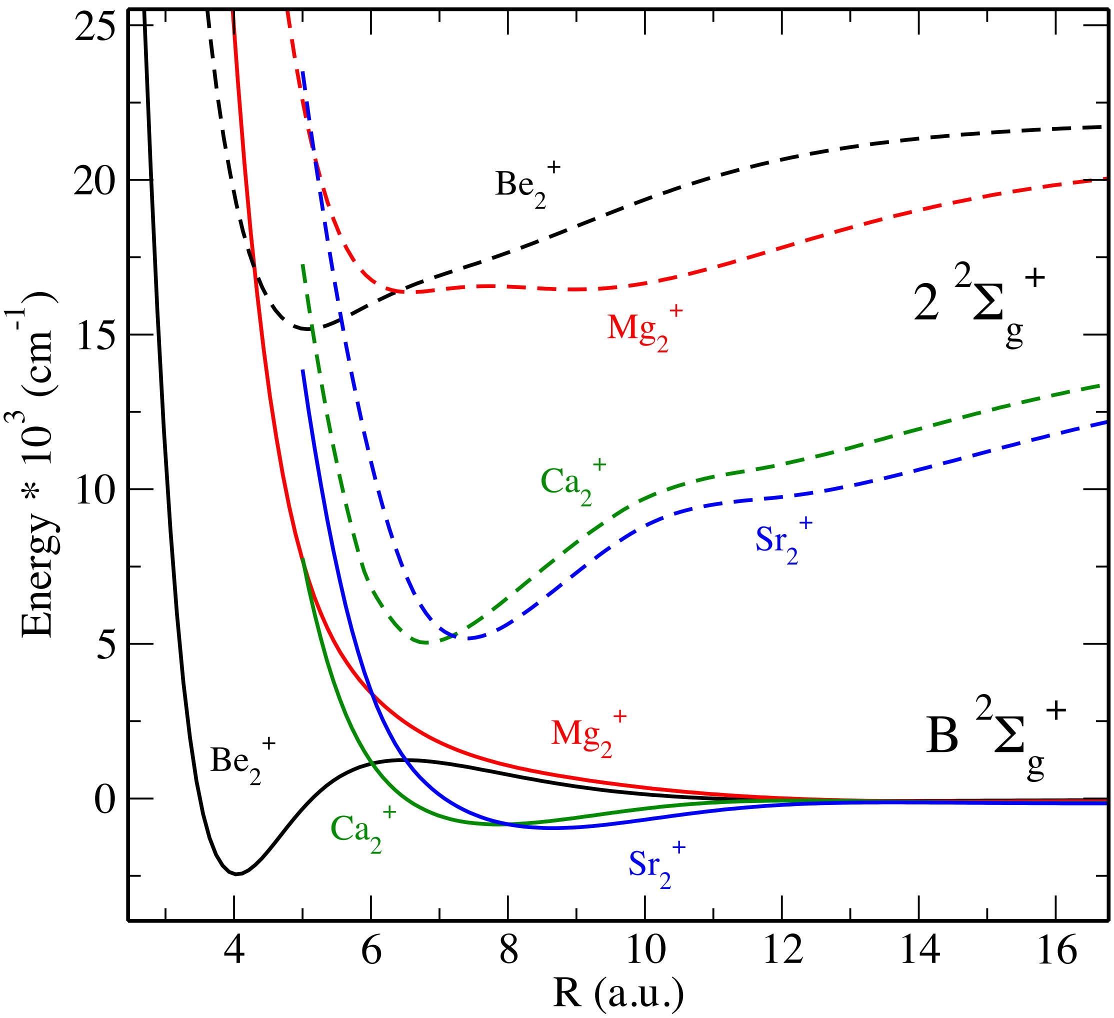

Figure 4.18. Calculated *ab initio* curves for the ground and excited $^2\Sigma_g^+$ states for Be_2^+ (in black), Mg_2^+ (in red), Ca_2^+ (in green) and Sr_2^+ (in blue). Solid lines represent the ground B $^2\Sigma_g^+$ state, whereas the dashed lines represent excited 2 $^2\Sigma_g^+$ states.

than the other members of this family. However in Be_2^+, the 2 $^2\Sigma_g^+$ state comes down very strongly at shorter separation and interacts with the ground B $^2\Sigma_g^+$ state, hence causing the double-well. In the case of Mg_2^+ though, the excited 2 $^2\Sigma_g^+$ state comes down but gets pulled up by an attractive interaction most likely from yet another excited state, and hence does not perturb the B $^2\Sigma_g^+$ state enough to form a double-well.

4.7 Long-Range — Inclusion of Exchange energy

The general form of long-range molecular potential is given as

$$V_{LR}(R) = E_{disp}(R) + E_{exch}(R)\,, \tag{4.17}$$

where $E_{disp}(R)$ is the collection of all dispersion terms in the long-range expansion and $E_{exch}(R)$ is the exchange energy contribution. In the previous sections for discussion on the long-range interaction, we have not included the contribution of the exchange energy term. Here we shall explore the various terms involved in the exchange energy contribution, and present a thorough comparison of the long-range of the Be_2^+, Mg_2^+, Ca_2^+, and Sr_2^+ molecular ions including both dispersion and exchange energy contributions.

The analytic expression for exchange energy as a function of internuclear separation R is given by [77],

$$E_{exch}(R) = \frac{1}{2}AR^{\alpha}e^{-\beta R}\Big[1 + \frac{B}{R} + \frac{C}{R^2} + ...\Big]\,. \tag{4.18}$$

This long-range expansion was studied in great detail by Bardsley *et al.* [78] and the parameters α, β and B are related by simple expressions connecting the ionization potential ϵ of the constituent atoms, in a homonuclear system. They are defined as

$$\beta = \sqrt{2 \times \epsilon}\,, \tag{4.19}$$

$$\alpha = (2\nu - 1)\,, \tag{4.20}$$

$$B = \nu^2\Big(\frac{3}{2}\nu - 1\Big)\,, \tag{4.21}$$

where ν=$1/\beta$. In order to obtain the exchange energy for Be_2^+ we calculate the ionization energy ϵ for Be atom at same level of theory as our potential energy curve

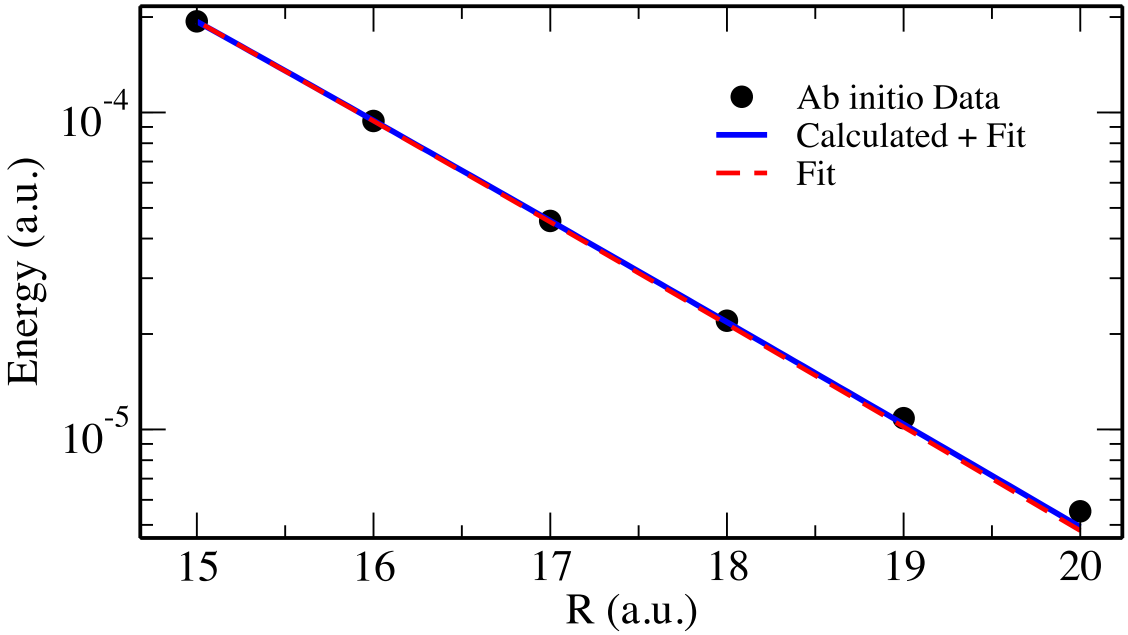

Figure 4.19. Exchange energy and comparison of *ab initio* data and numerical fit, in Be_2^+. Starting at R=20 onwards, numerical inaccuracies become significant.

calculations. Using this value of ϵ we can evaluate the expansion parameters α, β, and B from Bardsley's equations (shown above). The amplitude A and second order expansion coefficient C are obtained from numerical fit of Eq. (4.18) with the *ab initio* data. Note that the sign of C is negative which is consistent with previous calculations of alkali molecular ions [77], and also analytic results of H_2^+ [79, 80],

$$\begin{aligned} E_{exch}^{H_2^+}(R) &= 2Re^{-R-1}\Big(1+\frac{1}{2R}-\frac{25}{8R^2}-\frac{131}{48R^3}-\frac{3923}{384R^4} \\ &- \frac{145399}{3840R^5}-\frac{5219189}{46080R^6}-\frac{509102915}{645120R^7}-\frac{37749539911}{10321920R^8}\Big). \end{aligned} \tag{4.22}$$

We show in Fig. 4.19, the exchange energy for Be_2^+. We plot the difference of *ab initio* B $^2\Sigma_g^+$ and X $^2\Sigma_u^+$ potential energy curves on a log scale and numerically fit it with Eq. (4.18). We see very good agreement for the exchange energy of Be_2^+.

Table 4.10. Long-range expansion coefficients for the X $^2\Sigma_u^+$ and B $^2\Sigma_g^+$ states of homonuclear alkaline-earth molecular ions. All values are in atomic units. The numbers in square brackets indicates powers of ten.

Expansion coefficients	Be_2^+	Mg_2^+	Ca_2^+	Sr_2^+
α_d	3.812[1]	7.502[1]	1.606[2]	1.936[2]
α_q	3.000[2]	8.802[1]	3.073[3]	4.633[3]
C'_6	1.242[2]	2.169[2]	1.081[3]	3.653[3]
C_4 (=$\alpha_d/2$)	1.906[1]	3.751[1]	8.032[1]	9.680[1]
C_6 (=$\alpha_q/2$ + C'_6)	2.742[2]	6.570[2]	2.618[3]	5.970[3]
A	1.094	0.769	0.364	0.301
ϵ	0.341	0.280	0.224	0.208
α (calculated)	1.419	1.667	1.983	2.091
α (fitted)	1.472	1.671	1.992	2.101
β (calculated)	0.826	0.749	0.670	0.646
β (fitted)	0.835	0.748	0.682	0.651
B (calculated)	1.191	1.781	2.754	3.150
B (fitted)	1.103	1.799	2.764	3.162
C	-3.576[1]	-5.118[1]	-7.050[1]	-8.881[1]

Starting at R=20 a.u. onwards, the *ab initio* calculations reach the limit of numerical accuracies which is typically around 10^{-6} a.u. ($\sim$ 0.1 cm^{-1}). We also perform similar analysis for the long-range of other homonuclear molecular ions Mg_2^+, Ca_2^+, and Sr_2^+. We present in Table 4.10 a comprehensive list of all long-range coefficients, both dispersion and exchange energy contributions for all the molecular ions.

4.8 Concluding Remarks

In this chapter, we have shown in detail the *ab initio* calculations involved in the electronic structure determination and properties of the alkaline-earth family of molecular ions. Although the dimers have very similar valence electronic configuration, the intricacies of the core-valence and relativistic effects make determination of a unique *ab initio* method that would describe each one of the species accurately impossible. We thus sub-divided the chapter into Sections, dedicated to Ca_2^+, Sr_2^+, and Mg_2^+ to distinguish the differences in the details of computation.

Aside from computing the potential energy curves we have also provided spectroscopic values of the desired electronic states, transition dipole moments, radiative lifetimes, polarizability, and long-range analysis of all (except Ba_2^+) alkaline-earth molecular ions. Last but not the least, we provide a qualitative treatment of the comparison of the different alkaline-earth ionic dimers giving particular attention to the double-well structure in the B $^2\Sigma_g^+$ state.

Chapter 5

Heteronuclear alkaline-earth molecular ions — BeMg$^+$, BeCa$^+$ and MgCa$^+$

5.1 Overview of the problem

In the previous chapters, we have calculated *ab initio* potential curves for the ground and low lying excited states of homonuclear alkaline-earth molecular ions — Be$_2^+$, Mg$_2^+$, Ca$_2^+$, and Sr$_2^+$. We discussed in detail the methods involved in the computation and obtained properties like transition dipole moments, radiative lifetimes, spectroscopy, and long-range coefficients. In this chapter, we extend our calculations to study heteronuclear alkaline-earth molecular ions using very similar methods.

Let us consider heteronuclear alkaline-earth molecular ion XY$^+$, where X, Y can be Be, Mg or Ca. The ground state can be formed by the combination of X and Y$^+$ or Y and X$^+$, since X and Y are distinguishable. This is shown schematically in Fig. 5.1. The configuration lower in energy determines the ground X $^2\Sigma^+$ state asymptote.

We also calculate the lowest lying excited states for $^2\Sigma^+$ and $^2\Pi$ symmetries. In order to choose which excitations to calculate, we adopt a simple rule; we consider every possible state, arising from single excitations from the ground asymptote. The reason for this choice is that one-photon excitations can be experimentally achieved more simply. Once again, let us refer to our schematic description of a molecular ion

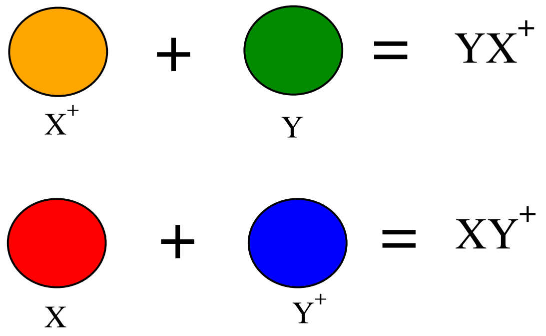

Figure 5.1. Diagram of ground state constituent atom/ions in a heteronuclear molecular ion XY^+.

XY^+ to elaborate this point. We illustrate the possible manifold of excited states in Fig. 5.2. $(X)^*$ represents the atom in its excited state, while $(X^+)^*$ represents the ion in its excited state.

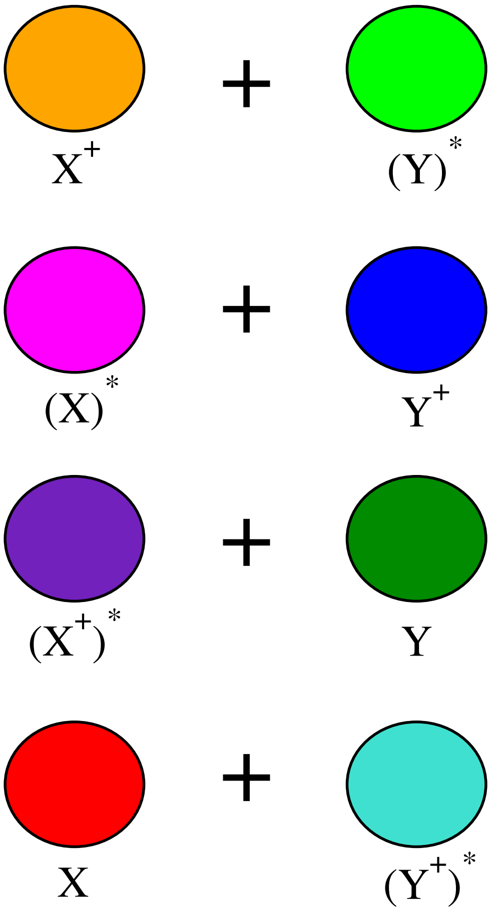

Figure 5.2. Diagram of the excited state manifold in a heteronuclear molecular ion XY^+ formed by single excitations.

5.2 Methods and Basis Sets

We use similar methods as developed in the previous chapters. For each of $BeMg^+$, $BeCa^+$, and $MgCa^+$ systems, we use a complete active space (CAS) comprising of *s*, *p* and *d* orbitals; as a reference to perform MRCI calculations. We use the effective-core potential (ECP) approach to describe the core-valence electron correlation. We list below the ECP+basis functions used for Be and Mg [81] in `MOLPRO` format. The ECP+CPP for Ca has already been mentioned in Chapter 4.

```
basis={
!
! basis set from SBK-LFK (EMSL)
!
! BERYLLIUM        (4s,5p,4d) -> [2s,3p,2d]
! BERYLLIUM        (4s,5p,4d) -> [2s,3p,2d]
s, BE , 1.447000000, 0.352200000, 0.121900000, 0.043950000
c, 1.3, -0.15647000, 0.10919000, 0.67538000
c, 4.4, 0.32987000
p, BE , 0.100498500, 1.447000000, 0.352200000, 0.121900000, 0.043950000
c, 1.1, 1
c, 2.4, 0.08924000, 0.30999000, 0.51842000
c, 5.5, 0.27911000
d, BE , 0.321727700, 0.103393000, 0.053121400, 0.012485900
c, 1.2, 0.41435500, 1.00000000
c, 3.4, 0.06302500, 1.00000000

! ECP+CPP from Stutgart website
!Q=2., SEFIT, DF, Ref 5; CPP: alpha=0.052;delta=1.28;ncut=1.
ECP,Be,2,2,0;
1; 2,1.000000,0.000000;
1; 2,2.653000,13.325000;
1; 2,3.120000,-1.574000;
!
!
!cpp,init,1;
!be,1,0.052,,,1.28;
}
```

```
basis={
!
! ECP + CPP from Stutgart website
!  Q=2., SEFIT, DF, Ref 5; CPP: alpha=0.476;delta=0.87;ncut=1.
ECP,Mg,10,3,0;
1; 2,1.000000,0.000000;
1; 2,1.732000,14.676000;
1; 2,1.115000,5.175700;
1; 2,1.203000,-1.816000;
!
!
s, Mg , 4.302235, 0.753995, 0.067089, 0.039, 0.01752,
0.006, 0.003, 0.001
c, 1.2, -0.013469, -0.134665
c, 3.3, 1
c, 4.4, 1
c, 5.5, 1
c, 6.6, 1
c, 7.7, 1
c, 8.8, 1
!
p, Mg , 0.2, 0.085, 0.020, 0.004, 0.0009
c, 1.1, 1
c, 2.2, 1
c, 3.3, 1
c, 4.4, 1
c, 5.5, 1
d, Mg , 1.455, 0.4332, 0.10839, 0.024635
c, 1.2, 0.02754, 0.05391
c, 3.3, 1
c, 4.4, 1
f, Mg , 0.015, 0.0005
c, 1.1, 1
c, 2.2, 1
!
!
!cpp,init,1;
!mg,1,0.476,,,0.87
}
```

5.3 Potential energy curves and Spectroscopic Constants

As mentioned in the beginning of the chapter, before we calculate potential energy curves, it is essential to list down which states we are interested in. A map of the various energy asymptotes of the constituent atom/ions and the possible molecular states arising from the respective asymptotes is called a "molecular correlation diagram". Such a map is key to identifying the required electronic states for the *ab initio* calculation.

We subdivide this section into three sub-sections, one each for BeMg^+, BeCa^+, and MgCa^+. For each one of them, we also list the molecular correlation diagram.

5.3.1 BeMg$^+$

Table 5.1 shows the correlation diagram for the lowest asymptotes in the BeMg^+ molecular ion. Figs. 5.3 and 5.4 show the *ab initio* potential energy curves for the low lying $^2\Sigma^+$ and $^2\Pi$ states, respectively.

Table 5.1. The lowest asymptotes for $BeMg^+$. We note that channel VI is a double excitation, which is energetically lower than the channel VII asymptote.

Channel	Asymptote	Molecular states
I	$Be(^1S) + Mg^+(^2S)$	$^2\Sigma^+$
II	$Mg(^1S) + Be^+(^2S)$	$^2\Sigma^+$
III	$Be^*(^3P) + Mg^+(^2S)$	$^2\Sigma^+$, $^2\Pi$
IV	$Mg^*(^3P) + Be^+(^2S)$	$^2\Sigma^+$, $^2\Pi$
V	$(Mg^+)^*(^2P) + Be(^1S)$	$^2\Sigma^+$, $^2\Pi$
VI	$Be^{**}(^1P) + Mg^+(^2S)$	$^2\Sigma^+$, $^2\Pi$
VII	$(Be^+)^*(^2P) + Mg(^1S)$	$^2\Sigma^+$, $^2\Pi$

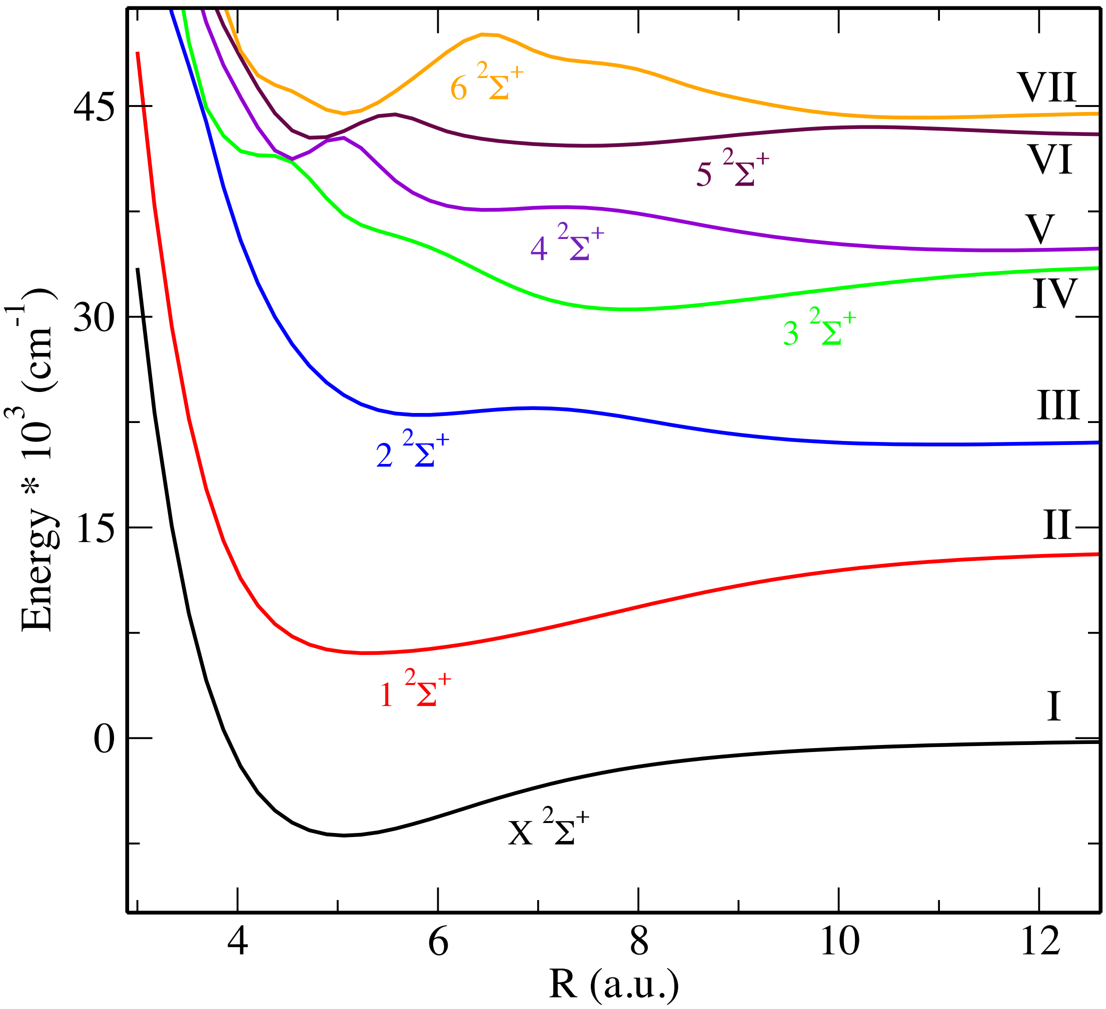

Figure 5.3. The figure shows the ground and low lying excited states of $^2\Sigma^+$ symmetry in BeMg$^+$. The asymptotes are listed in Table 5.1.

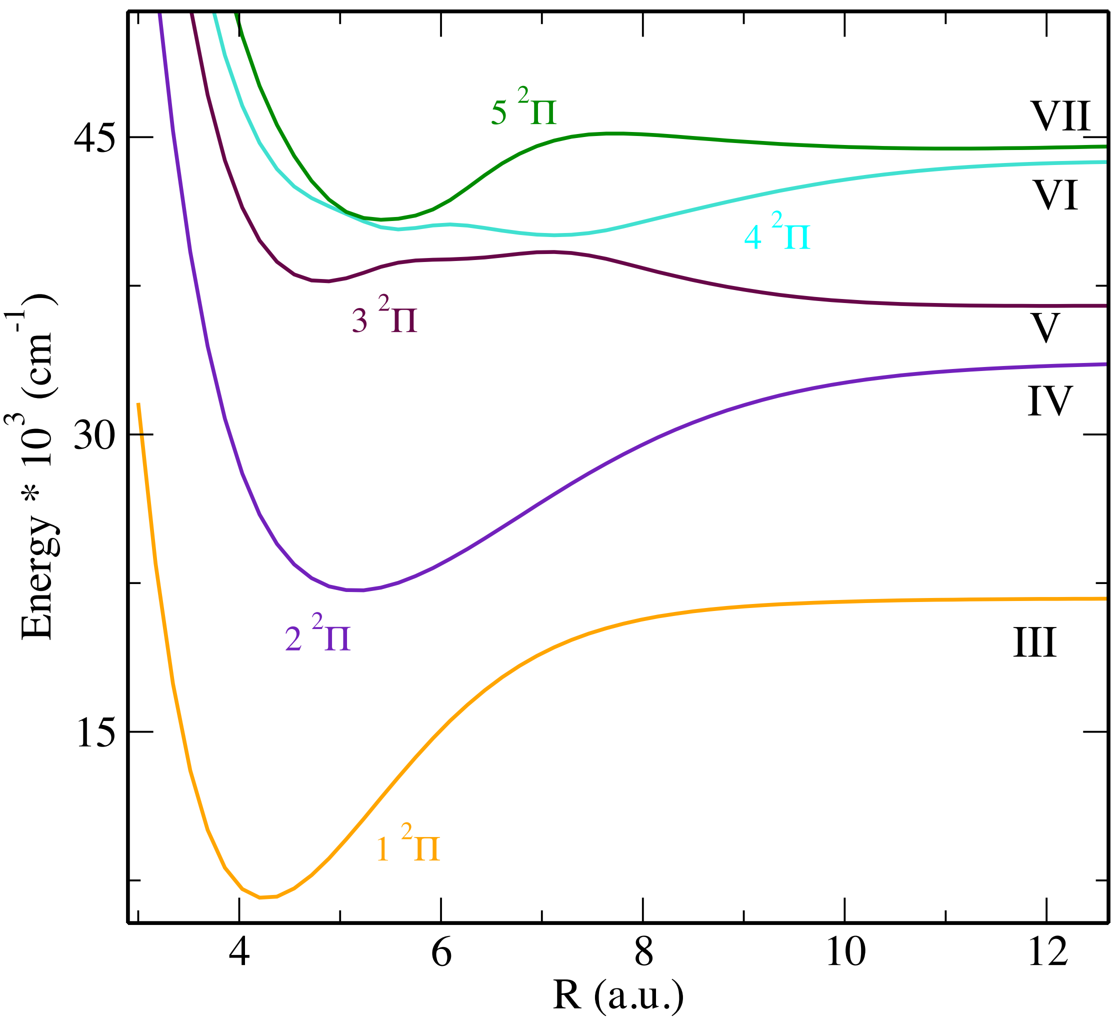

Figure 5.4. The figure shows the low lying $^2\Pi$ states in BeMg$^+$. The asymptotes are listed in Table 5.1.

Table 5.2. The lowest asymptotes for BeCa$^+$.

Channel	Asymptote	Molecular states
I	Be(^{1}S) + Ca$^+$(^{2}S)	$^2\Sigma^+$
II	(Ca$^+$)*(^{2}D) + Be(^{1}S)	$^2\Sigma^+$, $^2\Pi$, $^2\Delta$
III	Be*(^{3}P) + Ca$^+$(^{2}S)	$^2\Sigma^+$, $^2\Pi$
IV	(Ca$^+$)**(^{2}P) + Be(^{1}S)	$^2\Sigma^+$, $^2\Pi$
V	Ca(^{1}S) + Be$^+$(^{2}S)	$^2\Sigma^+$
VI	(Be$^+$)*(^{2}P) + Ca(^{1}S)	$^2\Sigma^+$, $^2\Pi$

5.3.2 BeCa$^+$

Table 5.2 shows the correlation diagram for the lowest asymptotes in the BeCa$^+$ molecular ion. Figs. 5.5 and 5.6 show the *ab initio* potential energy curves for the low lying $^2\Sigma^+$ and $^2\Pi$ states, respectively. Due to low lying excitations in the Ca$^+$ molecular ion, the second $^2\Sigma^+$ state (from channel V) lies much higher in the correlation diagram and after three excited asymptotes.

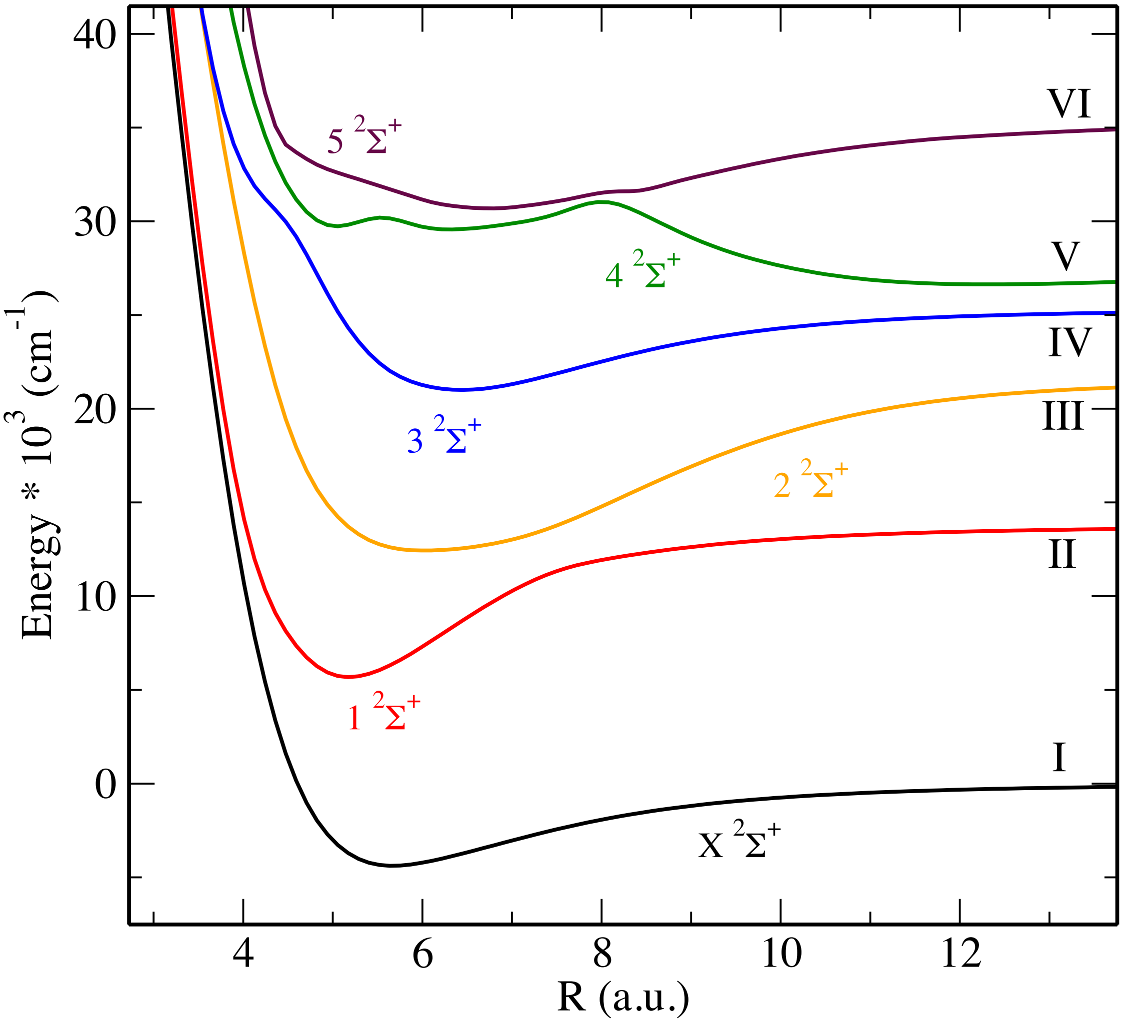

Figure 5.5. The figure shows the ground and low lying excited states of $^2\Sigma^+$ symmetry in BeCa$^+$. The asymptotes are listed in Table 5.2.

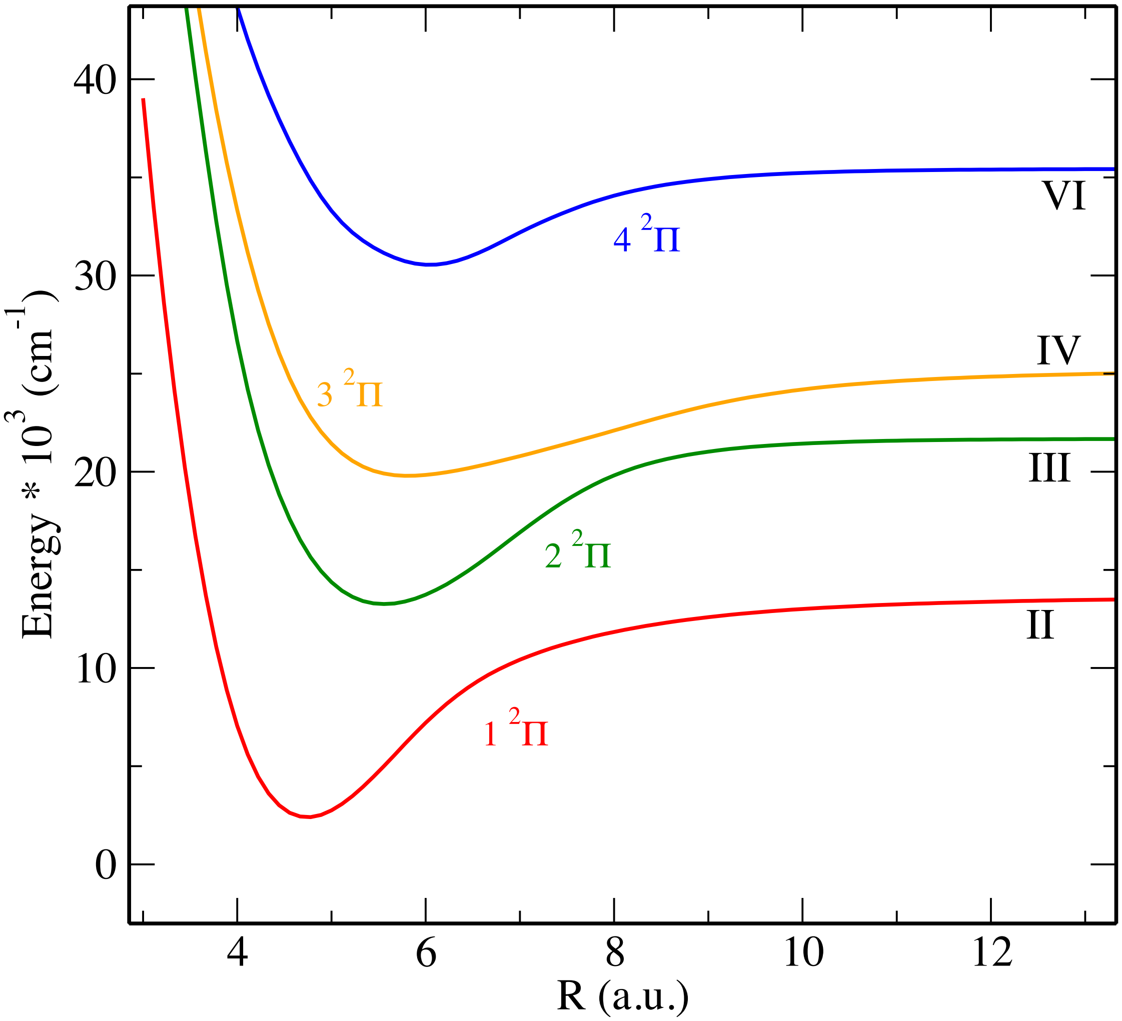

Figure 5.6. The figure shows the low lying $^2\Pi$ states in BeCa$^+$. The asymptotes are listed in Table 5.2.

Table 5.3. The lowest asymptotes for MgCa^+.

Channel	Asymptote	Molecular states
I	$\text{Mg}(^1\text{S}) + \text{Ca}^+(^2\text{S})$	$^2\Sigma^+$
II	$\text{Ca}(^1\text{S}) + \text{Mg}^+(^2\text{S})$	$^2\Sigma^+$
III	$(\text{Ca}^+)^*(^2\text{D}) + \text{Mg}(^1\text{S})$	$^2\Sigma^+$, $^2\Pi$, $^2\Delta$
IV	$\text{Mg}^*(^3\text{P}) + \text{Ca}^+(^2\text{S})$	$^2\Sigma^+$, $^2\Pi$
V	$(\text{Ca}^+)^{**}(^2\text{P}) + \text{Mg}(^1\text{S})$	$^2\Sigma^+$, $^2\Pi$
VI	$\text{Ca}^*(^3\text{P}) + \text{Mg}^+(^2\text{S})$	$^2\Sigma^+$, $^2\Pi$

5.3.3 MgCa$^+$

Table 5.3 shows the correlation diagram for the lowest asymptotes in the MgCa^+ molecular ion. Figs. 5.7 and 5.8 show the *ab initio* potential energy curves for the low lying $^2\Sigma^+$ and $^2\Pi$ states, respectively.

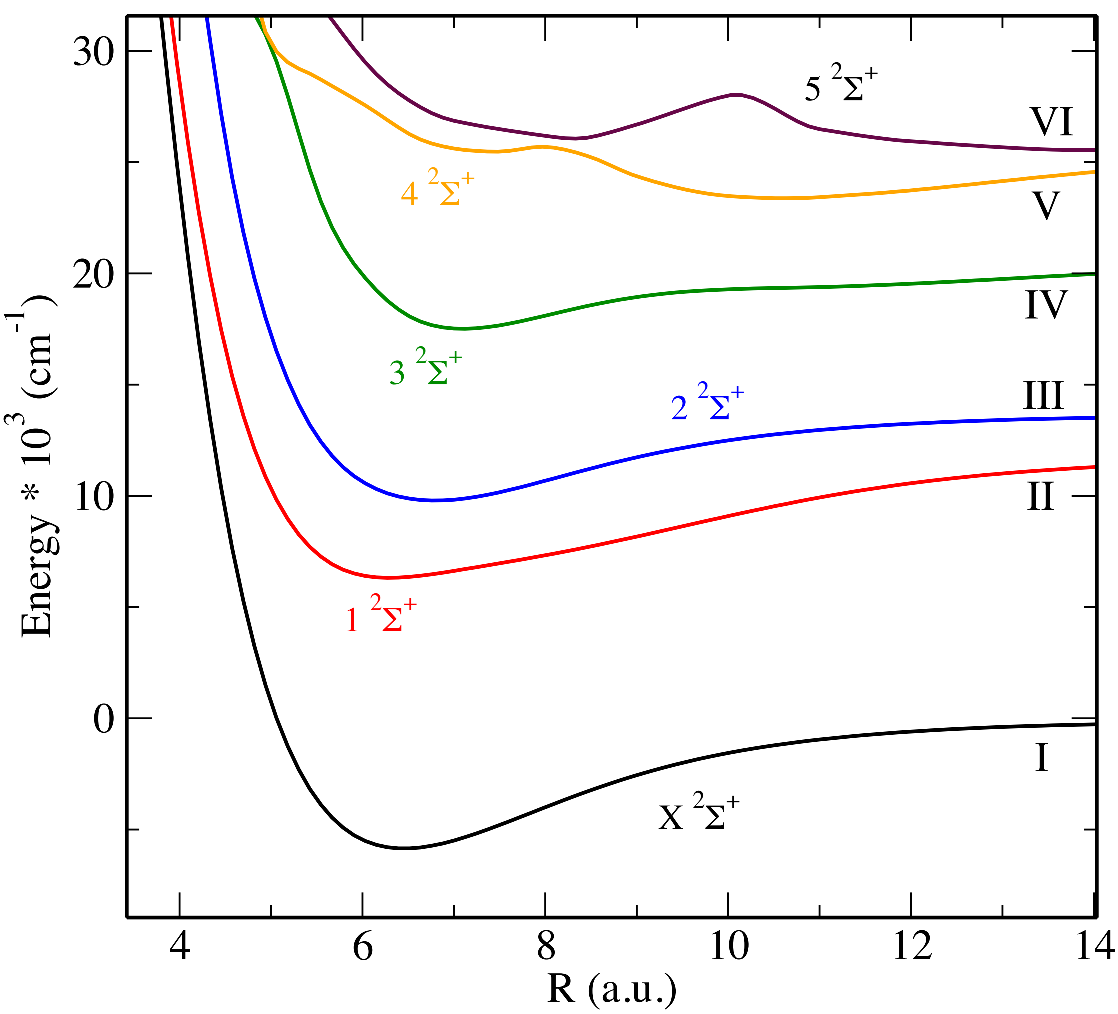

Figure 5.7. The figure shows the ground and low lying excited states of $^2\Sigma^+$ symmetry in MgCa$^+$. The asymptotes are listed in Table 5.3.

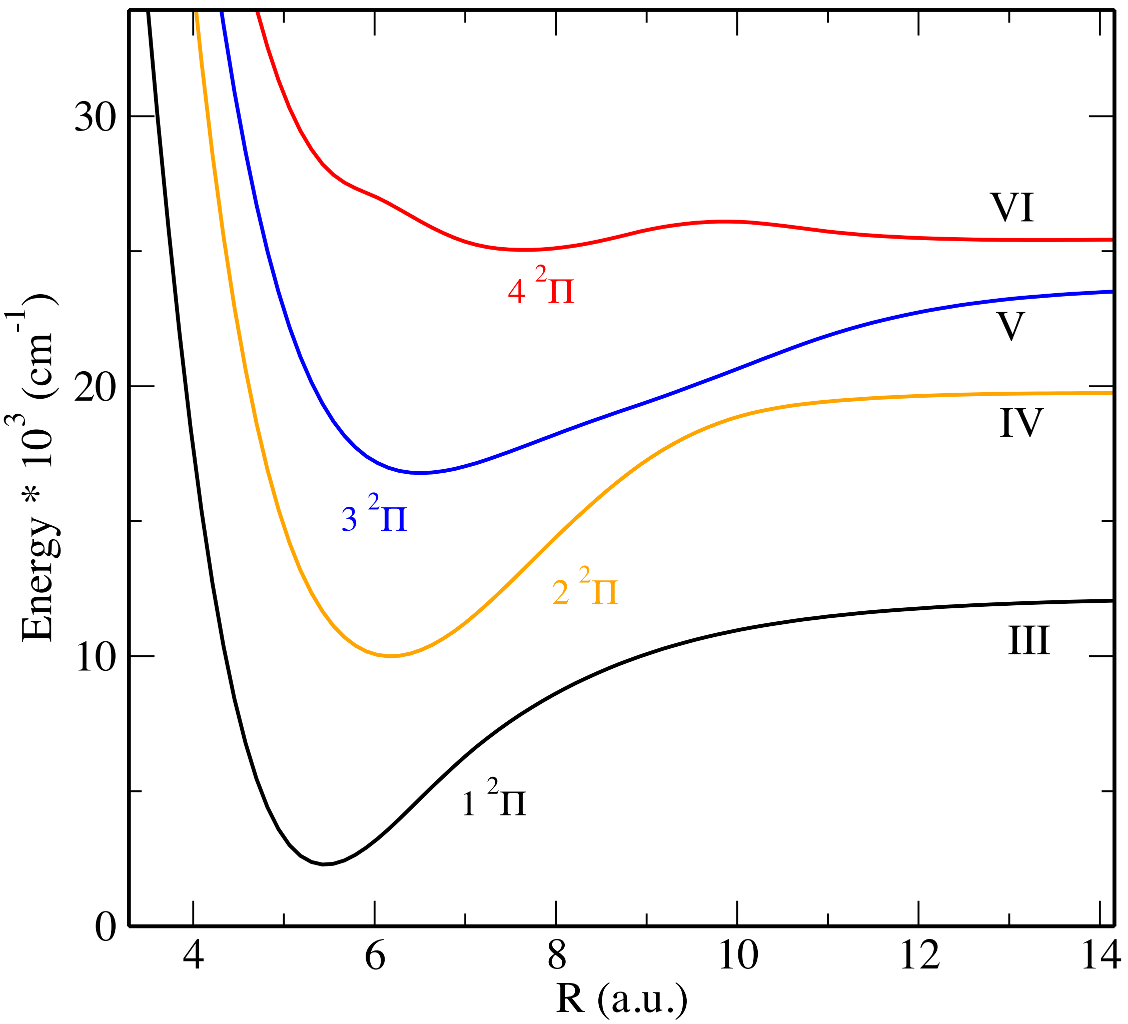

Figure 5.8. The figure shows the low lying $^2\Pi$ states in MgCa$^+$. The asymptotes are listed in Table 5.3.

Table 5.4. Spectroscopic constants for the absolute ground X $^2\Sigma^+$ state in the BeMg$^+$, BeCa$^+$ and MgCa$^+$ molecular ions.

Molecular Ion	r_e (Å)	B_e (cm^{-1})	ω_e (cm^{-1})	$\omega_e x_e$ (cm^{-1})	D_e (cm^{-1})
BeCa$^+$	2.998	0.254	254.158	6.472	4387
BeMg$^+$	2.683	0.356	303.306	2.552	6933
MgCa$^+$	3.416	0.095	156.779	0.852	5851

5.3.4 Spectroscopic Constants — X $^2\Sigma^+$ state

Table 5.4 lists the spectroscopic constants r_e, B_e, ω_e, $\omega_e x_e$ and D_e for the absolute ground X $^2\Sigma^+$ state for BeMg$^+$, BeCa$^+$ and MgCa$^+$ molecular ions. Dunham analysis was used to calculate the spectroscopic constants.

5.4 Concluding Remarks

We calculate accurate *ab initio* potential energy curves to describe the ground and low lying excited states of heteronuclear alkaline-earth molecular ions – BeMg$^+$, BeCa$^+$ and MgCa$^+$. We also perform a Dunham analysis to calculate spectroscopic constants for the absolute ground X $^2\Sigma^+$ in all these species.

Chapter 6

Mixed alkali alkaline-earth systems — An application to Hyperfine Structure

6.1 Example of the NaCa$^+$ molecular ion

In this chapter, we discuss electronic structure calculations pertaining to a specific heteronuclear alkali alkaline-earth system – NaCa$^+$. The primary focus of this chapter is to study the very complicated hyperfine structure of molecular ions arising from their nuclear spins and electric quadrupole interactions. A combination of alkali and alkaline-earth system brings the key elements of each of their families together, thereby making the system much richer than a traditional heteronuclear species of either alkali or alkaline-earth element.

Of particular interest is the fact that the most abundant isotope for alkaline earth elements has zero nuclear spin. So using a mixed alkali alkaline-earth species, one can obtain a very clean and simple hyperfine spectrum. Thus, we are most interested in studying the ^{23}Na^{40}Ca$^+$ system, although we shall briefly consider the example of the ^{43}Ca isotope, which has a non-zero nuclear spin. Owing to the closed valence shell, the absolute ground state of this system is X $^1\Sigma^+$, unlike doublets for the alkaline-earth species. We calculate accurate *ab initio* curves for the ground and low lying excited states for the NaCa$^+$ molecular ions and study the hyperfine structure of the lowest singlet X $^1\Sigma^+$ and triplet a $^3\Sigma^+$ state.

6.2 Potential Energy Curves

The ground and low lying excited states in NaCa$^+$ were calculated using similar methods developed previously. We use a 2 electron, 18 orbital complete active space as a reference to perform MRCI calculations, with the `MOLPRO` program. We have also used the equation of motion coupled cluster (EOM-CCSD) method to calculate and compare the singlet ground and excited states. In this situation, for two valence electrons, CCSD is equivalent to full CI. We get very good agreement between MRCI and CCSD potential energy curves. Since the EOM program is able to calculate only the singlet states, we had to rely purely on the CAS+MRCI method for the calculation of triplet states. The ECP+CPP approach has been used as well for the description of core-valence correlations. Basis sets corresponding to the ECP for Na were obtained from Dulieu *et al.* [82]. ECP and basis sets used for Ca [63] were the same as that used previously.

Table 6.1 shows the correlation diagram for the lowest asymptotes in the NaCa$^+$ molecular ion. Fig. 6.1 shows the *ab initio* potential energy curves for the low lying $^1\Sigma^+$ and $^3\Sigma^+$ states. As described in the previous chapter, the molecular correlation diagram gives a map of the different asymptotes, and the electronic states arising from them. As mentioned in the previous section, the correlation diagram shows the richer manifold of states arising from the different atomic asymptotes. As before, we are most interested in studying single excitations of the constituent atoms, especially Na (2S↔2P) resonance transition. Hence, we show in Fig. 6.1 potential energy curves arising from asymptotes I, II and VIII.

Table 6.1. The lowest asymptotes for $NaCa^+$. A single (*) represents a single excitation for an atom/ion, double (**) for double excitation and so on.

Channel	Asymptote	Molecular states
I	$Na^+(^1S) + Ca(^1S)$	$^1\Sigma^+$
II	$Na(^2S) + Ca^+(^2S)$	$^1\Sigma^+$, $^3\Sigma^+$
III	$Na^+(^1S) + Ca^*(^3P)$	$^3\Sigma^+$, $^3\Pi$
IV	$Na^+(^1S) + Ca^{**}(^3D)$	$^3\Sigma^+$, $^3\Pi$, $^3\Delta$
V	$Na(^2S) + (Ca^+)^*(^2D)$	$^1\Sigma^+$, $^1\Pi$, $^1\Delta$
		$^3\Sigma^+$, $^3\Pi$, $^3\Delta$
VI	$Na^+(^1S) + Ca^{***}(^1D)$	$^1\Sigma^+$, $^1\Pi$, $^1\Delta$
VII	$Na^+(^1S) + Ca^{****}(^1P)$	$^1\Sigma^+$, $^1\Pi$
VIII	$Na^*(^2P) + Ca^+(^2S)$	$^1\Sigma^+$, $^1\Pi$, $^3\Sigma^+$, $^3\Pi$

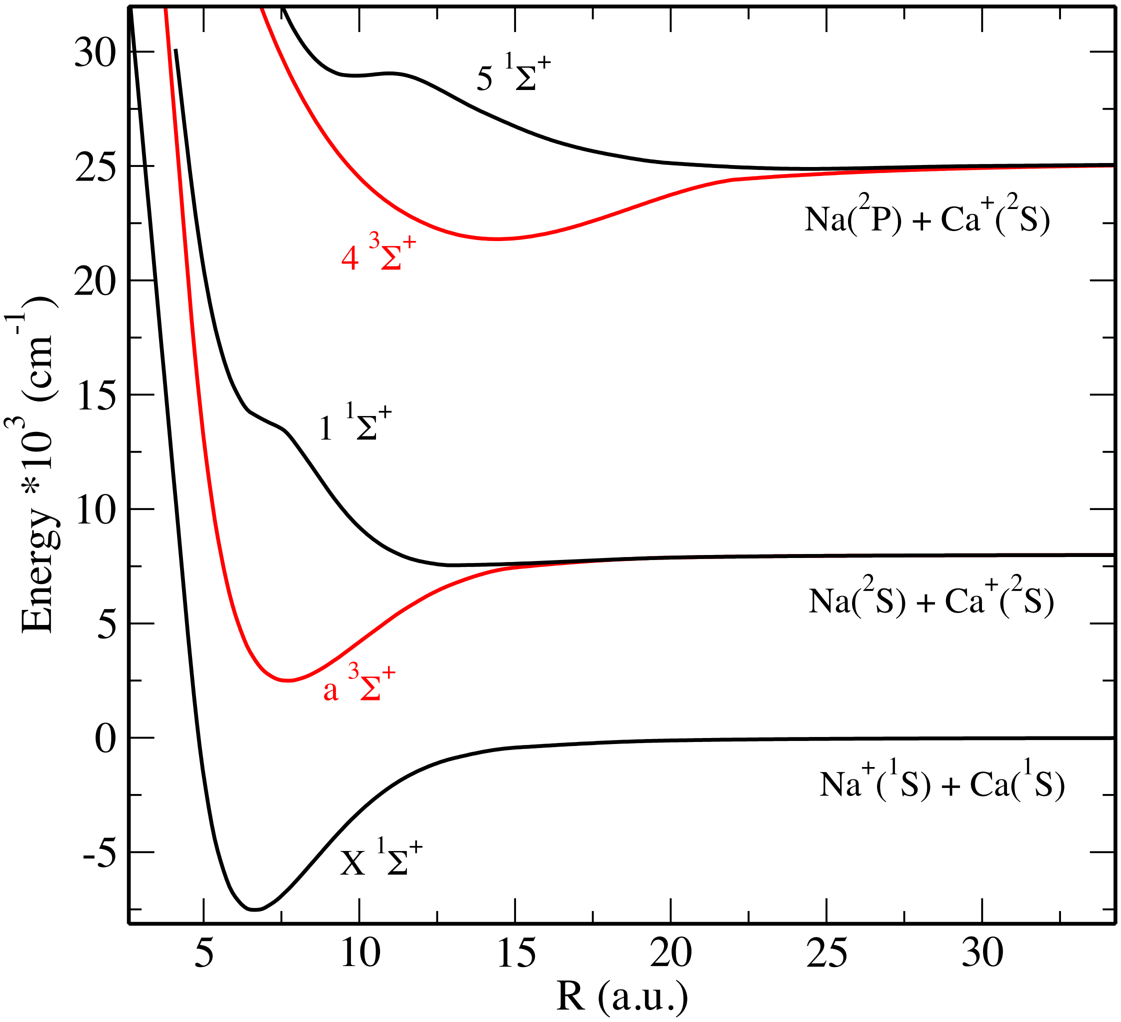

Figure 6.1. *Ab initio* potential energy curves for the low lying singlet and triplet states of NaCa$^+$.

6.3 Hyperfine spectra of NaCa$^+$ in the X$^1\Sigma^+$ state

Over the past few years, there has been a lot of advancement in the experimental methods to form the lowest rovibrational ground state of alkali dimers at ultracold temperatures. Methods ranged from direct photoassociation [83] to stimulated Raman adiabatic passage [84]. Owing to the richer manifold of states in mixed alkali alkaline systems, hybrid ion traps and experiments to study cold collisions in NaCa$^+$ system were proposed at UCONN [85, 86]. Resonant charge transfer and collisional studies with the cold atom/ion pair were studied.

One of the goals of the such experiments is to form a stable molecular quantum gas. In order to do that, one would require to produce a large number of molecules at ultracold temperatures in the same hyperfine level. Thus, one would require the knowledge of the hyperfine structure arising from the nuclear spin and electric quadrupoles of the constituent atom/ions. Another important application of preparing a molecule in a particular state is the ability to have an extreme state selectively. Such highly selective states do not suffer from any perturbation from nearby states, and thus are very good candidates for quantum computation.

6.3.1 Hyperfine Hamiltonian

For a molecular ion in a $^1\Sigma^+$ state, the total Hamiltonian of the system in an external magnetic field can be written as [87, 88]

$$H_{tot} = H_{rot} + H_{hfs} + H_{zee} , \tag{6.1}$$

where

$$H_{rot} = B_v N^2 - D_v N^4 \,, \tag{6.2}$$

$$\begin{aligned} H_{hfs} &= H_Q + H_{sr} + H_t + H_{ss} \\ &= \sum_{i=1}^{2} \boldsymbol{V_i} \cdot \boldsymbol{Q_i} + \sum_{i=1}^{2} \boldsymbol{c_i} \cdot \boldsymbol{N} \cdot \boldsymbol{I_i} + c_3 \boldsymbol{I_1} \cdot \boldsymbol{T} \cdot \boldsymbol{I_2} + c_4 \boldsymbol{I_1} \cdot \boldsymbol{I_2} \,, \end{aligned} \tag{6.3}$$

and

$$H_{zee} = -g_r \mu_N \boldsymbol{N} \cdot \boldsymbol{B} - \sum_{i=1}^{2} g_i \mu_N \boldsymbol{I_i} \cdot \boldsymbol{B} (1 - \sigma_i) \,. \tag{6.4}$$

Here, the dummy index i refers to each nuclei of the diatomic molecular ion while $\boldsymbol{I_1}$ and $\boldsymbol{I_2}$ refer to the nuclear spins of atom 1 and 2, respectively.

The first term of the total Hamiltonian given by Eq. (6.2) consists of the rotational part. The rotational and centrifugal constants of the molecule are given by B_v and D_v respectively (we neglect the centrifugal distortion in this work). We note that the rotational quantum operator is denoted by $\boldsymbol{N}$, we reserve $\boldsymbol{J}$ for denoting the angular momentum including electron spin for triplet states, as is discussed in the following section.

The hyperfine Hamiltonian given by Eq. (6.3) consists of four parts. The first term represents the interaction of electric quadrupole of the nuclei and the electric field gradients created by the electrons, eqQ_1 and eqQ_2. The second is the spin-rotation term, which describes the interaction of the nuclear spin with the magnetic moment created by the rotation of the molecule. Its coupling constants are c_1 and c_2. The last two terms represent the interaction between the two nuclear spins $\boldsymbol{I_1}$ and $\boldsymbol{I_2}$; there is both a tensor component, with coupling constant c_3, and a scalar component, with coupling constant c_4. The tensor $\boldsymbol{T}$ represents the angular part of a dipole-dipole interaction.

The Zeeman Hamiltonian given by Eq. (6.4) consists of two contributions from rotational and nuclear Zeeman terms. The rotational g-factor is denoted by g_r, whereas the nuclear g-factors corresponding to the two nuclei are given by g_1 and g_2, respectively. σ_i represents the isotropic nuclear shielding for atom i.

6.3.2 Coupling coefficients and Matrix elements

In this section, we discuss the calculation of coupling coefficients defined in the previous section, and also look at the matrix elements for the various terms in the hyperfine Hamiltonian. We use *ab initio* methods to calculate the hyperfine coupling constants. Density functional theory (DFT) is used with all-electron def2-QZVPPD basis sets, in the `GAUSSIAN` program to calculate all of the coefficients, except the rotational g-constant for which the `DALTON` program was used. The sample input files for these calculations are provided in Appendix D.1. Table 6.2 lists the calculated values of the coupling constants for X $^1\Sigma^+$ state of ^{23}Na^{43}Ca$^+$ at equilibrium internuclear separation r_e= 3.43 Å.

The hyperfine energy levels are obtained by diagonalizing the matrix representation of the Hamiltonian (see Eq. (6.1)) in a suitable basis set of angular momentum functions. We discuss the matrix elements of the different terms in the Hamiltonian given by Eq. (6.1). Detailed derivations of all these matrix elements have been done in standard texts [89, 90]. The matrix elements of the rotational Hamiltonian (H$_{rot}$) is given by,

Table 6.2. Hyperfine coupling coefficients for ^{23}Na^{43}Ca^{+}. $I_1 = 3/2$ and $I_2 = 7/2$ for ^{23}Na and ^{43}Ca atoms respectively.

Terms	Coupling coefficients
eqQ_1 (MHz)	-1.843
eqQ_2 (MHz)	0.015
c_1 (Hz)	378.901
c_2 (Hz)	-523.270
c_3 (Hz)	-272.936
c_4 (Hz)	-670.252
g_r	0.010
σ_1 (ppm)	591.373
σ_2 (ppm)	1335.627

$$\begin{aligned}\langle H_{rot}\rangle &= \langle N, m_N, m_1, m_2|H_{rot}|N', m'_N, m'_1, m'_2\rangle \\ &= B_v N(N+1)\delta_{N,N'}\delta_{m_1,m'_1}\delta_{m_2,m'_2}\,. \end{aligned} \tag{6.5}$$

We now list down the matrix elements of the four contributions in the hyperfine Hamiltonian. The first contribution is the electric quadrupole term. For a heteronuclear diatomic molecule, there are two distinct terms due to the electric quadrupole moment of the two nuclei. We shall only list the matrix element for one of the them (say atom 1), since the other term (for atom 2) would be exactly similar. The matrix element for the quadrupole Hamiltonian H_Q is given by,

$$
\begin{aligned}
\langle H_Q^{(1)}\rangle &= \langle i_2, m_2, (i_1 N)F_1, m_{F_1}|\boldsymbol{V_1^{(1)}}\cdot\boldsymbol{Q_1^{(2)}}|i_2, m_2', (i_1, N')F_1', m_{F_1}'\rangle \\
&= \delta_{F_1,F_1'}\delta_{m_{F_1},m_{F_1'}}\delta_{m_2,m_2'}(-1)^{N+N'+i_1+F_2} \\
&\times \frac{eqQ_1}{4}[(2N+1)(2N'+1)]^{1/2} \\
&\times \begin{pmatrix} N & 2 & N' \\ 0 & 0 & 0 \end{pmatrix}\begin{pmatrix} i_1 & 2 & i_1 \\ -i_1 & 0 & i_1 \end{pmatrix}^{-1}\begin{Bmatrix} N & i_1 & F_1 \\ i_1 & N' & 2 \end{Bmatrix}. \qquad (6.6)
\end{aligned}
$$

The matrix element for spin-rotation Hamiltonian H_{sr} is given by,

$$
\begin{aligned}
\langle H_{sr}^{(1)}\rangle &= \langle i_2, m_2, (i_1 N)F_1, m_{F_1}|H_{sr}^{(1)}|i_2, m_2', (i_1, N')F_1', m_{F_1}'\rangle \\
&= \delta_{m_2,m_2'}\delta_{N,N'}\delta_{F_1,F_1'}\delta_{m_{F_1},m_{F_1'}} \\
&\times \frac{1}{2}c_1(F_1(F_1+1)-i_1(i_1+1)-N(N+1)). \qquad (6.7)
\end{aligned}
$$

The matrix element for tensorial spin-spin interaction H_t is given by,

$$
\begin{aligned}
\langle H_t\rangle &= \langle N, (i_1, i_2)I, F, m_{F_1}|H_t|N', (i_1, i_2)I', F', m_{F_1'}\rangle \\
&= c_3\sqrt{30}\delta_{F,F'}\delta_{m_F,m_F'}(-1)^{N'+N+I+F} \\
&\times i_1(i_1+1)(2i_2+1)[(2N+1)(2N'+1)(2I+1)(2I'+1)]^{1/2} \\
&\times \begin{pmatrix} N & 2 & N' \\ 0 & 0 & 0 \end{pmatrix}\begin{Bmatrix} N & I & F \\ I' & N' & 2 \end{Bmatrix}\begin{Bmatrix} i_1 & i_2 & 1 \\ i_1 & i_2 & 1 \\ I & I' & 2 \end{Bmatrix}. \qquad (6.8)
\end{aligned}
$$

Finally, the last term in the hyperfine Hamiltonian is the scalar spin-spin interaction H_{ss}, whose matrix element is given by,

$$
\begin{aligned}
\langle H_{ss}\rangle &= \langle N, (i_1, i_2)I, F, m_F|H_t|N', (i_1, i_2)I', F', m_{F'}\rangle \\
&= \delta_{N,N'}\delta_{I,I'}\delta_{F,F'}\delta_{m_F,m_F'} \\
&\times \frac{1}{2}c_4(I(I+1)-i_1(i_1+1)-i_2(i_2+1)). \qquad (6.9)
\end{aligned}
$$

Now we are left with the evaluation of the matrix element of the Zeeman Hamiltonian (see Eq. (6.4)), which consists of the nuclear Zeeman and the rotational Zeeman terms.

$$\begin{aligned}\langle H_{NZ}\rangle &= \langle N, m_N, m_1, m_2|H_{NZ}|N', m'_N, m'_1, m'_2\rangle \\ &\times \delta_{N,N'}\delta_{m_N,m'_N}\delta_{m_1,m'_1}\delta_{m_2,m'_2} \\ &\times -m_N B_z g_r \mu_N\,, \qquad (6.10)\end{aligned}$$

and

$$\begin{aligned}\langle H^i_{IZ}\rangle &= \langle N, m_N, m_1, m_2|H_{NZ}|N', m'_N, m'_1, m'_2\rangle \\ &\times \delta_{N,N'}\delta_{m_N,m'_N}\delta_{m_1,m'_1}\delta_{m_2,m'_2} \\ &\times -m_i B_z g_i \mu_N(1-\sigma_i)\,. \qquad (6.11)\end{aligned}$$

6.3.3 Magnetic Hyperfine Spectra

We show in Fig. 6.2 the magnetic hyperfine spectra of the X $^1\Sigma^+$ state for ^{23}Na^{43}Ca$^+$ molecular ion. Each state with a total angular momentum F splits into $(2F+1)$ values in the presence of a magnetic field. Since ^{43}Ca isotope has a negative magnetic moment, it gives rise to an inverted hyperfine spectra. The zero field splitting is $\sim$ few kHz, similar to most X $^1\Sigma^+$ splitting for other heteronuclear alkali species [88].

However, as mentioned previously, we would like to take advantage of the zero nuclear spin of the ^{40}Ca isotope. Fig. 6.3 shows the hyperfine spectra of the X $^1\Sigma^+$ state for ^{23}Na^{40}Ca$^+$ ionic dimer. The only angular momentum involved in this system, is the nuclear spin of the ^{23}Na atom of 3/2. Hence, there is no zero-field splitting, however with the non-zero value of magnetic field, the single hyperfine level splits into 4 distinct widely separated Zeeman states. The hyperfine spectra of the X $^1\Sigma^+$ state for $N = 1$, for both ^{23}Na^{43}Ca$^+$ and ^{23}Na^{40}Ca$^+$ are shown in Appendix D.3.

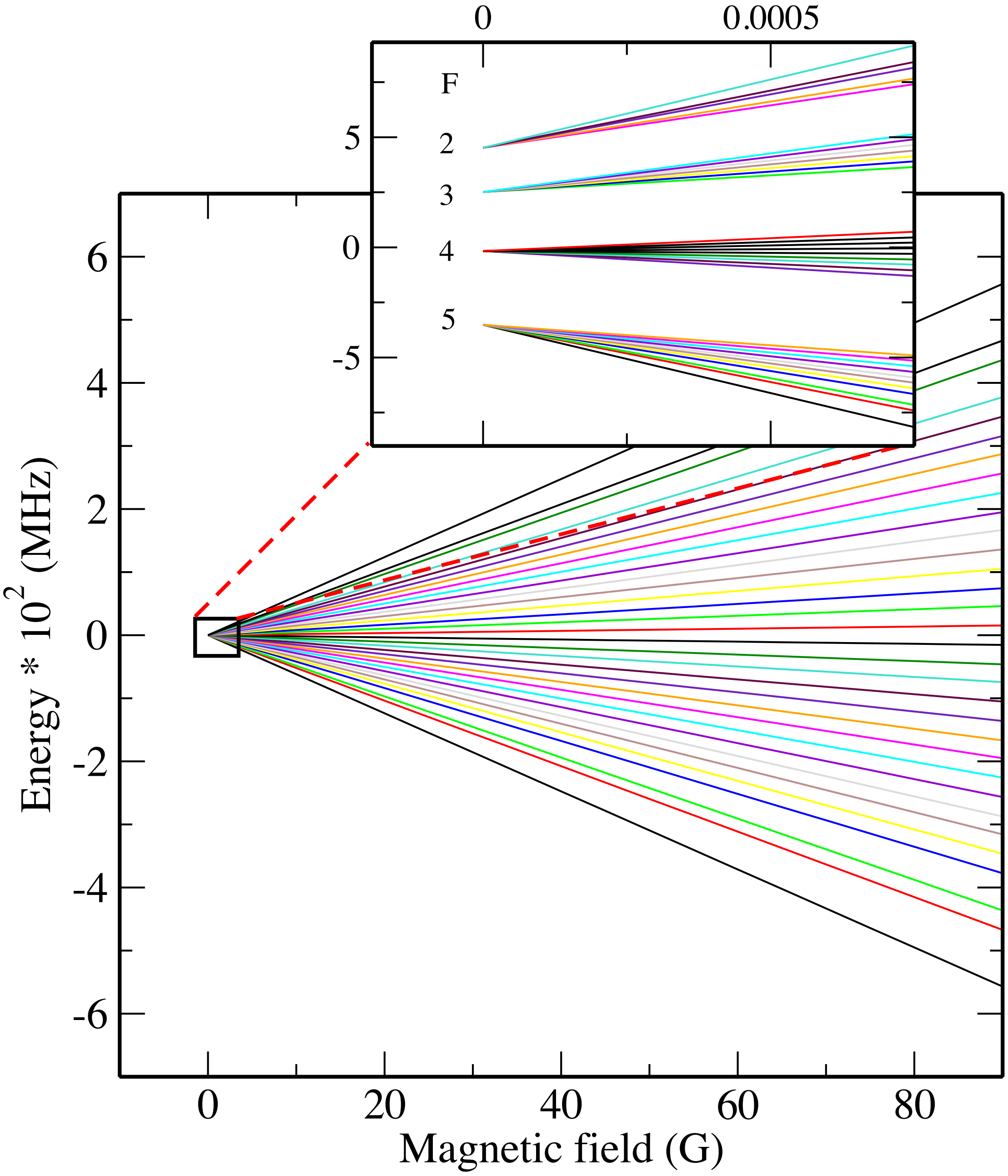

Figure 6.2. The figure shows the magnetic hyperfine spectrum of ^{23}Na^{43}Ca$^+$ in its ground X $^1\Sigma^+$ state at equilibrium internuclear separation. The inset is a magnification of the zero-field splitting, the energy scale (on Y-axis) being in kHz, and the X-axis reads the magnetic field in Gauss.

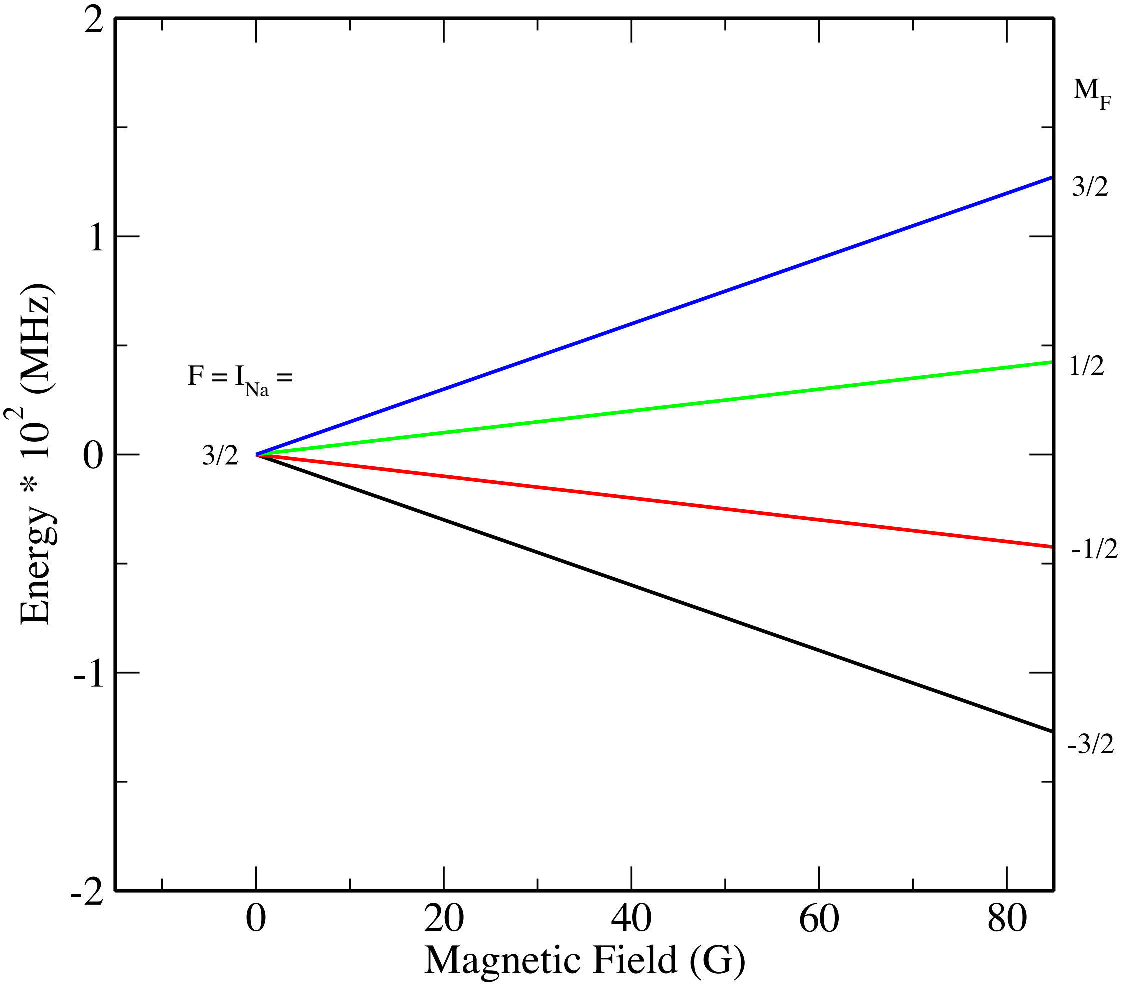

Figure 6.3. The figure shows the magnetic hyperfine spectrum of ^{23}Na^{40}Ca$^+$ in its ground X $^1\Sigma^+$ state at equilibrium internuclear separation. Note that, owing to ^{40}Ca having no nuclear spin there is no zero-field splitting in the singlet state.

6.4 Hyperfine spectra of NaCa$^+$ in the a$^3\Sigma^+$ state

In the previous section, we have discussed about the hyperfine spectra of the NaCa$^+$ molecular ion in the ground X$^1\Sigma^+$ state at equilibrium internuclear separation. Although the singlet ground state is the most stable configuration of the system, recently there is a lot of interest in the hyperfine spectra of the triplet states.

As we have seen in the previous section, the hyperfine spectra becomes much more cleaner and simpler when we use the ^{40}Ca isotope with zero nuclear spin instead of the ^{43}Ca isotope with a nuclear spin of 7/2. This becomes even more crucial, when aside from a nuclear spin, there is present a non-zero electronic spin $S = 1$ for the a$^3\Sigma^+$ state. It is for this reason that we limit our discussion of triplet hyperfine spectra to the ^{40}Ca isotope.

The simplest way to quantify the various calculations of the hyperfine spectra is to use the Hund's case (b) notation and use the following angular momentum coupling scheme. The individual nuclear spins $\boldsymbol{I_1}$ and $\boldsymbol{I_2}$ couple to form total nuclear spin $\boldsymbol{I}$. Now because of the non-zero electronic spin $\boldsymbol{S}$, the rotational angular momentum $\boldsymbol{N}$ couples with $\boldsymbol{S}$ to form total angular momentum $\boldsymbol{J}$, $\boldsymbol{N}+\boldsymbol{S}=\boldsymbol{J}$. In the next step, $\boldsymbol{J}$ couples with total nuclear spin $\boldsymbol{I}$ to form the grand total angular momentum $\boldsymbol{F}$: $\boldsymbol{J}+\boldsymbol{I}=\boldsymbol{F}$. In the presence of magnetic field, this hyperfine level F splits into an additional $(2F + 1)$ energy levels, giving the magnetic hyperfine spectra.

6.4.1 Hyperfine Hamiltonian – additional terms

There are additional terms in the Hamiltonian arising from the non-zero electronic spin $\boldsymbol{S}$. The total Hamiltonian of the system can still be written in the form of Eq.

(6.1). There are two additional terms in the hyperfine Hamiltonian which can be written as

$$\begin{aligned} H_{hfs}^{more} &= H_R + H_{FC} \\ &= \gamma_e \boldsymbol{N} \cdot \boldsymbol{S} + b_F \boldsymbol{I} \cdot \boldsymbol{S} \,. \end{aligned} \tag{6.12}$$

The first term in Eq. (6.12) H_R denotes the electronic spin-rotation term with a coupling coefficient γ_e. The second term H_{FC} signifies the interaction of this non-zero electronic spin $\boldsymbol{S}$ with the nuclear spin $\boldsymbol{I}$ of the molecular ion; this is the Fermi-contact interaction term with coupling coefficient b_F.

The next term in the Hamiltonian is the Zeeman term (Eq. 6.4) which needs to be modified to include the interaction of electronic spin $\boldsymbol{S}$ with the external magnetic field $\boldsymbol{B}$

$$H_{zee}^{more} = -g_s \mu_B \boldsymbol{S} \cdot \boldsymbol{B} \,. \tag{6.13}$$

6.4.2 Coupling coefficients and Matrix elements

As discussed for the ${}^1\Sigma^+$ state, all coupling coefficients were calculated with *ab initio* methods. Table 6.3 lists the required hyperfine coupling coefficients for ${}^{23}\mathrm{Na}^{40}\mathrm{Ca}^+$ in the $\mathrm{a}^3\Sigma^+$ state at $r_e = 4.05$ Å. Note that the triplet state is somewhat extended as is seen from the larger r_e. For calculation of the matrix elements and notations for angular momentum algebra and basis functions we refer to Carrington and Brown's textbook [89]. The matrix element for electronic spin-rotation Hamiltonian becomes

$$\begin{aligned} \langle H_R \rangle &= \langle N, S, J, m_J | H_R | N, S, J, m_J \rangle \\ &= \gamma_e (-1)^{N+J+S} \begin{Bmatrix} S & N & J \\ N & S & 1 \end{Bmatrix} \\ &\times \; (N(N+1)(2N+1)S(S+1)(2S+1))^{1/2} \,. \end{aligned} \tag{6.14}$$

The matrix element for Fermi-contact interaction is given by

$$\begin{aligned}
\langle H_{FC}\rangle &= \langle N,S,J,I,F,m_F|b_F\boldsymbol{I}\cdot\boldsymbol{S}|N,S,J',I,F',m'_F\rangle \\
&= b_F\delta_{m_Fm'_F}\delta_{FF'}(-1)^{J'+F+I}((2J+1)(2J'+1))^{1/2} \\
&\times\ (-1)^{J+N+1+S}(S(S+1)(2S+1)I(I+1)(2I+1))^{1/2} \\
&\times\ \begin{Bmatrix} I & J' & F \\ J & I & 1 \end{Bmatrix}\begin{Bmatrix} J & S & N \\ S & J' & 1 \end{Bmatrix}. \qquad (6.15)
\end{aligned}$$

The matrix element for the magnetic Zeeman term coupling the electronic spin $\boldsymbol{S}$ is given by

$$\begin{aligned}
\langle H^S_{Zee}\rangle &= \langle N,S,J,I,F,m_F|H^S_{Zee}|N,S,J',I,F',m_F\rangle \\
&= -g_S\mu_BB_z(-1)^{F-m_F}((2F+1)(2F'+1))^{1/2} \\
&\times\ (-1)^{F'+J+1+I}((2J+1)(2J'+1))^{1/2} \\
&\times\ (-1)^{J+N+1+S}(S(S+1)(2S+1))^{1/2} \\
&\times\ \begin{pmatrix} F & 1 & F' \\ -m_F & 0 & m_F \end{pmatrix}\begin{Bmatrix} F & J & I \\ J' & F' & 1 \end{Bmatrix}\begin{Bmatrix} J & S & N \\ S & J' & 1 \end{Bmatrix}. \qquad (6.16)
\end{aligned}$$

Table 6.3. Hyperfine coupling coefficients for the $a^3\Sigma^+$ state of ^{23}Na^{40}Ca$^+$ at $r_e =$ 4.05Å. $I_1 = 3/2$ and $I_2 = 0$ for ^{23}Na and ^{40}Ca atoms respectively. Note that nuclear spin-spin interaction terms are absent, since they are zero identically.

Terms	Coupling coefficients
eqQ_1 (MHz)	-1.104
c_1 (Hz)	378.901
γ_e (MHz)	27.856
b_F (MHz)	326.001
g_r	0.010
σ_1 (ppm)	624.331
σ_2 (ppm)	458.733

6.4.3 Magnetic Hyperfine Spectra

Fig. 6.4 shows the magnetic hyperfine spectrum of ^{23}Na^{40}Ca$^+$ in its ground a $^3\Sigma^+$ state at its equilibrium internuclear separation, r_e=4.05 Å. Since for the a $^3\Sigma^+$ state, the electronic spin is non-zero, S=1, this couples with the nuclear spin of ^{23}Na to produce the magnetic hyperfine structure. As mentioned previously in this chapter, this coupling is precisely the reason for choosing the mixed alkali alkaline-earth species to explore the hyperfine structure. The very interesting hyperfine map of the triplet state would help to prepare a pure quantum state in its fully stretched hyperfine state $|F, M_F\rangle = |5/2, 5/2\rangle$.

The strongest coupling governing the zero-field splitting is the Fermi-Contact interaction term, which in the case of ^{23}Na^{40}Ca$^+$ is about few hundred MHz. Each hyperfine level corresponding to a particular value of F, splits into $(2F + 1)$ values in the presence of external magnetic field B. At low enough magnetic field of < 100 G, the splitting between two successive hyperfine levels is ~ 50 MHz, which is large

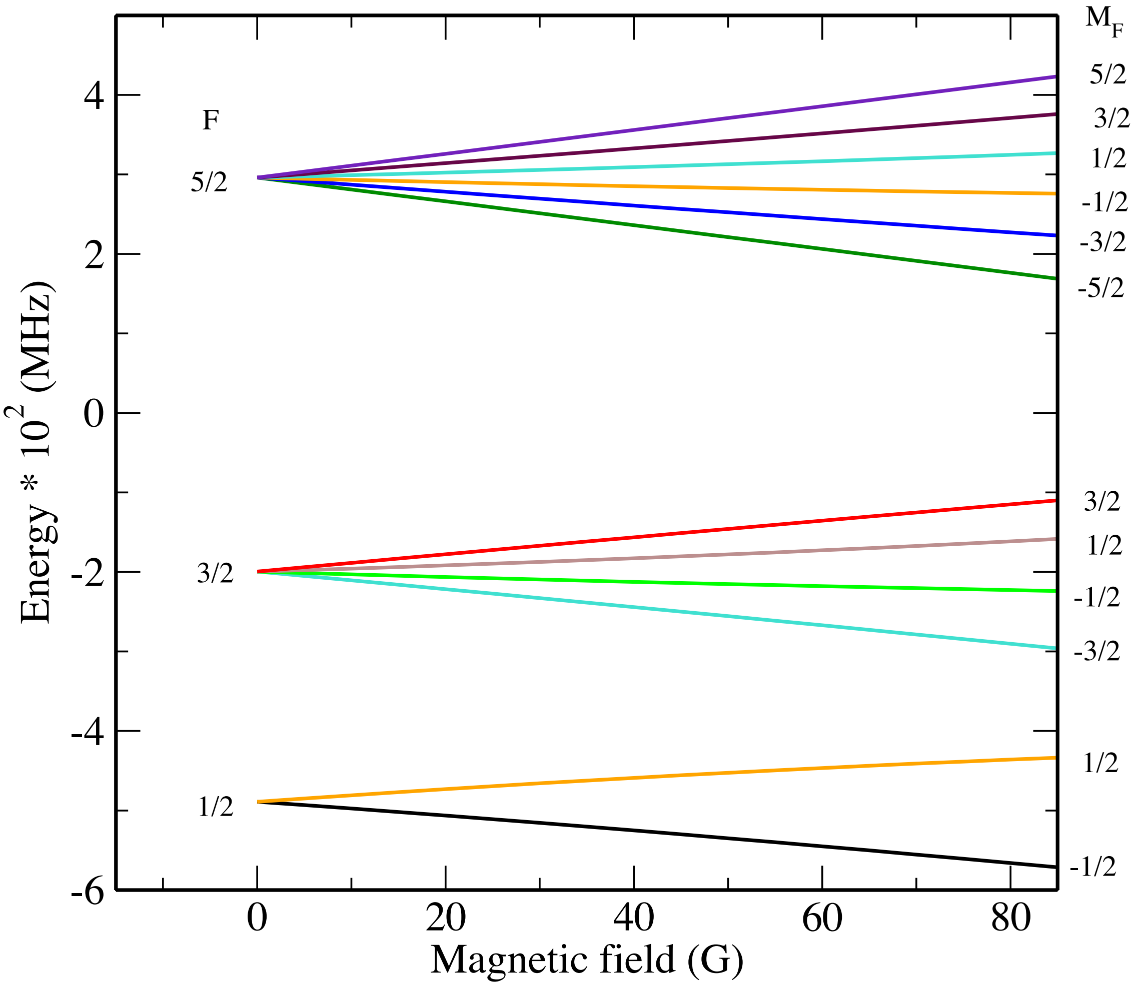

Figure 6.4. The figure shows the magnetic hyperfine spectrum of ^{23}Na^{40}Ca^{+} in its ground a $^{3}\Sigma^{+}$ state at equilibrium internuclear separation. Note that the electronic spin of ^{40}Ca couples to the nuclear spin of ^{23}Na to produce a simple and clean hyperfine map, with the zero-field splitting governed by the Fermi-Contact interaction.

enough to be easily resolved experimentally.

6.5 Concluding Remarks

In this chapter, we have developed a fully quantum mechanical treatment of the hyperfine structure in the lowest singlet and triplet states of NaCa$^+$. We believe the accurate knowledge of the hyperfine spectrum in such species, would pave the path for engineering pure quantum states using ultracold molecular ions.

It has been demonstrated that owing to the intricate angular momentum coupling, the hyperfine spectra is very complex. In problems as demanding as this, there is always space for further improvements and developments based on the ground work that has already been laid down. We have calculated the hyperfine spectrum for the equilibrium inter-nuclear separations for all the systems described above. The next important aspect to study would be to analyze such a spectrum with the change of the inter-nuclear separation R, along the potential energy surface of the system. This would lead to modified potential energy curves for a particular system in presence of an external magnetic field. Further calculations in this direction are currently underway in our group in the case of mixed alkali alkaline-earth systems.

Chapter 7

Electronic structure calculations in polyatomic molecular ions – Gold Nanoclusters

7.1 Introduction and Overview

Until now, we have discussed electronic structure calculations in diatomic molecular ions, mostly in the alkaline-earth family. In this chapter, we extend our discussion to the study of polyatomic systems – gold nanoclusters. The jump from diatomic to polyatomic systems is not straight-forward, and one often has to undertake many approximations to simplify the quantum mechanical problem. One such approximation is the exclusion of certain parts of the structure, and qualitatively describe it with classical mechanics, while treating other regions of interest quantum mechanically. Owing to many bond lengths, and hence many more degrees of freedom a discussion of potential energy curves is deliberately omitted. Instead the quality of the calculated structure is compared with the experimental X-Ray structure. Local properties, such as NMR shieldings, are also calculated by *ab initio* methods. The choice of gold nanoclusters as our system of interest was guided by several interests and applications in both physics and chemistry.

It is well known that gold nanoparticles are capable of catalyzing a number of fundamental chemical reactions [91, 92, 93]. Tunable reactions in metallic nanoparticles can be obtained by encapsulation of nanocrystals in thiolated monolayers [94, 95] known as monolayer protected clusters (MPCs). Exploiting MPCs for applications in the area of catalysis requires a proper structural and dynamical characterization of the physical properties of the protecting layer. It was not until recently, that such requisite has been met by the total structure determination of a number of thiolated gold clusters [96, 97, 98]. Such structures are characterized by surface gold atoms in the so called "staple" (–S–Au–S–) or "V-shape" motifs (–S–Au–S–Au–S–), as opposed to commonly assumed structures in which thiolates only passivate a high symmetry gold cluster. Along these experimental studies, Density Functional Theory has been crucial to interpret structural data under the light of NMR spectroscopy [99, 100], optical absorption [101], and electrochemical experiments [102]. Due to the size of these clusters, augmented by thiolated ligands, theoretical characterization (e.g calculation of spectra) requires an enormous amount of computational resources (both in time and memory). Intrinsic limitations of current Quantum Chemistry software places these types of calculations at the limits of computational tractability. This is clearly the case if, in addition to quantum detail, finite temperature simulations are required. In fact, a number of studies have shown a marked dependence of optical and electrochemical properties on temperature [103, 104, 105]. Thus, to retain quantum detail and incorporate finite temperature motions it would certainly be advantageous to develop approaches that can combine these features with a reasonable computational cost.

Empirical potentials have been used in the past for gold clusters to search structural minima followed by quantum mechanical refinement [106], but little has been done in the context of MPC's, especially considering the recent re-evaluation of the sulfur-gold binding motifs. Another approach would be to develop hybrid methods such as QM/MM, which were originally developed in the context of enzyme reactions

[107]. In this work we develop MM and QM/MM models, explore different implementations, and evaluate their ability to reproduce experimental data. We envision that such approaches will be of value to enable, in a practical manner, sampling of a large number of monolayer conformations. In particular, such procedures will be relevant to describe highly interacting oligopeptide ligands [108, 99]. In addition, partitioning the system into a QM and MM region will lead to several advantages. Apart from the obvious computational benefits, such method opens up a wide range of possibilities for certain studies of similar systems for which a full QM description is impractical and often unnecessary. This new approach also opens the possibility of focusing strictly on the electronic structure of the monolayer alone (or of the gold cluster and a fraction of the monolayer) which, for instance, can be advantageous to obtain insight into catalytic properties of these MPC's[109]. Thus, the goal of this study is to develop a first generation of hybrid methods that can both decrease the computational cost and, at the same time, reproduce the intricacies of the various gold-sulfur surface motifs.

We use $[\mathrm{Au}_{25}(\mathrm{SCH}_3)_{18}]^-$ molecular ion as the central prototype model and extend our theory to explain structural and chemical properties of larger MPC's. We begin by determining a minimum set of parameters and functional forms that would be sufficient to describe a thiol-protected gold cluster via a Molecular Mechanics (MM) force field. We then use these parameters to develop a hybrid QM/MM model which treats regions of chemical interest at a DFT level of theory, keeping all other atoms in the cluster at the MM level.

7.2 Computational Methods

We propose the use of hybrid QM/MM models to study physical and chemical properties of monolayer protected gold clusters. Au-SCH_3, Au-(SCH_3)-Au, and $[Au_{25}$-$(SCH_3)_{18}]^-$ are used as the training systems. In the following sections, we present the parameters and functions necessary to describe the structure in a molecular mechanics (MM) framework. We continue our discussion by introducing QM/MM hybrid models to predict or refine structures and NMR properties of similar gold clusters. All QM/MM calculations were performed with the Gaussian 09 suite [110] using the two-layer ONIOM scheme [111, 112]. In this scheme, the entire system is divided into two regions (X and Y). The QM/MM energy is obtained via an extrapolation of three independent calculations:

$$E = E(QM)_X + E(MM)_{X+Y} - E(MM)_X \tag{7.1}$$

where $E(QM)_X$ is the energy of region X at the QM level, $E(MM)_{X+Y}$ is the energy of the entire system (X and Y) at the MM level, and $E(MM)_X$ is the energy of X at the MM level. In the so called "electronic embedding" (EE) approach, electrostatic interactions between X and Y are included in each of the terms of the right hand side of Eq. 7.1, so that electrostatic interactions are canceled out at the MM level, but remain at the QM level. In the "mechanical embedding" (ME) approach, electrostatic interactions between region X and Y are only included at the MM level (the last two terms of Eq. 7.1). In both EE and ME, Van der Waals (VDW) interactions between X and Y are considered at the MM level (in the term $E(MM)_{X+Y}$). All calculations presented here make use of the EE approximation.

7.2.1 Molecular Mechanics Model

Construction of QM/MM models was made under the assumption that even a pure MM force field description of the thiolated clusters should reproduce the experimental structural data, at least in a qualitative and semi-quantitative manner. To this end, we sought to develop a force field with a minimal set of parameters and functional forms. Derivation of the force field was guided by the notion that these clusters present two well defined domains. Domain **1** contains the inner core (i.e. 13 Au atoms for $Au_{25}(SCH_2\text{-}R)_{18}$ and 23 Au atoms for $Au_{38}(SCH_2\text{-}R)_{24}$) forming high symmetry packed structures. For this domain we defined a 6-12 Lennard-Jones potential as implemented in the Amber force field [113]. Domain **2** contains the thiolated ligands and all Au atoms involved in the V-shape or staple motifs (Fig. 7.1). All gold atoms in this domain are assigned the same force field atom type (AuS). As starting values we took those reported in the UFF force field of Rappé *et al* [114]. These parameters were modified systematically and stepwise until the geometry of $[Au_{25}(SCH_3)_{18}]^{-1}$ was reproduced within a tolerance of 0.2 Å in the root mean square deviation. Gold atoms in **1** are separated from those that are only bonded to other core atoms (type Au) and those that are connected to core atoms and sulfur atoms (type AuC). Although the VDW parameters are identical for these two types, this distinction is required for the definition of bonded parameters (vide infra). VDW parameters are reported in Table 7.1.

Electrostatic interactions between the ligands and gold atoms in domain **1** are assumed to be negligible. Support for this assumption is given by a Bader charge analysis [115, 116] of $[Au_{25}(SCH_3)_{18}]^{-1}$ which shows that charges in domain **1** are very small ($\approx -0.04e$ for the central core atom and $\approx 0.02e$ for the other core atoms), adding up to a total charge of $0.15e$. Bader charges for AuS atoms are also small

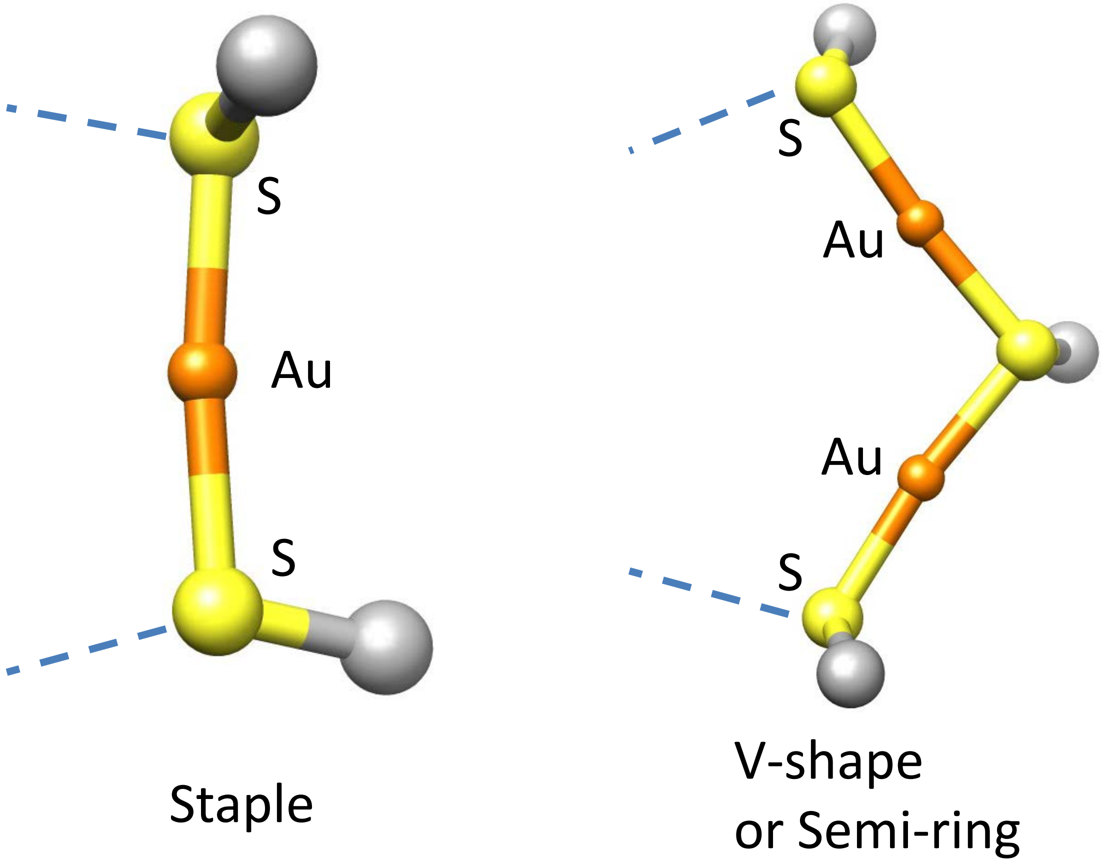

Figure 7.1. Possible binding patterns between gold and thiolated ligands

Table 7.1. 6-12 Lennard Jones parameters for a general MPC. Partial charges correspond to thiol in $[Au_{25}(SCH_3)_{18}]^{-1}$

Atom	Atom-type	σ	ϵ	charge
Au	Au	1.5000	1.0000	0.00000
Au	AuC	1.5000	1.0000	0.00000
Au	AuS	1.9000	1.0000	0.00000
S	SS	2.0000	0.2500	-0.22417
S	SC	2.0000	0.2500	-0.22417
C	CT	1.9080	0.1094	-0.15441
H	H1	1.3870	0.0157	0.10767

Table 7.2. Stretching parameters corresponding to the force field formula $(1/2)k_e(r-r_{eq})^2$.

At-type1	At-type2	k$_r$	r$_{eq}$
AuC	SC	150.00	2.48
AuS	SC	150.00	2.38
AuS	SS	150.00	2.38
SC	CT	237.00	1.84
SS	CT	237.00	1.84
CT	H1	340.00	1.09
CA	H1	340.00	1.09

($\approx 0.04e$). Thus, to facilitate transferability among different core sizes, the charges on all gold atoms are assumed to be zero. Charges on the thiol ligands are taken from an Electrostatic Potential (ESP) analysis (as implemented in Gaussian 09) for the neutral molecule Au_2-$[SCH_3]_2$. This analysis provides the following charges: $q_S = -0.23605$, $q_C = -0.16628$, and $q_H = 0.09580$. To ensure that the total MM charge adds up to the total charge of the cluster (Q), a simple correction δq is applied to each charge via the formula $\delta q = (Q/M - (q_S + q_C + 3q_H))/5$, where M is the number of thiolated ligands. Table 7.1 reports these charges for $Q = -1$ and $M = 18$, which uses the correction $\delta q = 0.01188$.

Bonded parameters (stretching, bending, torsion) involving X-Au-S-X were derived by fitting the force constants in all functional forms to match vibrational frequencies of selected modes of vibration for the molecules Au-SCH_3 and (Au-SCH_3-Au). All other parameters intrinsic to SCH_3 were taken from the Amber force field without modification. Tables 7.2, 7.3, and 7.4 report all bonded parameters involving the newly defined atom types and the existing types in the Amber force field.

Table 7.3. Bending parameters corresponding to the force field formula $(1/2)k_\theta(\theta - \theta_{eq})^2$.

At-type1	At-type2	At-type3	k_θ	θ_{eq}
AuC	SC	CT	35.00	105.00
AuS	SC	CT	35.00	105.00
SC	CT	H1	50.00	109.50
H1	CT	H1	35.00	109.50
SC	AuS	SS	20.00	180.00
AuS	SS	CT	35.00	105.00
AuS	SS	AuS	20.00	100.00
AuC	SC	AuS	20.00	91.00
SS	CT	H1	50.00	109.50
SC	CT	CT	50.00	111.50
SS	CT	CT	50.00	111.50
H1	CT	CA	35.00	110.50
CA	CA	H1	35.00	120.00

Table 7.4. Amber torsional parameters corresponding to the force field formula $\sum_{i=1}^{4} M_i[1 + \cos(i\theta - O_i(i+4))]/N_p$.

At-type1	At-type2	At-type3	At-type4	O_1	O_2	O_3	O_4	M_1	M_2	M_3	M_4	N_p
AuC	SC	CT	H1	0	0	0	0	0.00	0.00	0.16	0.00	1.00
AuC	SC	CA	H1	0	0	0	0	0.00	0.00	0.16	0.00	1.00
AuS	SC	CT	H1	0	0	0	0	0.00	0.00	0.16	0.00	1.00
AuS	SC	CA	H1	0	0	0	0	0.00	0.00	0.16	0.00	1.00
AuS	SS	CT	H1	0	0	0	0	0.00	0.00	0.16	0.00	1.00
AuS	SS	CA	H1	0	0	0	0	0.00	0.00	0.16	0.00	1.00
SC	AuS	SC	CT	0	0	0	0	0.00	0.00	0.00	0.00	1.00
SC	AuS	SC	CA	0	0	0	0	0.00	0.00	0.00	0.00	1.00
SC	AuS	SS	CT	0	0	0	0	0.00	0.00	0.00	0.00	1.00
SC	AuS	SS	CA	0	0	0	0	0.00	0.00	0.00	0.00	1.00
AuS	SS	AuS	SC	0	0	0	0	0.00	0.00	0.00	0.00	1.00
AuC	SC	AuS	SS	0	0	0	0	0.00	0.00	0.00	0.00	1.00
CT	SC	AuS	SS	0	0	0	0	0.00	0.00	0.00	0.00	1.00
CA	SC	AuS	SS	0	0	0	0	0.00	0.00	0.00	0.00	1.00

7.2.2 QM/MM Model

One of the major objectives in developing a full MM force field is to use it as the underlying potential in hybrid QM/MM models. We benchmark our model by comparing structural descriptors in $[Au_{25}(SCH_3)_{18}]^-$. The crystal structure of $[N(C_8H_{17})_4]^+[Au_{25}(SCH_2CH_2Ph)_{18}]^{-1}$ was determined recently by Heaven *et al.* [97], which was followed by several other experimental investigations [117] and theoretical [118] calculations using density functional theory (DFT) methods. The initial geometry for our QM/MM calculations is derived from that crystal structure by replacing the ethylphenyl groups with methyl groups. We adjust the resulting $[Au_{25}(SCH_3)_{18}]^-$ structure to obtain a symmetric structure belonging to the point group C_i.

The $[Au_{25}(SCH_3)_{18}]^-$ structure consists of an icosahedral Au_{13} core, protected by six V-shape motifs in an approximate octahedral arrangement. Each of the S atoms are connected to the organic ligand (CH_3), forming a monolayer protected cluster. We propose a QM/MM model in which the icosahedral Au_{13} core is treated via MM whereas the V-shape motifs with the ligands are treated via QM methods(see figure 7.2). These two regions interact with each other via the ONIOM extrapolation scheme with electronic embedding as described in Eq. 7.1.

Our choice of the partition for $[Au_{25}(SCH_3)_{18}]^-$ cluster was fairly straight-forward, making use of the intuitive definition of domains presented in the previous section. The icosahedral Au_{13} core is very stable and can be accurately described by a Lennard-Jones potential. Each of the gold atoms in the core, except the central one, is bonded to a sulphur atom forming a V-shape motif. A “cut” is defined between atoms types AuC and SC. These bond cuts are implemented in ONIOM by defining a “link-atom” to satisfy the valence and avoid broken bonds. The default choice of such a link-

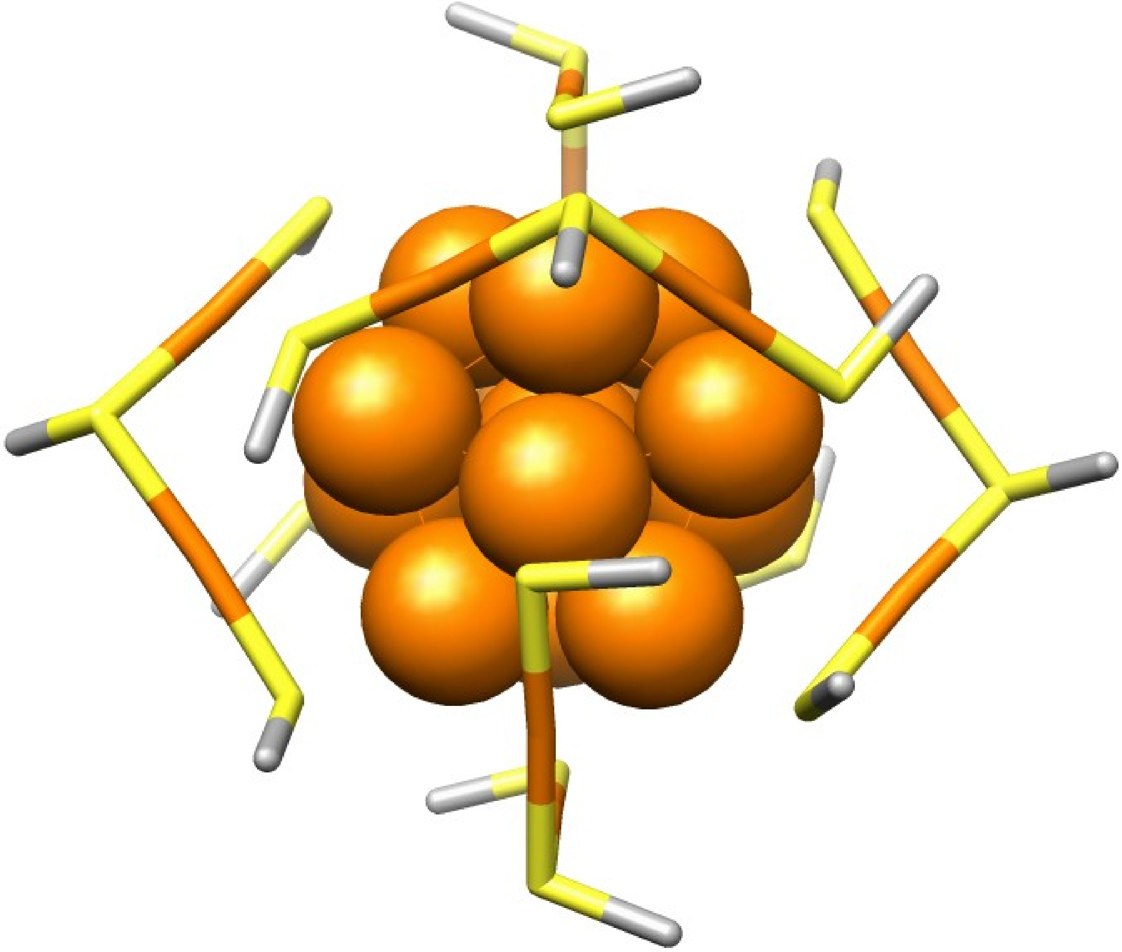

Figure 7.2. Structure of $[Au_{25}(SCH_3)_{18}]^-$, with Au atoms shown in orange, S in yellow, C in gray. H atoms are not shown for clarity. The Au_{13} core (MM region) is shown with spheres while all other atoms (QM region) are shown with sticks.

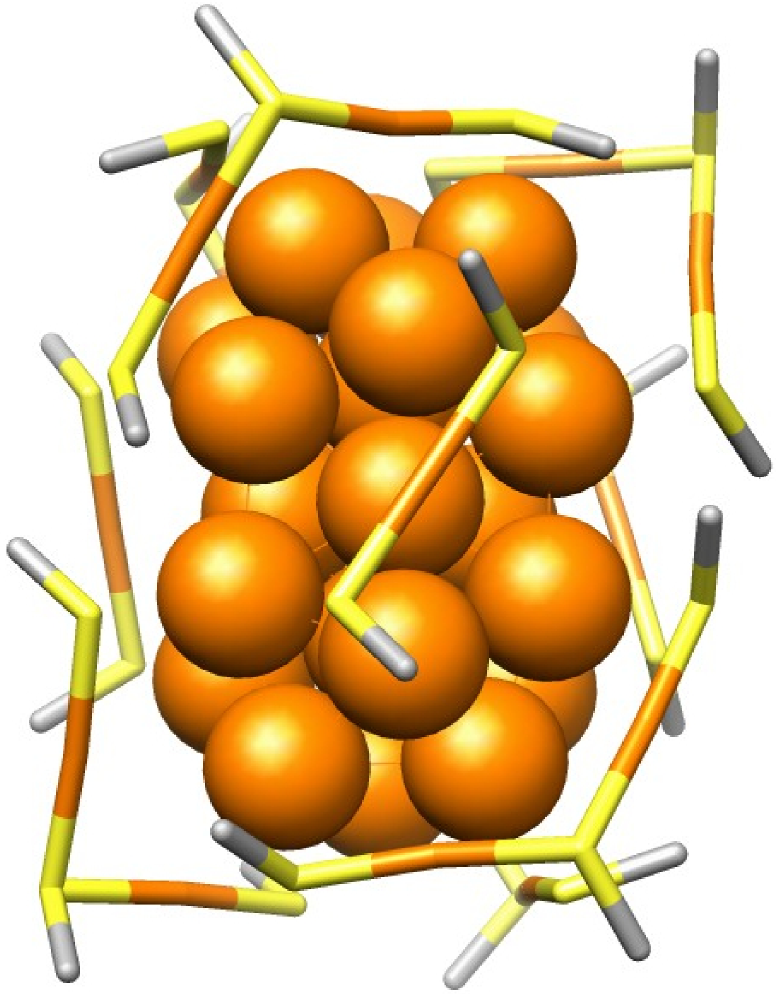

Figure 7.3. Structure of $Au_{38}(SCH_3)_{24}$. The Au_{23} core (MM region) is shown with spheres while all other atoms (QM region) are shown with sticks.

atom is typically a hydrogen atom. However for our purposes, the best choice of link-atom turned out to be another Au atom, thus forming Au(link)–S bonds in place of Au(core)–S bonds. Since the core has a small charge ($\approx 0.15e$), and since the QM region needs to be assigned an integer charge, we assume a –1 charge solely distributed among the atoms of domain **2** (QM region), thus making the entire structure an anion. The force field (based on Amber) described previously was used for the MM region. DFT was used to describe the remaining 102 atoms in domain **2**. We used the LANL2DZ psuedopotential and basis sets as defined in Gaussian 09 with the BLYP functional. For computational efficiency, we use density fitting with the W06 fitting basis [119]. It is evident that for this type of partition the gain in computational time, with respect to a full QM calculation, is minimal, since the QM region has effectively 24 gold atoms. Nevertheless, such partitioning scheme represents a proof of concept and will clearly become computationally more efficient for larger clusters and for cases where a reduced number of ligands are described quantum mechanically.

As a second example, we use our QM/MM model to optimize the structure of $Au_{38}(SCH_3)_{24}$. The X-ray structure was determined recently [120] along with a full DFT comparison [121]. The $Au_{38}(SCH_3)_{24}$ structure has a bi-icosahedral Au_{23} core, consisting of two icosahedral Au_{13} units joined by three shared Au atoms at the center. This core is protected by six long $[(Au)_2(SCH)_3]$ semi-ring (V-shape motifs) and three short $[Au(SCH3)_2]$ semi-rings (staple motifs) (see figure 7.3). The entire structure has D_3 symmetry, the largest Abelian point group being C_2.

By analogy with our partitioning of the $[Au_{25}\ (SCH_3)_{18}]^-$ system, we describe the bi-icosahedral Au_{23} core in $Au_{38}(SCH_3)_{24}$ by our modified Amber force field. The outer shell comprising the V-shape and staple motifs was described quantum mechan-

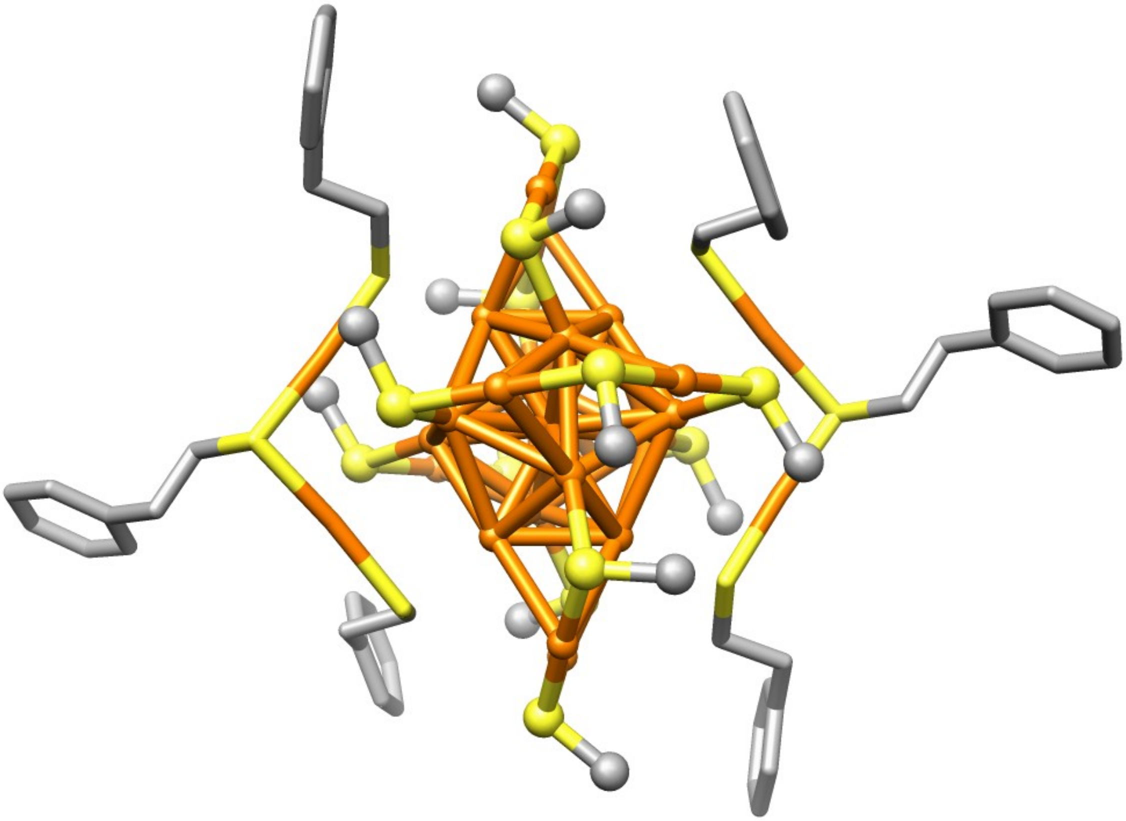

Figure 7.4. Hybrid structure $[Au_{25}(SCH_3)_{12}(SCH_2CH_2\ Ph)_6]^-$. The two semi-rings, belonging to the QM region, have ethyl-phenyls as ligands (shown by sticks). The remaining four semi-rings have methyls, which together with the Au_{13} core belong to the MM region (shown in balls & sticks).

ically using DFT. As before, we use the BLYP pure functional with LANL2DZ and density fitting basis set W06. Charge of the QM region was assumed to be zero.

We show in our final example, that one can use the same prescription proposed earlier to isolate a portion of the monolayer for a QM description, while retaining an MM description of the remainder. For this purpose, we took the $[Au_{25}(SCH_3)_{18}]^-$ structure and changed the ligands in two of the semi-rings from methyl to ethylphenyl,

Table 7.5. Structure validation for different QM/MM models. All distances are reported in Angstroms.

Cluster	d_{21}	$(d_{21})_{XRAY}$	d_{rms}	$(d_{rms})_{XRAY}$	δ_S (%)
$[Au_{25}(SCH_3)_{18}]^-$	2.84	2.87	2.73	2.76	1.09
$[Au_{38}(SCH_3)_{24}]$	2.09	2.02	1.71	1.76	2.84
$[Au_{25}(SCH_3)_{12}(SCH_2CH_2Ph)_6]^-$	2.87	2.87	2.72	2.76	1.45

thus forming $[Au_{25}(SCH_3)_{12}(SCH_2CH_2Ph)_6]^-$ (see figure 7.4). The QM region contains two semi-rings on opposite sides of the structure and the C_i symmetry of the original structure is preserved. Again the Au_{13} core and remaining $(Au)_2(SCH_3)_3$ semi-rings are in the MM region. We optimized the geometry and calculated NMR properties of ^{13}C and ^{1}H. Results are reported in the following section.

7.3 Results and Discussions

We report in Table 7.5 an analysis of the optimized structure for the different clusters described in the previous section. To assess the accuracy of our structure, we define the parameters d_{21} and d_{rms} as the distance between two neighboring Au atoms in the core and the "root mean square" distance of all Au atoms from the central atom in the core, respectively. We define the percent error δ_S as,

$$\delta_S = \frac{|(d_{rms})_{XRAY} - (d_{rms})_{MODEL}|}{(d_{rms})_{XRAY}} \times 100 \tag{7.2}$$

We note that the maximum error in structure optimization using our QM/MM models is ~ 3 %, which is remarkably good. We then used the optimized structures to calculate NMR properties of ^{13}C and ^{1}H, which we present in Tables 7.6 and 7.7.

Guided by the benchmark studies of Cheeseman *et al.* [122], our calculations of NMR chemical shifts are performed with the B3LYP hybrid functional, using the LANL2DZ basis set for Au, and the 6–31G(d,p) for S, C and H. We see that the NMR isotropic shieldings obtained using the QM/MM model compare very well to that found using full DFT on the same $[Au_{25}(SCH_3)_{12}(SCH_2CH_2Ph)_6]^-$ structure. We also calculate the mean unsigned error (MUE) to compare theory with NMR experiments reported recently [100]. The mean unsigned error is defined as,

$$MUE = \frac{1}{n_i}\sum_i(|\delta^i_{model} - \delta^i_{experiment}|) \tag{7.3}$$

where n_i is the total number of different types of C and H atoms, and δ are the NMR chemical shifts. The maximum MUE is 3.5 ppm for ^{13}C and 0.18 ppm for ^{1}H NMR. Thus we see that both ^{13}C and ^{1}H agree remarkably well with the known experimental results. Although small, we believe that the discrepancies arise from the fact that the experimental structure has six semi-rings with CH_2CH_2Ph as the functional group for all ligands whereas the QM/MM and full DFT models have two semi-rings with CH_2CH_2Ph as ligands and the rest replaced with CH_3, so we are neglecting some of the electrostatic interactions that arise due to the difference in the structure. However, the error seems to be small in comparison to the huge gain in computational efficiency. More precisely, the time taken to caculate the NMR shielding tensors with the QM/MM model was approximately 1 hour, whereas the same calculation with full DFT took 12 hours using the same hardware.

Table 7.6. ^{13}C NMR chemical shifts δ (in ppm) for $[Au_{25}(SCH_3)_{12}(SCH_2CH_2Ph)_6]^-$ cluster. Reported are the calculated values within the QM/MM approximation, full DFT calculation, and experimental values.

Atom	QM/MM	DFT	Experiment [100]
α–C_{inner}	50.75	55.80	—
α–C_{outer}	48.72	49.74	35.97
β–C_{inner}	45.11	44.26	—
β–C_{outer}	44.07	43.47	42.18
i–C_{inner}	137.35	141.05	141.88
i–C_{outer}	137.43	140.42	140.88
m–C_{inner}	125.48	125.00	128.52
m–C_{outer}	125.61	124.94	128.63
o–C_{inner}	125.29	126.49	129.85
o–C_{outer}	125.37	125.42	129.30
p–C_{inner}	123.99	122.45	126.27
p–C_{outer}	123.96	122.35	126.49
MUE (in ppm)	3.50	3.23	

Table 7.7. ^{1}H NMR chemical shifts δ (in ppm) for $[Au_{25}(SCH_3)_{12}(SCH_2CH_2Ph)_6]^-$ cluster.

Atom	QM/MM	DFT	Experiment [100]
α–$CH_{2,inner}$	2.92	3.23	3.80^{broad}
α–$CH_{2,outer}$	3.18	2.97	3.13
β–$CH_{2,inner}$	2.93	2.95	3.13
β–$CH_{2,outer}$	3.03	3.07	t2.93
m–CH_{inner}	7.28	7.24	7.15
m–CH_{outer}	7.29	7.19	7.19
o–CH_{inner}	7.19	7.54	7.19
o–CH_{outer}	7.23	7.35	7.14
p–CH_{inner}	7.23	7.02	7.08
p–CH_{outer}	7.27	7.09	7.15
MUE (in ppm)	0.18	0.18	

7.4 Concluding Remarks

The use of X-ray crystallography to determine the structure of gold nanoparticles has been limited, owing partly to the difficulty of obtaining samples of sufficiently uniform size for the growth of single crystals. Until recently, there had been just one example of an Au cluster, Au_{102}(p-MBA)$_{44}$, which had been determined by crystallography [96]. Since then, there have been successful crystal structure determinations of smaller sized gold clusters like Au_{25} [97] and Au_{38} [120]. The recent availability of detailed structural data has created an opportunity for the construction and validation of computational methods for modeling these systems. Starting from the analysis of $[Au_{25}(SCH_3)_{18}]^-$ molecular ion, we have developed generalized hybrid QM/MM models to accurately describe the structure of monolayer protected gold clusters. We have found that errors in the calculated geometries from our QM/MM model are $\sim 3\%$, compared to the crystal structures. In addition, the isotropic chemical shifts obtained from NMR calculation agree very well among the QM/MM model, full DFT calculations and experiment. Use of these hybrid models not only saves computational resources but also enables the study of physical properties and chemical reactions for larger molecular ions where physical insight can be obtained by describing only a small region of the system at a high QM level.

Chapter 8

Summary and Outlook

In this thesis, we present accurate electronic structure calculations for potential energy curves of ground and excited states of both homonuclear and heteronuclear alkaline-earth molecular ions. We also compute the transition dipole moments, radiative lifetimes, polarizabilities, and long-range coefficients for such ionic dimers. So far, very little is known about these systems and we believe that our calculations would provide the foundation on which modern experiments on these cold molecular ions could be developed. The initial goal for such experiments would be to study resonant charge transfer. Since in the alkaline-earth ionic dimers the charge and the neutral atom can be imaged separately, experiments on ultracold atom-ion collisions and resonant charge transfer could be accurately controlled and measured.

We have also explored in Chapter 3 a pathway to form Be_2^+, in the long-range shallow well of the metastable B $^2\Sigma_g^+$ state by ultracold photoassociation. Such experiments for formation of cold molecular ions would help understand not only the problems of atomic physics, but can also lead to model quantum systems for the study of many body physics, disorder, and artificial crystals.

In Chapter 4, we have presented our recent findings for the non-adiabatic corrections to the Born-Oppenheimer approximation. Although, for most practical scenarios, the corrections to Born-Oppenheimer approximation are extremely small and negligible, such corrections become important for studies involving the mass of nuclei. For accurate description of studies involving ultracold atom-ion collisions among two different isotopes of the same element [5], non-adiabatic corrections must be included in the description of the quantum system.

In Chapter 6 we calculate the hyperfine structure of NaCa^+. The magnetic hyperfine spectra of the $\mathrm{a}^3\Sigma^+$ state shows a well separated spacing of the energy levels $\sim$ 50 MHz at a magnetic field of 100 G. Such spacing is experimentally achievable.

Last but not the least, we have described in Chapter 7 the development of a hybrid QM/MM method to treat polyatomic systems, like ionic clusters. The size of the system forces the *ab initio* calculations at the limits of computational tractability. However, we demonstrate that by intelligent partition of the large system, we can still achieve the computational accuracy of full quantum mechanical descriptions.

Appendix A

Input files for Quantum Chemistry programs

A.1 `MOLPRO` input

We list a sample input file for use with the `MOLPRO` program, which calculates the total valence energy for the B $^2\Sigma_g^+$ state in the Be_2^+ molecular ion. The sample input uses the aug-cc-pVQZ basis set, available from the EMSL basis set library.

```
!
***,Be2+ Sigma G State Potential Energy Curve

memory,250,M
gthresh, zero=1.d-14, oneint=1.d-14, twoint=1.d-14, energy=1.d-12

basis={
!
! BERYLLIUM         (13s,7p,4d,3f,2g) -> [6s,5p,4d,3f,2g]
! BERYLLIUM         (12s,6p,3d,2f,1g) -> [5s,4p,3d,2f,1g]
! BERYLLIUM         (1s,1p,1d,1f,1g)
s, BE , 14630.0000000, 2191.0000000, 498.2000000, 140.9000000,
45.8600000, 16.4700000, 6.3190000, 2.5350000, 1.0350000, 0.2528000,
0.1052000, 0.0426100, 0.0143900
c, 1.9, 0.0000920, 0.0007130, 0.0037350, 0.0154680, 0.0528740,
0.1456940, 0.3026810, 0.4049360, 0.2223870
c, 1.9, -0.0000170, -0.0001300, -0.0006790, -0.0028570, -0.0098130,
-0.0286090, -0.0637600, -0.1172310, -0.1212020
c, 10.10, 1
c, 11.11, 1
c, 12.12, 1
c, 13.13, 1
p, BE , 14.0300000, 3.1680000, 0.9024000, 0.3036000, 0.1130000,
0.0428600, 0.0065000
c, 1.3, 0.0040990, 0.0256260, 0.1037680
c, 4.4, 1
```

```
c, 5.5, 1
c, 6.6, 1
c, 7.7, 1
d, BE , 1.0720000, 0.4410000, 0.1811000, 0.0554000
c, 1.1, 1
c, 2.2, 1
c, 3.3, 1
c, 4.4, 1
f, BE , 0.4810000, 0.2550000, 0.0930000
c, 1.1, 1
c, 2.2, 1
c, 3.3, 1
g, BE , 0.4150000, 0.1834000
c, 1.1, 1
c, 2.2, 1
}

d=[100.0, 50.0, 20.0, 10.0, 7.5, 5.0, 3.0]

do i=1,#d
! Be2+ Molecule
data,truncate,2100.2
geomtyp=xyz
geometry={
   2
  Be2+
  be1 0.   0.  d(i)*toang
  be2 0.   0. -d(i)*toang
}
set,charge=1
{rhf;wf,7,1,1;
save,2100.2;start,atden}
ehf1(i)=energy
{fci;}
e1(i)=energy
enddo

do i=1,#d
! Be+ Ion
geomtyp=xyz
symmetry,x,y
geometry={
   2
  Be2+
  be1 0.   0.  d(i)*toang
  be2 0.   0. -d(i)*toang
}
set,charge=1
dummy,Be1
{rhf;wf,3,1,1;}
e2(i)=energy
enddo
```

```
do i=1,#d
! Be Atom
geomtyp=xyz
symmetry,x,y
geometry={
  2
 Be2+
 be1 0.   0.  d(i)*toang
 be2 0.   0. -d(i)*toang
}
set,charge=0
dummy,Be1
{rhf;wf,4,1,0;}
ehf3(i)=energy
ccsd
e3(i)=energy
enddo

do i=1,#d
d(i)=2*d(i)
diff(i)=(e1(i)-e2(i)-e3(i))*tocm
enddo

table,d,diff
digits,2,2
```

A.2 `PSI3` input

Following is a sample input file for B $^2\Sigma_g^+$ state in the Be_2^+ molecular ion, used with the `PSI3` program with aug-cc-pV5Z basis set. The CI program in `PSI3` is much faster than `MOLPRO`, so for large basis set calculations, it is much preferred.

```
% Be2+

psi: (
  label = "Be2+ sigma g"
  memory = (4048.0 MB)
  charge = 1
  multp = 2
  jobtype = sp
  wfn = detci
  fci = true
  convergence = 7
  reference = rohf
```

```
  dertype = none
  basis = "AV5Z"
  puream = true
% occ 1
  docc = (1 0 0 0 0 2 0 0)
  socc = (1 0 0 0 0 0 0 0)
% occ 2
% docc = (2 0 0 0 0 1 0 0)
% socc = (1 0 0 0 0 0 0 0)
  freeze_core = true
%  chkpt_mos = true
  units = bohr
  zmat = (
    Be
    Be 1 2.0
  )
)

scf: (
  convergence = 14
  maxiter = 200
% print_mos = true
)

basis: (
BERYLLIUM:"AV5Z" = (
         (S (  54620.00000000       0.00001800)
            (   8180.00000000       0.00013800)
            (   1862.00000000       0.00072300)
            (    527.30000000       0.00303900)
            (    172.00000000       0.01090800)
            (     62.10000000       0.03403500)
            (     24.21000000       0.09119300)
            (      9.99300000       0.19926800)
            (      4.30500000       0.32935500)
            (      1.92100000       0.34048900) )
         (S (  54620.00000000      -0.00000300)
            (   8180.00000000      -0.00002500)
            (   1862.00000000      -0.00013100)
            (    527.30000000      -0.00055800)
            (    172.00000000      -0.00198800)
            (     62.10000000      -0.00637000)
            (     24.21000000      -0.01721700)
            (      9.99300000      -0.04085800)
            (      4.30500000      -0.07423700)
            (      1.92100000      -0.11923400) )
         (S (      0.86630000       1.00000000) )
         (S (      0.24750000       1.00000000) )
         (S (      0.10090000       1.00000000) )
         (S (      0.04129000       1.00000000) )
         (P (     43.75000000       0.00063300)
            (     10.33000000       0.00480800)
```

```
              (        3.22600000       0.02052700)
              (        1.12700000       0.06781600)  )
          (P  (        0.43340000       1.00000000)  )
          (P  (        0.18080000       1.00000000)  )
          (P  (        0.07827000       1.00000000)  )
          (P  (        0.03372000       1.00000000)  )
          (D  (        1.63500000       1.00000000)  )
          (D  (        0.74100000       1.00000000)  )
          (D  (        0.33500000       1.00000000)  )
          (D  (        0.15190000       1.00000000)  )
          (F  (        0.68600000       1.00000000)  )
          (F  (        0.40100000       1.00000000)  )
          (F  (        0.23500000       1.00000000)  )
          (G  (        0.60300000       1.00000000)  )
          (G  (        0.32400000       1.00000000)  )
          (H  (        0.51000000       1.00000000)  )
% AV5Z  diffuse
          (S  (        0.013777         1.0)  )
          (P  (        0.007668         1.0)  )
          (D  (        0.077200         1.0)  )
          (F  (        0.013750         1.0)  )
          (G  (        0.174000         1.0)  )
          (H  (        0.225000         1.0)  )
         )
)
```

A.3 Transition Moment calculation code

This is a standard input file for `MOLPRO` CI program, to calculate the electronic transition dipole moment, coupling the X $^2\Sigma_u^+$ state to the B $^2\Sigma_g^+$ state in Be_2^+. This can be easily modified to calculate other transition moments, just by changing the respective symmetry of the relevant state.

```
!
***,Be2+ Sigma-U to Sigma-G Transition Moment

memory,250,M
gthresh,energy=1.d-12

basis={
!
! BE   cc-pVTZ
!
```

```
sp,Be,vtz;c;
d,Be,0.3493,0.1724;
f,Be,0.3423;
s,Be,0.0147;
p,Be,0.0093;
d,Be,0.0588;
f,Be,0.1188;
s,Be,3.9564,1.4164;
p,Be,8.7733,2.0354;
d,Be,1.6193;
}

d=[1000.0, 30.0, 20.0, 19.0, 18.0, 17.0, 16.0, 15.0, 14.0, 13.0, 12.0,
11.0, 10.0, 9.5, 9.0, 8.5, 8.0, 7.5, 7.0, 6.5, 6.0, 5.9, 5.8, 5.7, 5.6,
5.5, 5.4, 5.3, 5.2, 5.1, 5.0, 4.9, 4.8, 4.7, 4.6, 4.5, 4.4, 4.3, 4.2,
4.1, 4.0, 3.9, 3.8, 3.7, 3.6, 3.5, 3.4, 3.3, 3.2, 3.1, 3.0]

do i=1,#d
geometry={Be; Be 1 d(i)}
set,charge=1

{rhf;wf,7,5,1;}

{multi;maxit,40;
occ,3,1,1,0,3,1,1,0;
closed,0,0,0,0,0,0,0,0;
wf,7,5,1;
wf,7,1,1;}

! Be2+ Sigma-U

{ci;wf,7,5,1;maxit,500;save,6140.2;}
e1(i)=energy


! Be2+ Sigma-G

{ci;wf,7,1,1;maxit,500;save,7140.2;}
e2(i)=energy

! Be2+ Pi-U to Sigma-G transition
{ci;trans,6140.2,7140.2,dmx}

mu(i)=trdmx
enddo

table,d,e1,e2,mu
digits,2,12,12,12
```

A.4 `CFOUR` input

The `CFOUR` program has the fastest coupled cluster (CC) code in our experience. The input file is always named ZMAT. Here is a sample ZMAT input file, for Ca_2^+ restricted inner valence (RIV) calculation at the CCSDT level of theory,

```
CCSDT test case
CA
CA 1 R

R=VAR

*CFOUR(CALC=CCSDT,BASIS=SPECIAL
   PRINT=0,REF=ROHF
   UNITS=1,CHARGE=1
   MULTIPLICITY=2
   CC_CONV=10,CC_EXPORDER=20,CC_MAXCYC=500
   OCCUPATION=6-2-2-0-6-2-2-0/5-2-2-0-6-2-2-0
   DROPMO=1-2-3-4-5-6-7-8-9-10
   MEMORY=80000000)

CA:cc-pwCVTZ
CA:cc-pwCVTZ
```

A.5 `PYTHON` script for quantum chemistry programs

Here is a `PYTHON` script, which can be used with most quantum chemistry programs to generate a table of data points, for a desired level of theory and internuclear separations. It uses common regular-expressions (REGEX) and assumes that the UNIX command line is used to run the script.

```
#!usr/bin/python
# Copyright by Sandipan Banerjee, UCONN
# Python script for running CFOUR program to generate
data sets for a bunch of given R values

import os, sys
import string

r = ’30.0 28.0 24.0 20.0 18.0 16.5 16.0 15.5 14.0 13.5 12.0
11.0 10.0 9.0 8.0 7.0 6.0 5.0’.split()
log = ’ca2p_ccsdt_riv_sg_’
b = ”ZMAT”
ext = ’.1’
#outfile = ’output_sg_av5z.dat’

def makeinp(oldFile,newFile):
  f1 = open(oldFile, ”r”)
  f2 = open(newFile, ”w”)
  while 1:
        text = f1.readline()
        if text == ””:
                break
        text = text.replace(”VAR”,r[i])
        f2.write(text)
  f1.close()
  f2.close()
  return

for i in range(len(r)):
  print ’Running’, r[i]
  a = ”ZMAT.ca2p”
  makeinp(a,b)
  out = (log + ’’.join(r[i]) + ext)
  os.system(’xcfour >& %s’ % (out))
  os.system(’xclean’)
else:
  print ’The loop is over’
```

A.6 Dipole Polarizabilty calculation code

This is sample `MOLPRO` input file, for calculation of static dipole polarizability of the Ca atom in its ground state, using the finite-field method. This is performed at the CCSD(T) level of theory, however this can be easily modified for use with any other level of theory.

```
!
***,Ca Dipole Polarizability

memory,250,M
gthresh, zero=1.d-14, oneint=1.d-14, twoint=1.d-14, energy=1.d-12

basis=aug-cc-pV5Z

 symmetry,x,y
 geometry={ Ca }

 !define finite field strengths

 field=[0,0.0001,-0.0001]

 !loop over fields

 do i=1,#field
   !add finite field along z to H

   dip,,,field(i)
   hf
   {ccsd(t);core;maxit,200}
   e(i)=energy
 enddo

 !dipole moment as first energy derivative
 dipmz=(e(2)-e(3))/(field(2)-field(3))

 !polarizability as second der.
 dpolz=(e(2)+e(3)-2*e(1))/((field(2)-field(1))*(field(3)-field(1)))

 table,e(1),dipmz,dpolz
```

A.7 Quadrupole Polarizabilty calculation code

This is sample `MOLPRO` input file, for calculation of static quadrupole polarizability of the Ca atom in its ground state, using the finite-field method.

```
!
***,Ca Quadrupole Polarizability

memory,250,M
gthresh, zero=1.d-14, oneint=1.d-14, twoint=1.d-14, energy=1.d-12

basis=aug-cc-pV5Z

 symmetry,x,y
 geometry={ Ca }

 !define finite field strengths
 field=[0,0.0001,-0.0001]

 do i=1,#field
   quad,,,field(i)
   hf
   {ccsd(t);core;maxit,200}
   e(i)=energy
 enddo

 !quadrupole moment as first energy derivative
 quadmz=(e(2)-e(3))/(field(2)-field(3))

 !polarizability as second der.
 qpolz=(e(2)+e(3)-2*e(1))/((field(2)-field(1))*(field(3)-field(1)))

 table,e(1),quadmz,qpolz
```

Appendix B

Input/ Output for bound vibrational levels

B.1 Sample input for LEVEL code

We have used the `LEVEL` program, developed by Le Roy to calculate energies of bound vibrational levels for potential energy curves for various molecular ions studied. This program is based on the Numerov algorithm implemented in FORTRAN 90. It can calculate energies and wavefunctions for different vibrational levels. We have also used it to calculate Franck-Condon overlaps between two potentials, and to calculate Einstein A-coefficient for radiative decay.

```
4 9   4 9   1   1            ! IAN! IMN1 IAN2 IMN2 CHARGE NUMPOT
' Levels of potential for 2(Sigma)g State of Be2+ '
0.001 1.3 90. 1.d-06         ! RH RMIN RMAX EPS
100 -1 0 0.D0                ! NTP LPPOT IOMEG VLIM
0 1 3 4 0.D5                 ! NUSE IR2 ILR NCN CNN
1.0D0 1.0D0 0.d0             ! RFACT EFACT VSHIFT
1.58753163240000             10313.68707042250000
1.67840044637577             5132.42814242910000
1.76926926035149             1618.33669321841000
1.86013807432726             -602.48983533663300
1.95100688830304             -1908.84232400221000
2.04187570227881             -2544.36159618185000
2.13274451625453             -2710.25471908260000
2.22361333023030             -2560.19886303708000
2.31448214420607             -2206.96259059629000
2.40535095818179             -1730.62302685235000
2.49621977215757             -1207.03593501474000
2.58708858613334             -690.79809128338000
2.67795740010911             -227.06410390732600
2.76882621408483             160.55629241621000
```

2.85969502806060	477.81791782795400
2.95056384203638	730.37504802731800
3.04143265601210	924.16506871250100
3.13230146998787	1064.78118301374000
3.22317028396364	1159.01977109418000
3.31403909793941	1215.52767930164000
3.40490791191513	1240.60857200174000
3.49577672589091	1239.96482959616000
3.58664553986668	1218.54772483866000
3.67751435384240	1180.48510512383000
3.76838316781817	1129.67495626256000
3.85925198179394	1069.43324271480000
3.95012079576972	1002.52274490642000
4.04098960974544	931.36853293287000
4.13185842372121	858.20319683126200
4.22272723769698	784.33084945582200
4.31359605167275	711.26729836102800
4.40446486564847	640.02992712237800
4.49533367962425	571.53141140052400
4.58620249360002	506.36782467326300
4.67707130757574	444.99337438687400
4.76794012155151	387.64159867329900
4.85880893552728	334.44118026866500
4.94967774950305	285.43778693594000
5.04054656347878	240.58648591140600
5.13141537745455	199.77967735918000
5.22228419143032	162.85728992069600
5.31315300540604	129.61977127596400
5.40402181938171	99.84859327147650
5.49489063335737	73.31807799541440
5.58575944733357	49.81368147890520
5.67662826130924	29.10286140782550
5.76749707528490	10.95092726875040
5.85836588926057	−4.86929844335600
5.94923470323624	−18.57166225016150
6.04010351721190	−30.36143770779330
6.13097233118810	−40.42782630158080
6.22184114516377	−48.93172634756480
6.31270995913943	−56.04099579556700
6.40357877311510	−61.91213495822640
6.49444758709076	−66.68472351900470
6.58531640106643	−70.48986360311000
6.67618521504263	−73.44507098485330
6.76705402901829	−75.65195551119680
6.85792284299396	−77.20063125060340
6.94879165696963	−78.17826549377740
7.03966047094530	−78.66041140042540
7.13052928492096	−78.71989361778610
7.22139809889716	−78.41632830057250
7.31226691287282	−77.81125789116080
7.40313572684849	−76.94201050152060
7.49400454082416	−75.84455772988480

```
7.58487335479982        -74.58855355349000
7.67574216877602        -73.16511367354320
7.76661098275169        -71.64245149949050
7.85747979672735        -69.99879594525370
7.94834861070302        -68.31123675481180
8.03921742467869        -66.57832457477190
8.13008623865435        -64.80096134570040
8.22095505263055        -63.01682673966720
8.31182386660622        -61.22203395958390
8.40269268058188        -59.41652530769020
8.49356149455755        -57.61930446612490
8.58443030853322        -55.85202645949550
8.67529912250888        -54.11557820451800
8.76616793648508        -52.40584474695510
8.85703675046075        -50.71871112183970
8.94790556443641        -49.05006237454840
9.03877437841208        -47.40242345820210
9.12964319238775        -45.81536924192680
9.22051200636341        -44.28992638006390
9.31138082033961        -42.81855805081400
9.40224963431527        -41.39372741731720
9.49311844829094        -40.00789765694840
9.58398726226661        -38.66011892823240
9.67485607624228        -37.36552067869560
9.76572489021794        -36.11797980470830
9.85659370419414        -34.90940187025560
9.94746251816980        -33.73169242896620
10.03833133214550       -32.57675704379400
10.12920014612110       -31.44674854590620
10.22006896009680       -30.36087897065000
10.31093777407250       -29.32553493738930
10.40180658804870       -28.34670562310380
10.49267540202430       -27.43038020749740
10.58354421600000       -26.58254786842470
-999 1 2 -1 0 1 -1 -10           ! NLEV1 AUTO1 LCDC
LXPCT NJM JDJR IWR LPRWF
0 0                                       ! IV(1) IJ(1) GV(1)=Trial Energy
```

B.2 Sample output for `LEVEL` code

```
Find  21 Potential-1 vibrational levels with  J=  0

v       E(v)          v       E(v)          v       E(v)          v       E(v)
------------------    ------------------    ------------------    ------------------
0   -2444.3506        6      -69.7655       12      -10.9105      18       -0.8481
1   -1925.3493        7      -53.7117       13       -7.8944      19       -0.4300
2   -1425.2887        8      -40.1671       14       -5.5667      20       -0.1870
3    -948.1527        9      -29.0517       15       -3.7865
4    -497.8803        10      -20.5207      16       -2.4579
5     -79.2265        11      -14.8901      17       -1.5021
```

Appendix C

Non-Adiabatic corrections

C.1 Diagonal and off-diagonal matrix element computation

The diagonal and off-diagonal corrections for $\tilde{V}_{\alpha\beta}$ are implemented in `MOLPRO`, using the following code.

```
!
***, Be2+ Non-Adiabatic Corrections

memory,350,m;

basis={
!
! BE  cc-pV5Z
!
sp,Be,v5z;c;
d,Be,1.7175,0.7646,0.3404,0.1515;
f,Be,0.6127,0.3568,0.2078;
g,Be,0.5980,0.3183;
h,Be,0.5142;
s,Be,0.0128;
p,Be,0.0076;
d,Be,0.0428;
f,Be,0.0719;
g,Be,0.0979;
h,Be,0.2033;
}

mass, isotope, Be1=9.012182, Be2=10.013534

ma = 9.012182
mb =10.013534
M=(ma+mb)

DeltaR = 5.0D-03
```

```
dis=30.00

!Do i=1, 1
Do i=1, 135

   r(i) = dis

   R00 = -1.0D+00 * mb * dis / (ma + mb)

   Be1Z = R00
   Be2Z = R00 + dis
   Be1X = 0.0
   Be2X = 0.0
   Be1Y = 0.0
   Be2Y = 0.0


   symmetry,x
   orient,noorient
   geomtyp=xyz

   geometry={
    Be1 Be1X*toang Be1Y*toang Be1Z*toang
    Be2 Be2X*toang Be2Y*toang Be2Z*toang
    }

   IF (i.eq.1) Then

      {multi;occ,8,2;closed,0,0;
       start,2144.2;
       wf,7,1,1;state,2;natorb,2145.2,ci,print;}

   End IF

   label1:
   {multi;occ,8,2;closed,0,0;
    wf,7,1,1;state,2;natorb,2145.2,ci,print;maxiter,40}

   if (status.lt.0) then
      goto, label1, [-1], [6]
   endif

   {ci;noexc;
    wf,7,1,1;state,2,1,2;save,6000.2;orbital,2145.2;
    thresh,energy=1.d-10,coeff=5.d-10}

   text, move Y Plus Delta_R

   Be1Y = DeltaR

   !orient,noorient
```

```
geomtyp=xyz
geometry={
Be1  Be1X*toang Be1Y*toang Be1Z*toang
Be2  Be2X*toang Be2Y*toang Be2Z*toang
}


label2:
{multi;occ,8,2;closed,0,0;
 start,2145.2;wf,7,1,1;state,2;orbital,2146.2;maxiter,40}

if (status.lt.0) then
   goto, label2, [-1], [6]
endif

{ci;noexc;
 wf,7,1,1;state,2,1,2;save,6001.2;orbital,2146.2;
 thresh,energy=1.d-10,coeff=5.d-10}

{ci;trans,6000.2,6001.2,biorth,ov}
ABO1(i) = trov(1)
ABO2(i) = trov(2)
ABO3(i) = trov(3)
ABO4(i) = trov(4)


 text, move Y Minus Delta_R

 Be1Y = -DeltaR

!orient,noorient
geomtyp=xyz
geometry={
Be1  Be1X*toang Be1Y*toang Be1Z*toang
Be2  Be2X*toang Be2Y*toang Be2Z*toang
}

label3:
{multi;occ,8,2;closed,0,0;
 start,2145.2;wf,7,1,1;state,2;orbital,2147.2;maxiter,40}

if (status.lt.0) then
   goto, label3, [-1], [6]
endif

{ci;noexc;
 wf,7,1,1;state,2,1,2;save,6002.2;orbital,2147.2;
 thresh,energy=1.d-10,coeff=5.d-10}


{ci;trans,6001.2,6002.2,biorth,ov}
KBO1(i) = trov(1)
```

```
KBO2(i) = trov(2)
KBO3(i) = trov(3)
KBO4(i) = trov(4)

{ci;trans,6002.2,6001.2,biorth,ov}

KKBO1(i) = trov(1)
KKBO2(i) = trov(2)
KKBO3(i) = trov(3)
KKBO4(i) = trov(4)

{ci;trans,6000.2,6002.2,biorth,ov}
BBO1(i) = trov(1)
BBO2(i) = trov(2)
BBO3(i) = trov(3)
BBO4(i) = trov(4)


text, move Y Plus 2*Delta_R

Be1Y = 2*DeltaR

!orient,noorient
geomtyp=xyz
geometry={
Be1  Be1X*toang Be1Y*toang Be1Z*toang
Be2  Be2X*toang Be2Y*toang Be2Z*toang
}


label4:
{multi;occ,8,2;closed,0,0;
 start,2145.2;wf,7,1,1;state,2;orbital,2148.2;maxiter,40}

if (status.lt.0) then
   goto, label4, [-1], [6]
endif

{ci;noexc;
 wf,7,1,1;state,2,1,2;save,6003.2;orbital,2148.2;
 thresh,energy=1.d-10,coeff=5.d-10}

{ci;trans,6000.2,6003.2,biorth,ov}
ABO11(i) = trov(1)
ABO22(i) = trov(2)
ABO33(i) = trov(3)
ABO44(i) = trov(4)


 text, move Y Minus 2*Delta_R

 Be1Y = -2*DeltaR
```

```
!orient,noorient
geomtyp=xyz
geometry={
Be1  Be1X*toang Be1Y*toang Be1Z*toang
Be2  Be2X*toang Be2Y*toang Be2Z*toang
}

label5:
{multi;occ,8,2;closed,0,0;
 start,2145.2;wf,7,1,1;state,2;orbital,2149.2;maxiter,40}

if (status.lt.0) then
   goto, label5, [-1], [6]
endif

{ci;noexc;
 wf,7,1,1;state,2,1,2;save,6004.2;orbital,2149.2;
 thresh,energy=1.d-10,coeff=5.d-10}


{ci;trans,6003.2,6004.2,biorth,ov}
KBO11(i) = trov(1)
KBO22(i) = trov(2)
KBO33(i) = trov(3)
KBO44(i) = trov(4)

{ci;trans,6004.2,6003.2,biorth,ov}

KKBO11(i) = trov(1)
KKBO22(i) = trov(2)
KKBO33(i) = trov(3)
KKBO44(i) = trov(4)

{ci;trans,6000.2,6004.2,biorth,ov}
BBO11(i) = trov(1)
BBO22(i) = trov(2)
BBO33(i) = trov(3)
BBO44(i) = trov(4)



! Diagonal corrections V_aa and V_bb

VaaBO(i) = (-6.93986)*(1/24)*(16*KKBO1(i)
- KKBO11(i) - 15)
VaaBOcm(i) = ((-6.93986)*(1/24)*(16*KKBO1(i)
- KKBO11(i) - 15))*tocm

Vaa(i) = VaaBO(i)-VaaBO(1)

VbbBO(i) = (-6.93986)*(1/24)*(16*KKBO4(i)
```

```
   - KKBO44(i) - 15)
   VbbBOcm(i) = ((-6.93986)*(1/24)*(16*KKBO4(i)
   - KKBO44(i) - 15))*tocm

   Vbb(i) = VbbBO(i)-VbbBO(1)

   ! Off-Diagonal correction V_ab

   VabBO(i) = (-6.93986)*(1/48)*(16*(KKBO2(i)+KKBO3(i))
   - (KKBO22(i)+KKBO33(i)))
   VabBOcm(i) = ((-6.93986)*(1/48)*(16*(KKBO2(i)+KKBO3(i))
   - (KKBO22(i)+KKBO33(i))))*tocm

   Vab(i) = VabBO(i)-VabBO(1)

    r(i) = dis

    !dis = dis - 0.1
    dis = dis - 0.2
EndDo


{table,r,KKBO1,KKBO2,KKBO3,KKBO4
 title, < PSI(Y–dY) | PSI(Y+dY) >
 digits,2,13,13,13,13
 sort,1}

{table,r,KKBO11,KKBO22,KKBO33,KKBO44
 title, < PSI(Y-2*dY) | PSI(Y+2*dY) >
 digits,2,13,13,13,13
 sort,1}

{table,r,VaaBO,VaaBOcm
 title, VaaBO
 digits,2,13,2
 sort,1}

{table,r,VbbBO,VbbBOcm
 title, VbbBO
 digits,2,13,2
 sort,1}

{table,r,VabBO,VabBOcm
 title, VabBO
 digits,2,13,2
 sort,1}

{table,r,Vaa
 title, Vaa
 digits,2,13
 sort,1}
```

```
{table,r,Vbb
 title, Vbb
 digits,2,13
 sort,1}

{table,r,Vab
 title, Vab
 digits,2,13
 sort,1}
```

C.2 More off-diagonal couplings

The off-diagonal first derivative coupling $F_{\alpha\beta}$, is implemented in `MOLPRO` using the following code. This example is for Be_2^+.

```
!
***, Be2+ Isotope coupling

memory,240,m;

basis={
!
! BE   cc-pV5Z
!
sp,Be,v5z;c;
d,Be,1.7175,0.7646,0.3404,0.1515;
f,Be,0.6127,0.3568,0.2078;
g,Be,0.5980,0.3183;
h,Be,0.5142;
s,Be,0.0128;
p,Be,0.0076;
d,Be,0.0428;
f,Be,0.0719;
g,Be,0.0979;
h,Be,0.2033;
}

d=[30.0, 25.0, 20.0, 18.0, 16.0, 14.0, 12.0, 10.0, 9.0, 8.5,
8.0, 7.5, 7.0, 6.8, 6.6, 6.4, 6.2, 6.0, 5.8, 5.6, 5.4, 5.2, 5.0,
4.8, 4.6, 4.4, 4.2, 4.0, 3.8, 3.6, 3.4]

do i=1,#d
mass, isotope, Be1=9.012182, Be2=10.013534

ma = 9.012182
```

```
mb =10.013534
M=(ma+mb)
mul=ma*mb

fac=(0.5/mul)*(ma-mb)

symmetry,x
orient,charge

geometry={be1; be2 1 d(i)}

set,charge=1
{rhf;wf,7,1,1;}

{multi;occ,8,2;closed,0,0;
wf,7,1,1;state,2;natorb,2145.2,ci,print;}

{ci;noexc;
 wf,7,1,1;state,2,1,2;save,6000.2;orbital,2145.2;
thresh,energy=1.d-10,coeff=5.d-10}

{ci;trans,6000.2,6000.2,biorth,velo}

enddo
```

Finally, the off-diagonal rotational coupling $L_{\alpha\beta}$, between the ${}^2\Sigma_u^+$ and ${}^2\Pi_u$ states is given by,

```
!
***, Be2+ Rotational Coupling

memory,240,m;

basis={
!
! BE   cc-pV5Z
!
sp,Be,v5z;c;
d,Be,1.7175,0.7646,0.3404,0.1515;
f,Be,0.6127,0.3568,0.2078;
g,Be,0.5980,0.3183;
h,Be,0.5142;
s,Be,0.0128;
p,Be,0.0076;
d,Be,0.0428;
f,Be,0.0719;
g,Be,0.0979;
h,Be,0.2033;
```

```
}

d=[30.0, 25.0, 20.0, 18.0, 16.0, 14.0, 12.0, 10.0,
9.0, 8.5, 8.0, 7.5, 7.0, 6.8, 6.6, 6.4, 6.2, 6.0, 5.8, 5.6,
5.4, 5.2, 5.0, 4.8, 4.6, 4.4, 4.2, 4.0, 3.8, 3.6, 3.4, 3.2, 3.0]

do i=1,#d

ma = 9.012182
mb =10.013534
M=(ma+mb)
mul=ma*mb

fac=(0.5/mul)*(ma-mb)

geometry={be1; be2 1 d(i)}

set,charge=1
{rhf;wf,7,5,1;}

{multi;occ,3,1,1,0,3,1,1,0;
closed,0,0,0,0,0,0,0,0;
wf,7,5,1;
wf,7,1,1;
wf,7,2,1;
maxiter,40;
}

{ci;noexc;
 wf,7,5,1;save,6000.2;}

{ci;noexc;
 wf,7,2,1;save,6001.2;}

{ci;trans,6000.2,6001.2,biorth,Ly}

tl(i)=trly
enddo

table,d,tl
digits,2,13
```

C.3 Non-adiabatic corrections in Mg_2^+ and Ca_2^+

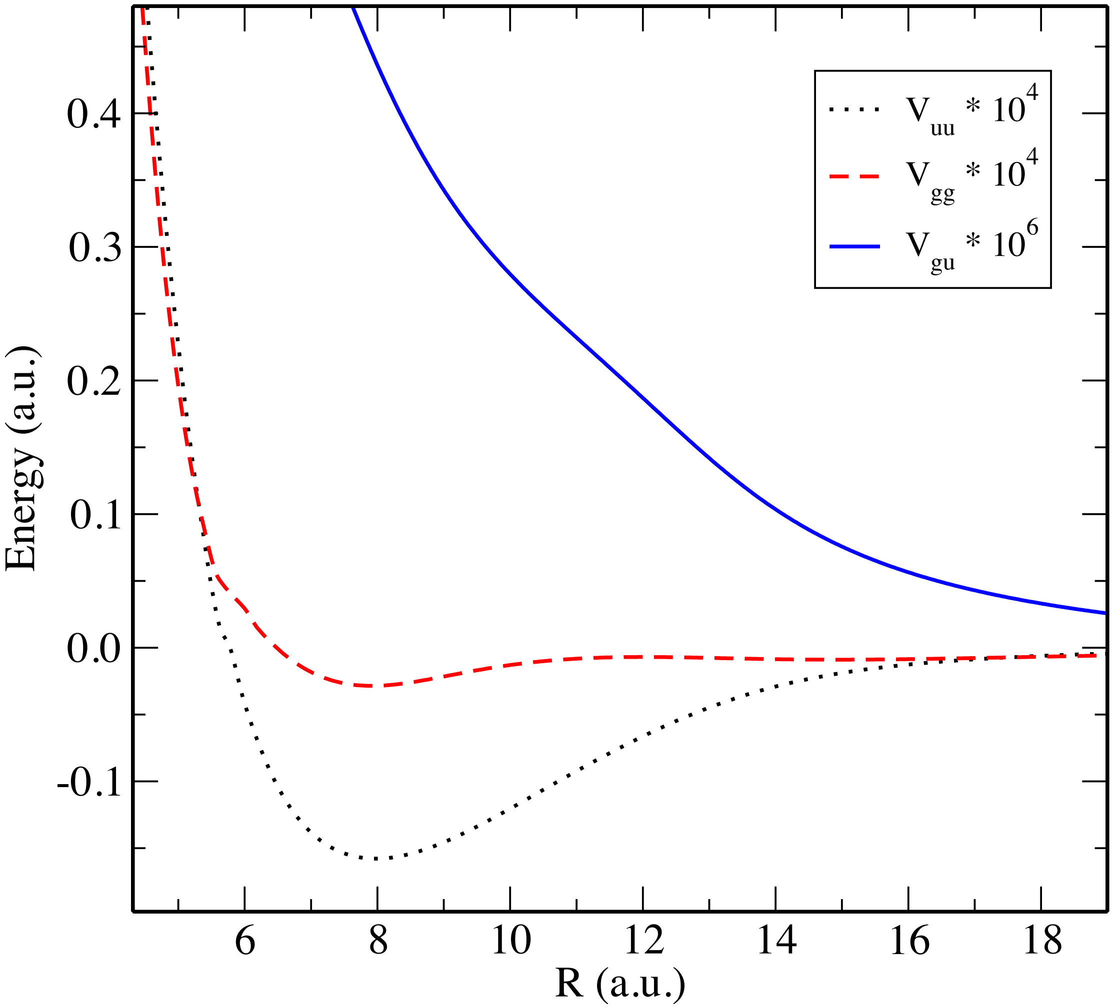

Figure C.1. Calculated $V_{\alpha\beta}$ coupling between the X $^2\Sigma_u^+$ and B $^2\Sigma_g^+$ states in the ^{24}Mg^{25}Mg$^+$ molecular ion. The diagonal couplings (multiplied by 10^4) are shown in black (dotted) and red (dashed) lines, and off-diagonal coupling V_{gu} (multiplied by 10^6) is shown in blue (solid) line.

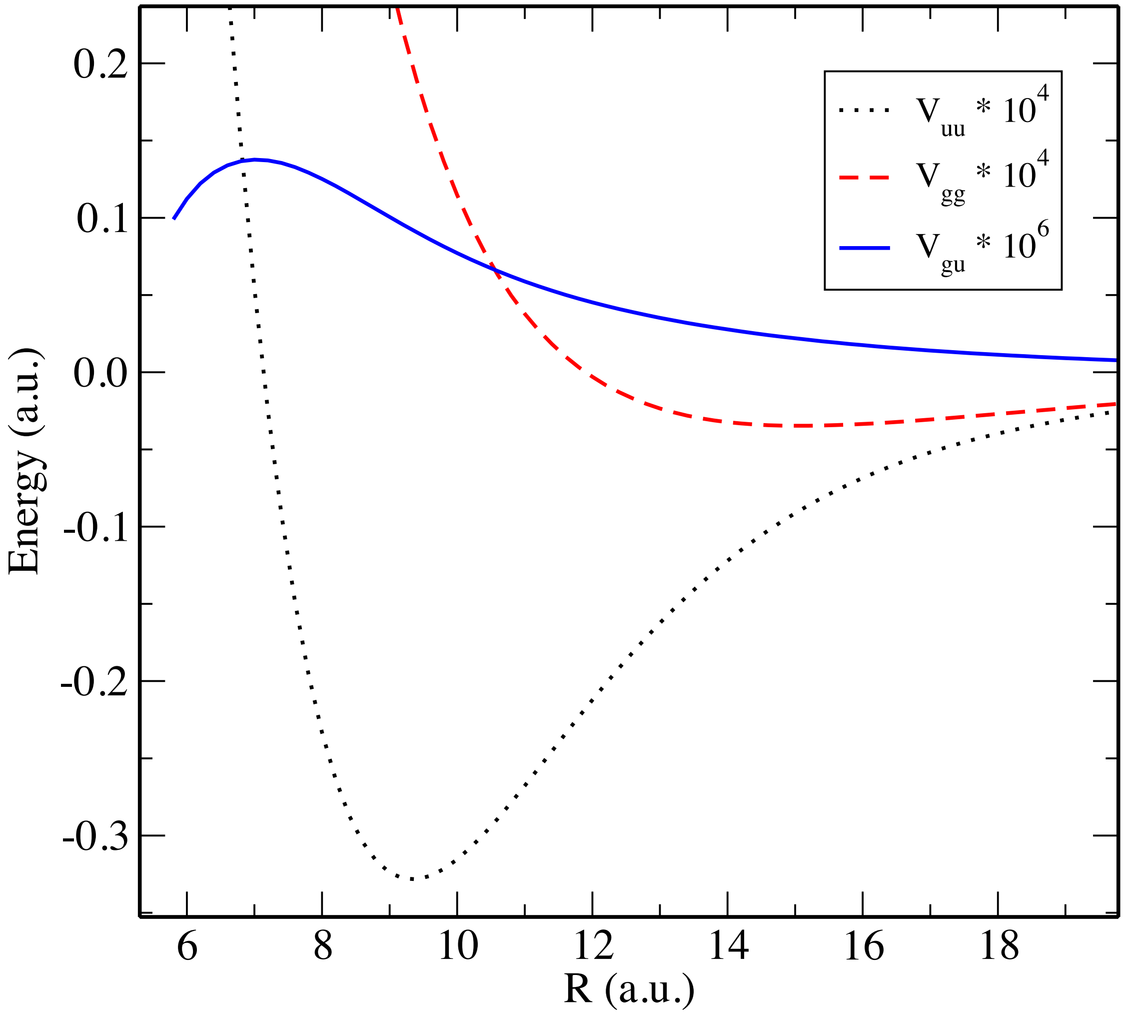

Figure C.2. Calculated $V_{\alpha\beta}$ coupling between the X $^2\Sigma_u^+$ and B $^2\Sigma_g^+$ states in the ^{40}Ca^{43}Ca$^+$ molecular ion. The diagonal couplings (multiplied by 10^4) are shown in black (dotted) and red (dashed) lines, and off-diagonal coupling V_{gu} (multiplied by 10^6) is shown in blue (solid) line.

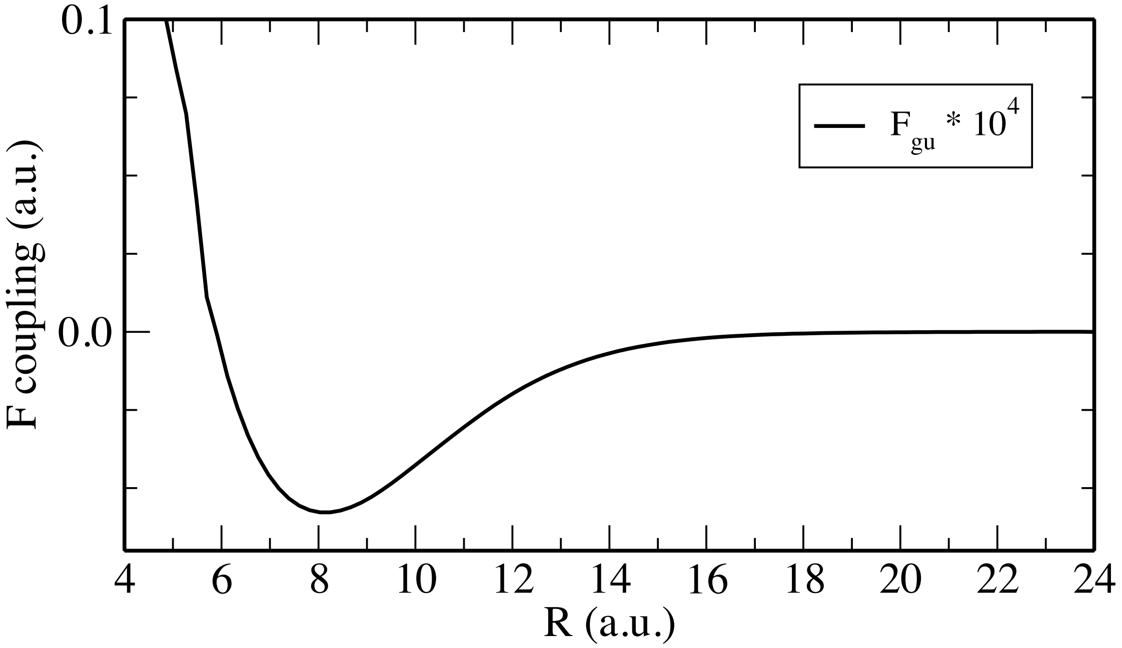

Figure C.3. Calculated first derivative coupling $F_{\alpha\beta}$ (multiplied by 10^4) between the X $^2\Sigma_u^+$ and B $^2\Sigma_g^+$ states in the ^{24}Mg^{25}Mg$^+$ molecular ion.

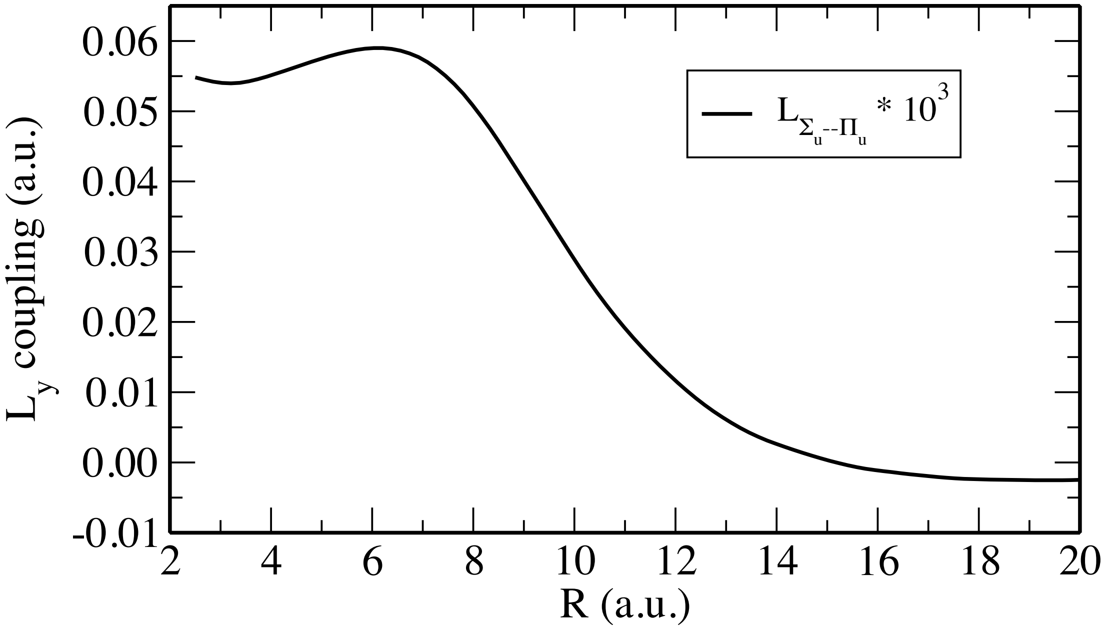

Figure C.4. Calculated L_y coupling (multiplied by 10^3) between the X $^2\Sigma_u^+$ and A $^2\Pi_u$ states in the ^{24}Mg^{25}Mg$^+$ molecular ion.

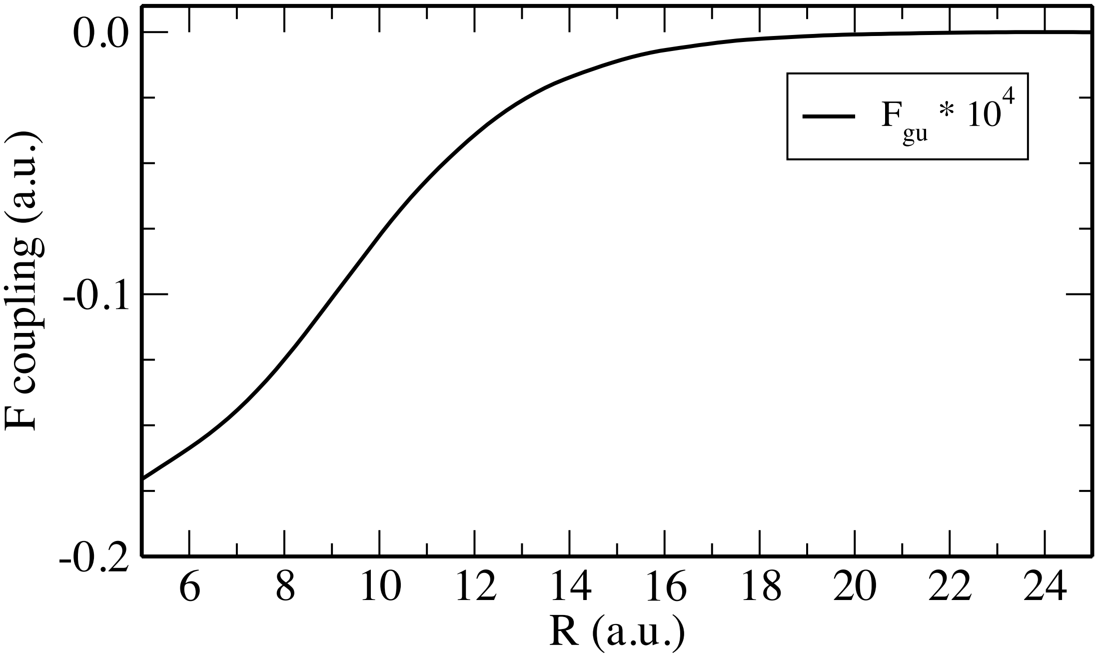

Figure C.5. Calculated first derivative coupling $F_{\alpha\beta}$ (multiplied by 10^4) between the X $^2\Sigma_u^+$ and B $^2\Sigma_g^+$ states in the ^{40}Ca^{43}Ca$^+$ molecular ion.

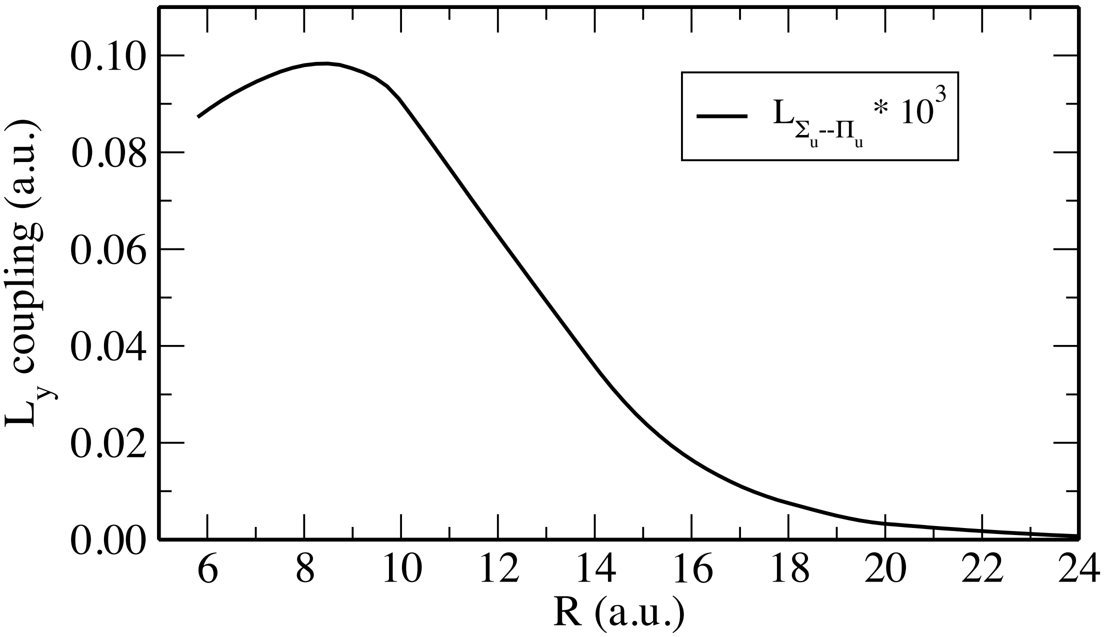

Figure C.6. Calculated L_y coupling (multiplied by 10^3) between the X $^2\Sigma_u^+$ and A $^2\Pi_u$ states in the ^{40}Ca^{43}Ca$^+$ molecular ion.

Appendix D

Hyperfine structure calculation

D.1 Sample *ab initio* input – `GAUSSIAN` and `DALTON` files

As discussed in Chapter 6, there are several coupling coefficients corresponding to the different interaction terms in the hyperfine Hamiltonian. These coefficients are either extracted from experimental measurements or from *ab initio* calculations. All the major coupling constants were obtained from DFT calculations using the `GAUSSIAN` program. The rotational g-factor was obtained from a similar calculation using the `DALTON` program. We list below sample input files for use with `GAUSSIAN` and `DALTON` programs.

```
% Gaussian Code for calculating Hyperfine coupling coefficients
%nproc=4
%mem=2gb
#p b3lyp/gen prop=efg test int=ultrafine output=pickett nmr=spinspin

NaCa+ - Singlet sigma state

 1,1
Na
Ca(Iso=43, Spin=7, QMom=-0.0408, GFac=-1.31727) 1 3.439651

Na     0
S   10   1.00
 379852.2008100            0.20671384468E-04
  56886.0063780            0.16070466617E-03
  12942.7018380            0.84462905848E-03
   3664.3017904            0.35519026029E-02
   1194.7417499            0.12754034468E-01
    430.98192917           0.39895462742E-01
```

```
    167.83169424             0.10720154498
     69.306669040            0.23339516913
     29.951170886            0.36333077287
     13.380791097            0.30544770974
S   3   1.00
    121.74011283             0.36142427284E-01
     37.044143387            0.28820961687
     13.995422624            0.79337384869
S   1   1.00
      5.9827797428           1.0000000
S   1   1.00
      2.4830455118           1.0000000
S   1   1.00
      1.0452506187           1.0000000
S   1   1.00
      0.43875640383          1.0000000
S   1   1.00
      0.65595633185E-01            1.0000000
S   1   1.00
      0.30561925072E-01            1.0000000
S   1   1.00
      0.15509064018E-01            1.0000000
P   8   1.00
    690.77627017             0.37478518415E-03
    163.82806121             0.31775441030E-02
     52.876460769            0.16333581338E-01
     19.812270493            0.59754902585E-01
      8.1320378784           0.15879328812
      3.4969068377           0.29049363260
      1.5117244146           0.36368131139
      0.64479294912          0.28195867334
P   1   1.00
      0.26145823312          1.0000000
P   1   1.00
      0.11704726116          1.0000000
P   1   1.00
      0.40494747666E-01            1.0000000
P   1   1.00
      0.15666707355E-01            1.0000000
D   1   1.00
      5.3000000000           1.0000000
D   1   1.00
      1.5900000000           1.0000000
D   1   1.00
      0.23000000000          1.0000000
D   1   1.00
      0.75700000000E-01            1.0000000
F   1   1.00
      4.2700000000           1.0000000
F   1   1.00
      0.13500000000          1.0000000
****
```

```
Ca     0
S   11   1.00
 2433075.4304000              0.91625196182E-05
  364160.4301500              0.71271617974E-04
   82898.7476370              0.37433706369E-03
   23499.7305400              0.15762862250E-02
    7671.2245985              0.57026102580E-02
    2770.2330687              0.18255738108E-01
    1080.6807550              0.51906421035E-01
     448.04894531             0.12791238579
     194.92007727             0.25586635231
      88.039793338            0.36028678275
      40.645696719            0.26838462020
S   4   1.00
     779.53331918            -0.18403005509E-01
     241.18856300            -0.17649440544
      92.403869324           -0.77662799584
      39.786090342           -1.3352155444
S   1   1.00
      18.195864278            1.0000000
S   1   1.00
       8.3321457067           1.0000000
S   1   1.00
       3.9190196209           1.0000000
S   1   1.00
       1.6667099493           1.0000000
S   1   1.00
       0.80891084908          1.0000000
S   1   1.00
       0.36174199934          1.0000000
S   1   1.00
       0.82379874526E-01            1.0000000
S   1   1.00
       0.47947864375E-01            1.0000000
S   1   1.00
       0.22308112408E-01            1.0000000
P   9   1.00
    4064.2232796              0.19780891021E-03
     962.91550624             0.17307465902E-02
     312.34501046             0.95298721105E-02
     118.76056036             0.38387459783E-01
      49.816153133            0.11679256218
      22.259679401            0.25637225097
      10.286094124            0.37986193747
       4.8606982416           0.30805760637
       2.2525682942           0.85755999942E-01
P   5   1.00
      31.467555443           -0.42441487483E-02
      10.657589056           -0.19579425947E-01
       2.0505555426           0.21237507422
       0.94362089228          0.46277871121
       0.42709067504          0.39177495728
```

```
P    1    1.00
       0.17788187209              1.0000000
P    1    1.00
       0.86000000000E-01                1.0000000
P    1    1.00
       0.41500000000E-01                1.0000000
P    1    1.00
       0.20000000000E-01                1.0000000
D    3    1.00
      16.924012098                0.35543971560E-01
       4.4655403330               0.18133698335
       1.4347576200               0.48002060116
D    1    1.00
       0.46552376784              1.0000000
D    1    1.00
       0.14097711082              1.0000000
D    1    1.00
       0.41467009281E-01                1.0000000
F    1    1.00
       2.6500000000               1.0000000
F    1    1.00
       0.79400000000              1.0000000
F    1    1.00
       0.13000000000              1.0000000
****
```

```
% Sample DALTON input for getting Rotational g-factor
%
% .DAL input
**DALTON INPUT
.RUN WAVE FUNCTION
.PROPERTIES
**WAVE FUNCTIONS
.DFT
 B3LYP
**PROPERTIES
.MAGNET
.QUADRU
.NQCC
.SHIELD
.MOLGFA
.SPIN-SPIN
.SPIN-R
**END OF DALTON INPUT
%
% .MOL input for Na2 molecule
%
BASIS
def2_qzvpp
Na2
B3LYP/def2_qzvpp
    2    0
         11     1
Na   .0000000000            .0000000000            -2.91017
         11     1
Na   .0000000000            .0000000000             2.91017
```

D.2 Hyperfine program sample input/output

D.2.1 Source files

Most of the code development and implementation was done in the Fermi workstation of UConn Physics computer network. An initial version of this code was developed by Phillippe Pellegrini, a former postdoc of the group. This has been modified and redesigned for our specific systems discussed in this thesis. File "hfs.f90" is the main program. It uses the module anglib.f for the calculation of Clebsch-Gordon coefficients. File dwig3j6j9j.f also contains routines used for angular momentum algebra. The program uses the dsyev lapack matrix diagonalization routine. The following simple compilation command (written in makefile) can be used to compile the code,

```
ifort hfs.f90 dwig3j6j9j.f anglib.f
-L/scratch/intel/Compiler/11.0/081/mkl/lib/em64t
-lmkl_lapack -lmkl -lguide -lpthread
```

D.2.2 Input

The standard input file which incorporates all parameters and coupling constants is called “hfs.in”. The following is a sample input file for calculating the hyperfine spectra, of the ^{23}Na^{40}Ca^{+} molecular ion, for the a$^3\Sigma^+$ state in $v = 0$, $N = 0$ level. Note that for ^{40}Ca, the nuclear spin is 0.

```
'23Na40Ca Triplet State'

1.5d0, 0.0d0                                  !i1,i2
2.8514251                                     !Bv, in GHz
-1.8434, 0.0                                  !eQq1,eQq2, in MHz
378.901, -523.27, -272.936, -670.252,
381394600, 503946100                          !c1,c2,c3,c4,c5,c6 in Hz
1.7482403                                     !mu in Debye

2.21752, 0.0, 0.01                            !g1,g2,gr
591.3733d0,1335.627d0                         !sig1,sig2

4.d0                                          !Nmax

0.0d0, 0.0d0, 1d0                             !efmin,efmax,efpas in kV/cm
0d0,100d0,5d0                                 !Bmin,Bmax,Bpas in Gauss
```

The corresponding section in the code which reads the input and brief meaning of the various input parameters is shown below. Detailed discussion of the different terms of the hyperfine Hamiltonian is made in Chapter 6.

```
read(21,*)molec
read(21,*)
read(21,*)i1,i2
read(21,*)Bv
read(21,*)eQq1,eQq2
read(21,*)c1,c2,c3,c4,c5,c6
read(21,*)mu
read(21,*)
read(21,*)g1,g2,gr
read(21,*)sig1,sig2
read(21,*)
read(21,*)Nmax
read(21,*)
read(21,*)efmin,efmax,efpas
read(21,*)Bmin,Bmax,Bpas
```

The various input parameters being,

- 'molec' indicates the molecular system studied.
- i1, i2 are nuclear spins for atom 1 and 2.
- Rotational constant Bv must be in GHz.
- Electric quadrupolar interaction constants eQq1, eQq2 must be in MHz.
- Hyperfine coupling constants (nuclear spin-rotations, scalar spin-spin, tensorial spin-spin, fermi-contact, electronic spin-rotation) c1, c2, c3, c4, c5, c6 must be in Hz.
- Permanent dipole moment 'mu' must be in Debye.
- Rotational coupling constants g1, g2, gr, sig1, sig2 are dimensionless.
- 'Nmax' is the number of rotational levels included in the basis.
- efmin, efmax, efpas are the minimum, maximum, and step values for the static electric field. Must be in kV.cm^{-1}. efmin=efmax for a fixed value.
- Bmin, Bmax, Bpas are the minimum, maximum, and step values for the static magnetic field. Must be in Gauss. Bmin=Bmax for a fixed value.

D.2.3 Output

The total energy eigenvalue of the hyperfine Hamiltonian, as a function of given magnetic field is recorded in the file “fort.34”. The section of the code where this is written is shown below.

```
!eigenenergies in function of the magnetic field


dum=0
do j=dimI+1,3*dimI
dum=dum+v_diag(j)
enddo
dum=dum/(3*dimI)

write(34,'(400(e20.10))')B,((v_diag(j)-dum),j=dimI+1,3*dimI)
```

The Zeeman map of the hyperfine spectra, is simply obtained, by any standard plotting program. I prefer to use `XMGRACE`. The command for plotting the spectra in `XMGRACE` would simply be,

```
xmgrace -free -nxy fort.34 &
```

which would produce the following figure (Fig. D.1),

D.3 Additional curves

We provide here, additional hyperfine spectra of the X $^1\Sigma^+$ state for $N = 1$, for both ^{23}Na^{43}Ca$^+$ and ^{23}Na^{40}Ca$^+$. We also show the hyperfine spectra of the a $^3\Sigma^+$ state for $N = 0$, for ^{23}Na^{43}Ca$^+$.

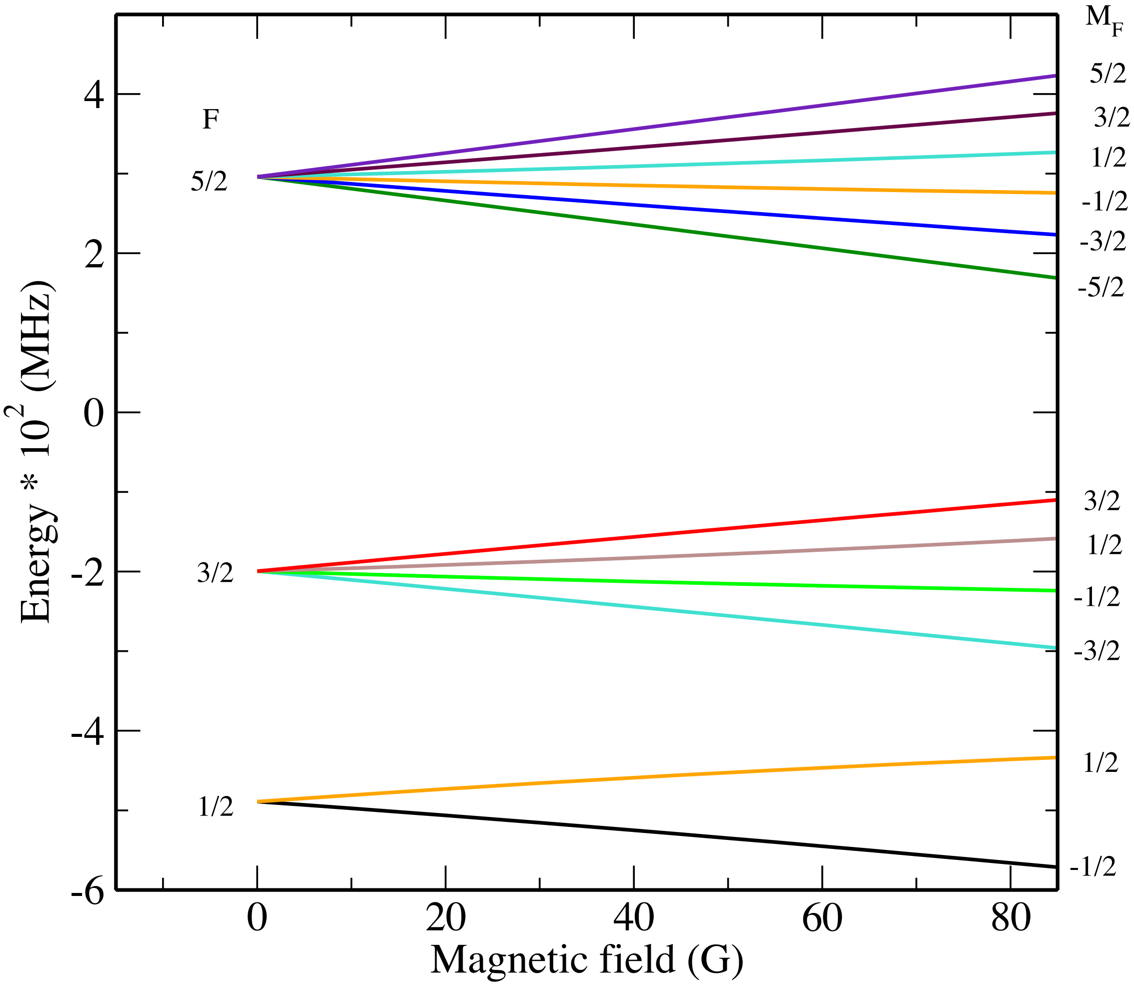

Figure D.1. Hyperfine spectra of ${}^{23}\mathrm{Na}{}^{40}\mathrm{Ca}^{+}$ molecular ion for the $\mathrm{a}^3\Sigma^+$ state in $v = 0$, $N = 0$ level at $r_e = 4.05$ Å.

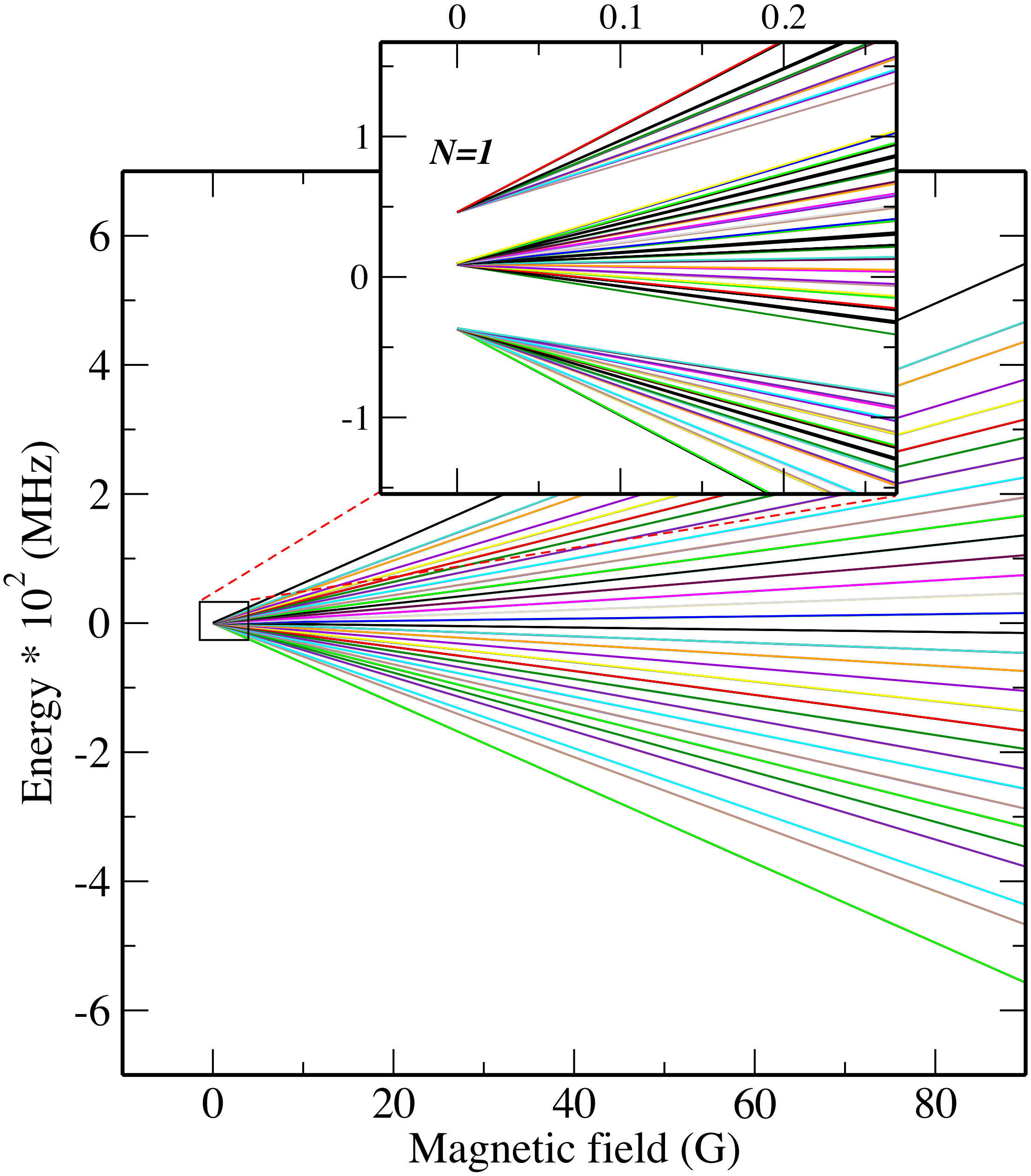

Figure D.2. The figure shows the hyperfine spectrum of ^{23}Na^{43}Ca$^+$ in its ground X $^1\Sigma^+$ state at equilibrium internuclear separation for $N = 1$ at $r_e = 3.43$ Å. The inset scale is in MHz; the zero field splitting is dominated by electric quadrupole interaction. Fig. D.3 (in the following page) shows a magnified view of this inset and the more intricate field splittings.

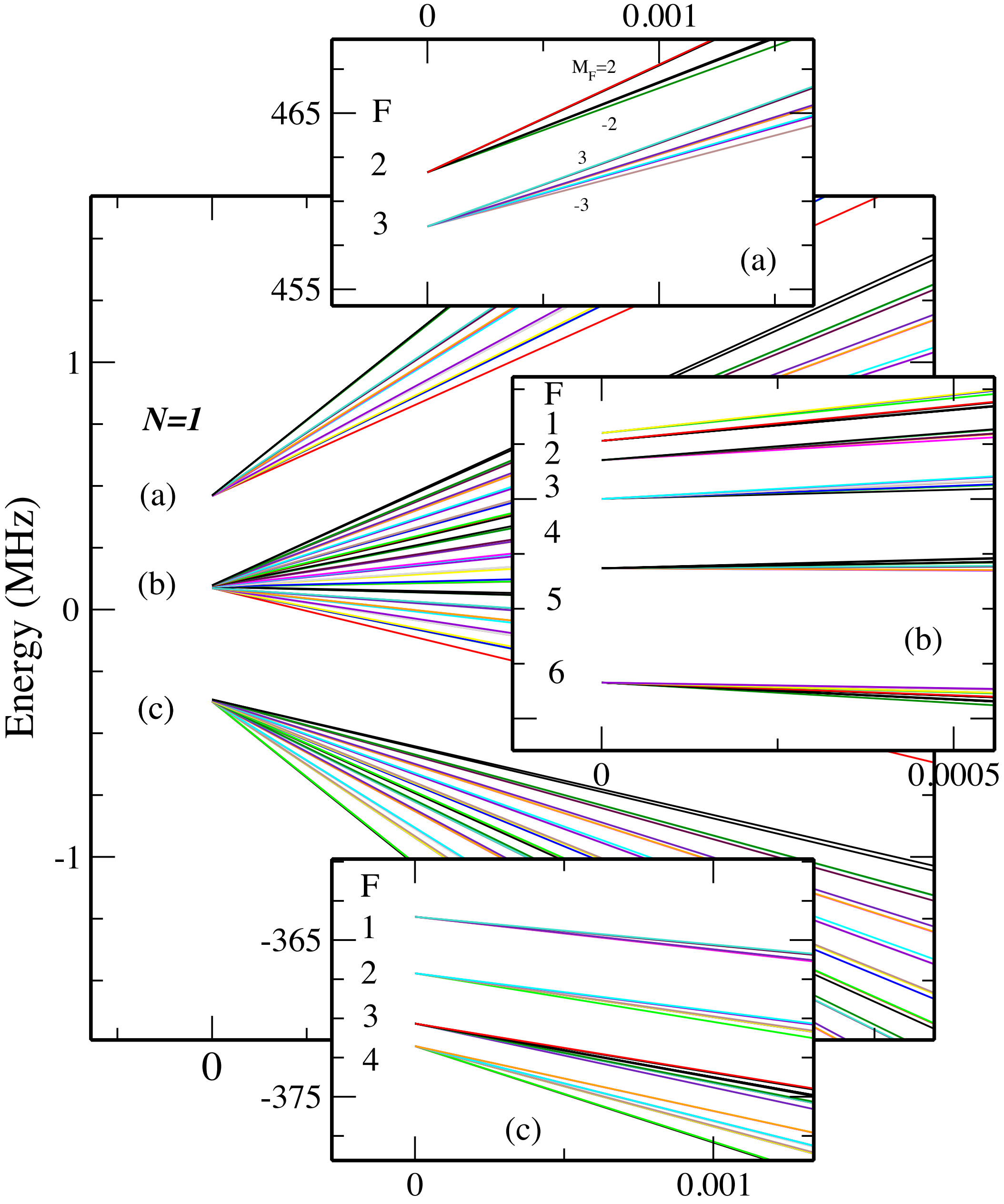

Figure D.3. The figure shows the hyperfine spectrum of ^{23}Na^{43}Ca^{+} in its ground X $^1\Sigma^+$ state at equilibrium internuclear separation for $N = 1$. The three insets show the different hyperfine states arising from the zero-field splittings (a), (b) and (c). Each level with total angular momentum F splits into $(2F + 1)$ levels in the presence of magnetic field, as shown in (a). Similar labeling of M_F values are expected for (b) and (c), but are not shown for simplicity. The energy scale is in kHz.

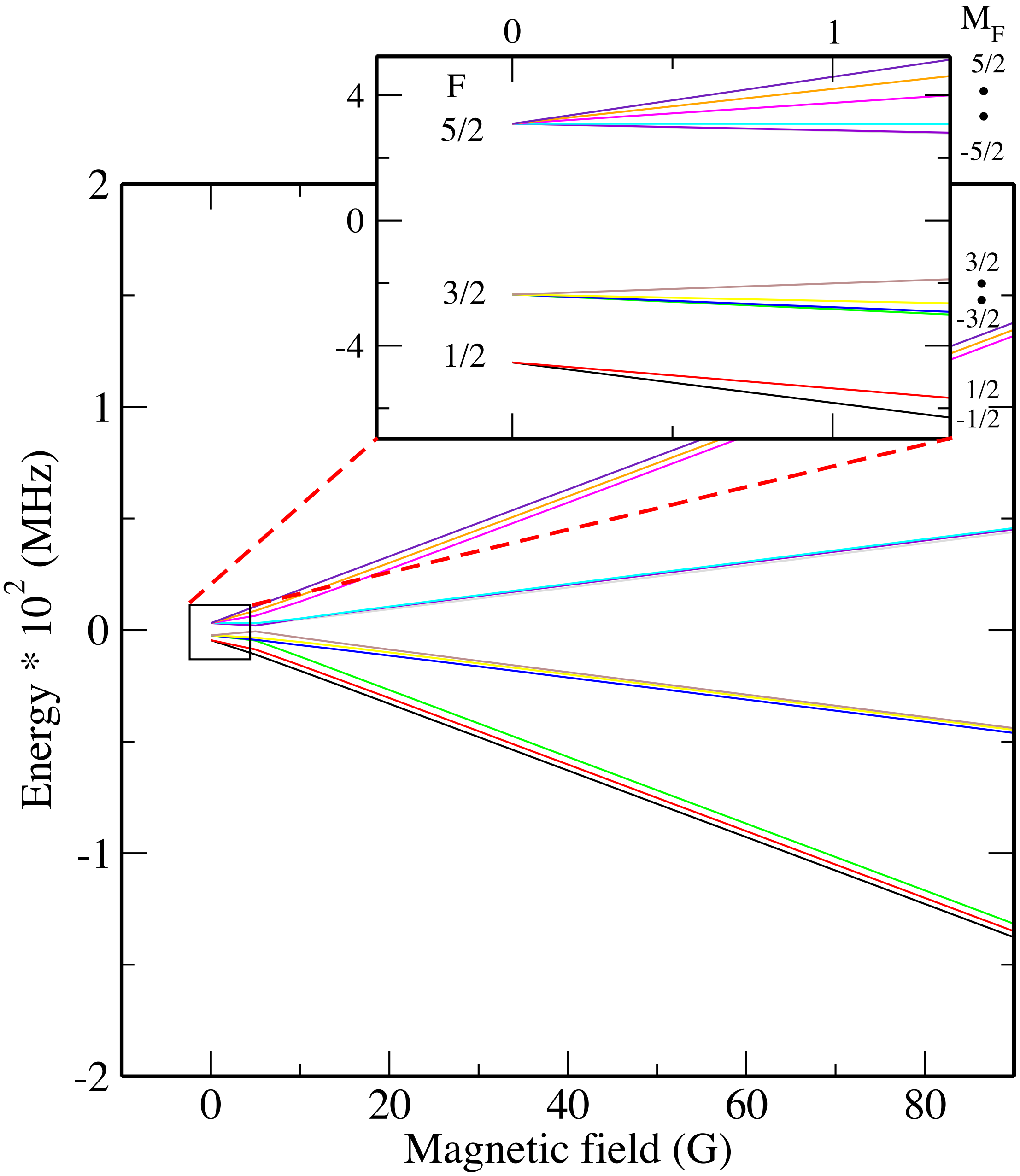

Figure D.4. The figure shows the hyperfine spectrum of ^{23}Na^{40}Ca^{+} in its ground X $^{1}\Sigma^{+}$ state at equilibrium internuclear separation for $N = 1$. The inset scale is in MHz.

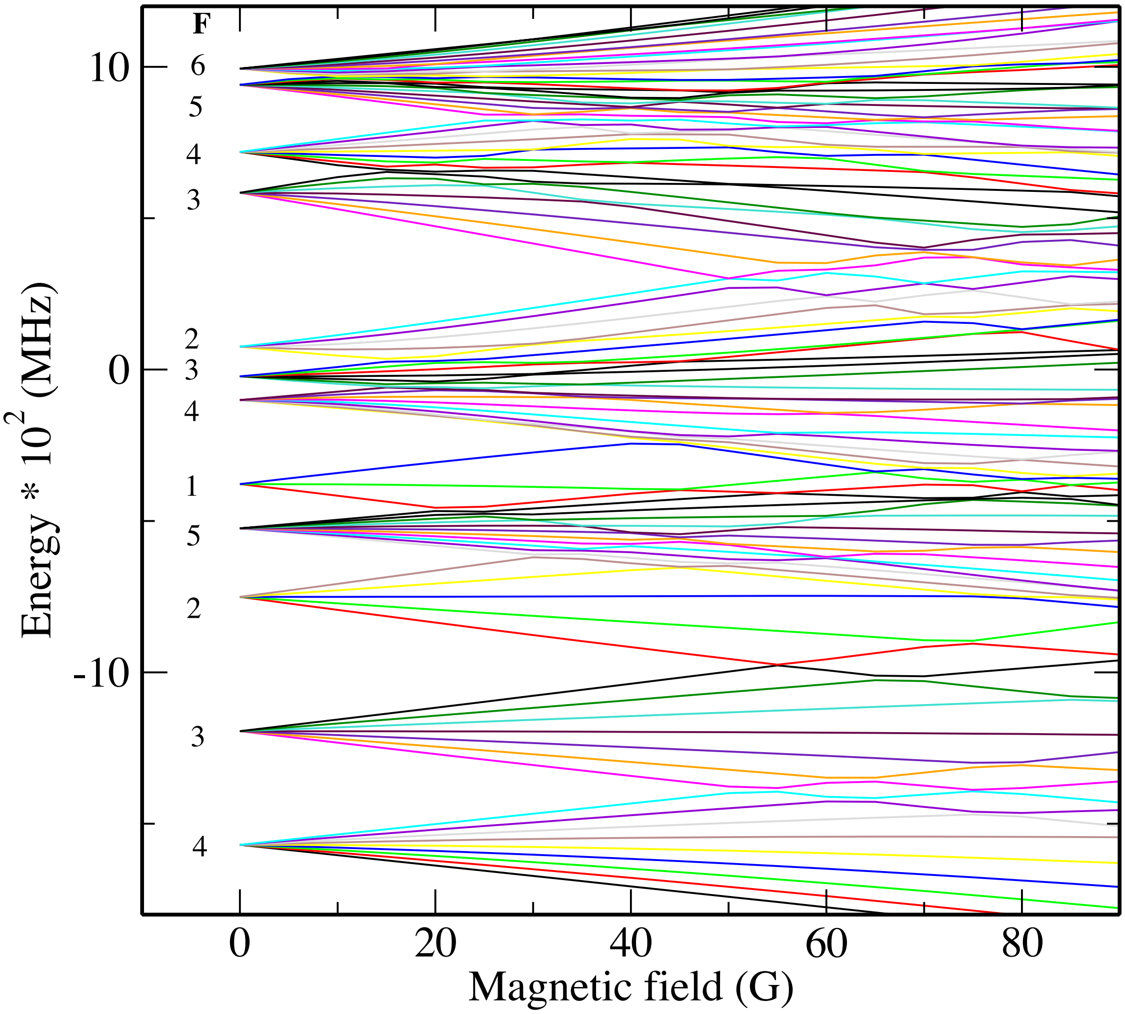

Figure D.5. The figure shows the magnetic hyperfine spectrum of ^{23}Na^{43}Ca$^+$ in the a $^3\Sigma^+$ state at equilibrium internuclear separation for $N = 0$. We see that even for low magnetic field strengths of $\sim$ 60 G, there is mixing between the hyperfine levels which make the spectra more complex.

Bibliography

[1] H. D. L. Lamb *et al.*, Phys. Rev. A **86**, 022716 (2012).

[2] S. T. Sullivan, W. G. Rellergert, S. Kotochigova, and E. R. Hudson, Phys. Rev. Lett. **109**, 223002 (2012).

[3] F. H. J. Hall *et al.*, arXiv **physics.atom-ph**, (2013).

[4] P. Zhang, A. Dalgarno, and R. Côté, Phys. Rev. A **80**, 030703 (2009).

[5] P. Zhang, A. Dalgarno, R. Côté, and E. Bodo, Phys. Chem. Chem. Phys. 1 (2011).

[6] R. Côté and A. Dalgarno, Phys. Rev. A **62**, 012709 (2000).

[7] R. Côté, Phys. Rev. Lett. **85**, 5316 (2000).

[8] S. Porsev, A. Ludlow, M. Boyd, and J. Ye, Phys. Rev. A **78**, 032508 (2008).

[9] D. DeMille, Phys. Rev. Lett. **88**, 067901 (2002).

[10] C. Monroe *et al.*, Phys. Rev. Lett. **75**, 4714 (1995).

[11] M. Brune *et al.*, Phys. Rev. Lett. **77**, 4887 (1996).

[12] A. T. Grier, M. Cetina, F. Oručević, and V. Vuletić, Phys. Rev. Lett. **102**, 223201 (2009).

[13] J. Weiner, V. Bagnato, S. Zilio, and P. Julienne, Rev. Mod. Phys. **71**, 1 (1999).

[14] T. C. Killian *et al.*, Phys. Rev. Lett. **83**, 4776 (1999).

[15] W. R. Anderson, J. R. Veale, and T. F. Gallagher, Phys. Rev. Lett. **80**, 249 (1998).

[16] R. Côté, V. Kharchenko, and M. D. Lukin, Phys. Rev. Lett. **89**, 093001 (2002).

[17] D. Ciampini *et al.*, Phys. Rev. A **66**, 043409 (2002).

[18] C. Cramer, *Essentials of Computational Chemistry: Theories and Models* (Wiley, http://books.google.com/books?id=BKJcbvzl0RsC, 2005).

[19] J. M. L. Martin, Chem. Phys. Lett. **303**, 399 (1999).

[20] I. Fischer, V. E. Bondybey, P. Rosmus, and H. J. Werner, Chem. Phys. **151**, 295 (1991).

[21] T. H. Dunning, J. Chem. Phys. **90**, 1007 (1989).

[22] D. W. Schwenke, J. Chem. Phys. **122**, 014107 (2005).

[23] A. Halkier *et al.*, Chem. Phys. Lett. **286**, 243 (1998).

[24] J. Noga and R. J. Bartlett, J. Chem. Phys. **86**, 7041 (1987).

[25] J. M. L. Martin and G. de Oliveira, J. Chem. Phys. **111**, 1843 (1999).

[26] S. F. Boys and F. Bernardi, Mol. Phys. **19**, 553 (1970).

[27] H.-J. Werner *et al.*, MOLPRO, version 2008.3, a package of ab initio programs, 2008, see http://www.molpro.net.

[28] T. D. Crawford *et al.*, J. Comp. Chem. **28**, 1610 (2007).

[29] M. Kállay and P. R. Surján, J. Chem. Phys. **115**, 2945 (2001).

[30] R. J. Le Roy, Univ. of Waterloo Chem. Phys. Research Report CP-663 (2007) (2007).

[31] J. L. Dunham, Phys. Rev. **41**, 721 (1932).

[32] J. M. Merritt, A. L. Kaledin, V. E. Bondybey, and M. C. Heaven, Phys. Chem. Chem. Phys. **10**, 4006 (2008).

[33] W. J. Stevens, M. Gardner, A. Karo, and P. Julienne, J. Chem. Phys. **67**, 2860 (1977).

[34] H. H. Michels, R. H. Hobbs, and L. A. Wright, J. Chem. Phys. **71**, 5053 (1979).

[35] J. Komasa, Phys. Rev. A **65**, 012506 (2001).

[36] J. Mitroy, private communication (unpublished).

[37] J. Koput and K. A. Peterson, J. Phys. Chem. A **106**, 9595 (2002).

[38] K. Peterson, private communication (unpublished).

[39] B. Meng, P. J. Bruna, and J. S. Wright, Mol. Phys. **79**, 1305 (1993).

[40] P. J. Bruna, B. Q. Meng, and J. S. Wright, J Mol. Spec. **159**, 79 (1993).

[41] J. Doyle, B. Friedrich, R. V. Krems, and F. Masnou-Seeuws, Eur. Phys. J D **31**, 149 (2004), and references therein.

[42] K. M. Jones, E. Tiesinga, P. D. Lett, and P. S. Julienne, Rev. Mod. Phys. **78**, 483 (2006).

[43] J. M. Merritt, V. E. Bondybey, and M. C. Heaven, Science **324**, 1548 (2009).

[44] E. Taylor-Juarros, Formation and analysis of ultracold polar molecules, PhD Thesis, Dept. of Physics, Univ. of Connecticut, 2007.

[45] J. L. Bohn and P. S. Julienne, Phys. Rev. A **54**, R4637 (1996).

[46] E. Juarros, P. Pellegrini, K. Kirby, and R. Côté, Phys. Rev. A **73**, 041403 (2006).

[47] E. Juarros, K. Kirby, and R. Côté, J Phys. B **39**, S965 (2006).

[48] E. Taylor-Juarros, R. Côté, and K. Kirby, Eur. Phys. J D **31**, 213 (2004).

[49] E. P. Wigner, Phys. Rev. **73**, 1002 (1948).

[50] P. Pellegrini and R. Côté, New Journal of Physics **11**, 055047 (2009).

[51] R. Côté, E. Juarros, and K. Kirby, Phys. Rev. A **81**, 060704 (2010).

[52] S. Banerjee *et al.*, Chem. Phys. Lett. **496**, 208 (2010).

[53] M. Marinescu and A. Dalgarno, Phys. Rev. A **52**, 311 (1995).

[54] A. Dalgarno and W. D. Davison, Adv. At. Mol. Phys. **2**, 1 (1966).

[55] A. Dalgarno, Adv. Chem. Phys. **12**, 143 (1967).

[56] J. Y. Zhang and J. Mitroy, Phys. Rev. A **76**, 022705 (2007).

[57] J. Mitroy and J. Y. Zhang, Phys. Rev. A **76**, 062703 (2007).

[58] J. Mitroy and M. W. J. Bromley, Phys. Rev. A **68**, 052714 (2003).

[59] L.-Y. Tang *et al.*, Phys. Rev. A **80**, 042511 (2009).

[60] J. Mitroy, Phys. Rev. A **82**, 052516 (2010).

[61] S. T. Sullivan *et al.*, Phys. Chem. Chem. Phys. **13**, 18859 (2011).

[62] P. Fuentealba, L. von Szentpaly, H. Preuss, and H. Stoll, J Phys. B **18**, 1287 (1985).

[63] E. Czuchaj, M. Krosnicki, and H. Stoll, Theo. Chem. Accts. **110**, 28 (2003).

[64] J. Stanton *et al.*, CFOUR, Coupled-Cluster techniques for Computational Chemistry, 2010, see http://www.cfour.de.

[65] B. Liu and R. E. Olson, Phys. Rev. A **18**, 2498 (1978).

[66] B. Bussery-Honvault and R. Moszynski, Mol. Phys. **104**, 2387 (2006).

[67] K. Patkowski, R. Podeszwa, and K. Szalewicz, J. Phys. Chem. A **111**, 12822 (2007).

[68] S. Porsev and A. Derevianko, JETP **102**, 195 (2006).

[69] J. Mitroy and J.-Y. Zhang, J. Chem. Phys. **128**, 134305 (2008).

[70] J. Mitroy and J. Y. Zhang, Eu. Phys. J. D **46**, 415 (2008).

[71] E. Czuchaj, M. Krośnicki, and H. Stoll, Chem. Phys. Lett. **371**, 401 (2003).

[72] A. Sadlej, M. Urban, and O. Gropen, Phys. Rev. A **44**, 5547 (1991).

[73] J. Mitroy and J. Zhang, Mol. Phys. **108**, 1999 (2010).

[74] A. Lurio and R. Novick, Phys. Scr. **134**, A608 (1964).

[75] L. Ding *et al.*, Phys. Rev. A **48**, 2024 (1993).

[76] E. Bodo, P. Zhang, and A. Dalgarno, New Journal of Physics **10**, 033024 (2008).

[77] P. Zhang, E. Bodo, and A. Dalgarno, The Journal of Physical Chemistry **113**, 15085 (2009).

[78] J. Bardsley, T. Holstein, B. Junker, and S. Sinha, Physical Review A **11**, 1911 (1975).

[79] A. Kaiser, T.-O. Mller, and H. Friedrich, Mol. Phys. 1 (2013).

[80] R. J. Damburg and R. K. Propin, J. Phys. B **1**, 681 (1968).

[81] M. Aymar, R. Guérout, M. Sahlaoui, and O. Dulieu, J. Phys. B. **42**, 154025 (2009).

[82] M. Aymar and O. Dulieu, J. Chem. Phys. **122**, 204302 (2005).

[83] J. Banerjee *et al.*, Phys. Rev. A **86**, 053428 (2012).

[84] K.-K. Ni *et al.*, Science **322**, 231 (2008).

[85] O. P. Makarov, R. Côté, H. Michels, and W. W. Smith, Phys. Rev. A **67**, 042705 (2003).

[86] D. S. Goodman *et al.*, Phys. Rev. A **86**, 033408 (2012).

[87] J. Aldegunde and J. Hutson, Phys. Rev. A **79**, 013401 (2009).

[88] J. Aldegunde, B. Rivington, P. Żuchowski, and J. Hutson, Phys. Rev. A **78**, 033434 (2008).

[89] J. Brown and A. Carrington, *Rotational Spectroscopy of Diatomic Molecules*, *Cambridge Molecular Science* (Cambridge University Press, http://books.google.com/books?id=TU4eA7MoDrQC, 2003).

[90] H. Lefebvre-Brion and R. Field, *The Spectra and Dynamics of Diatomic Molecules* (Elsevier Academic Press, http://books.google.com/books?id=faQ-M34i0ogC, 2004).

[91] M. Haruta, Nature **437**, 1098 (2005).

[92] A. Corma and P. Serna, Science **313**, 332 (2006).

[93] A. S. K. Hashmi and G. J. Hutchings, Angewandte Chemie **118**, 8064 (2006).

[94] A. C. Templeton, M. P. Wuelfing, and R. W. Murray, Accts Chem Res **33**, 27 (2000).

[95] C. J. Zhong and M. M. Maye, Adv Mater **13**, 1507 (2001).

[96] P. D. Jadzinsky *et al.*, Science **318**, 430 (2007).

[97] M. W. Heaven *et al.*, J. Am. Chem. Soc. **130**, 3754 (2008).

[98] H. Qian *et al.*, J Am Chem Soc **132**, 8280 (2010).

[99] N. V. Perera, W. Isley, F. Maran, and J. A. Gascón, J Phys Chem C **114**, 16043 (2010).

[100] A. Venzo *et al.*, Anal Chem **83**, 6355 (2011).

[101] C. M. Aikens, J Phys Chem A **113**, 10811 (2009), pMID: 19746959.

[102] J. F. Parker *et al.*, J Phys Chem C **114**, 8276 (2010).

[103] M. S. Devadas *et al.*, J Phys Chem Lett **2**, 2752 (2011).

[104] D. T. Miles and R. W. Murray, Anal Chem **75**, 1251 (2003).

[105] J. T. v. Wijngaarden *et al.*, J Phys Chem C **114**, 16025 (2010).

[106] I. Garzón *et al.*, Eu J Phys D **9**, 211 (1999).

[107] A. Warshel and M. Levitt, J Mol Bio **103**, 227 (1976).

[108] L. Fabris *et al.*, J Am Chem Soc **128**, 326 (2006).

[109] M. Dasog, W. Hou, and R. W. J. Scott, Chem Comm **47**, 8569 (2011).

[110] M. J. Frisch *et al.*, Gaussian 09 Revision A.1, gaussian Inc. Wallingford CT 2009.

[111] S. Dapprich *et al.*, J Mol Struct **461**, 1 (1999).

[112] T. Vreven *et al.*, J Chem Theo Comp **2**, 815 (2006).

[113] W. D. Cornell *et al.*, J. Am. Chem. Soc. **117**, 5179 (1995).

[114] A. K. Rappé *et al.*, J Am Chem Soc **114**, 10024 (1992).

[115] R. F. W. Bader, *Atoms in Molecules: A Quantum Theory* (Oxford University Press, New York, 1999).

[116] G. Henkelman, A. Arnaldsson, and H. Jansson, Comp Mat Sci **36**, 354 (2006).

[117] M. Z. Zhu, W. T. Eckenhoff, T. Pintauer, and R. C. Jin, J Phys Chem C **112**, 14221 (2008).

[118] J. Akola *et al.*, J. Am. Chem. Soc. **130**, 3756 (2008).

[119] F. Weigend, Phys Chem Chem Phys **8**, 1057 (2006).

[120] H. Qian *et al.*, J Am Chem Soc **132**, 8280 (2010).

[121] O. Lopez-Acevedo *et al.*, J Am Chem Soc **132**, 8210 (2010).

[122] J. R. Cheeseman, G. W. Trucks, T. A. Keith, and M. J. Frisch, J Chem Phys **104**, 5497 (1996).